On the Mechanical Properties and Microstructure of Nitinol for Biomedical Stent Applications

by

Scott Wade Robertson

B.S. (University of Texas, Austin) 1998
M.S. (University of California, Berkeley) 2004

A dissertation submitted in partial satisfaction of the

requirements for the degree of

Doctor of Philosophy
in

Engineering-Materials Science and Engineering

in the

GRADUATE DIVISION

of the

UNIVERSITY OF CALIFORNIA, BERKELEY

Committee in charge:

Professor Robert O. Ritchie, Chair
Professor Kevin E. Healy
Professor Lisa A. Pruitt

Fall 2006

The dissertation of Scott Wade Robertson is approved:

Chair (Date)

(Date)

(Date)

University of California, Berkeley

Fall 2006

Abstract

On the Mechanical Properties and Microstructure
of Nitinol for Biomedical Stent Applications

by

Scott Wade Robertson

Doctor of Philosophy in Engineering-Materials Science and Engineering

University of California, Berkeley

Professor Robert O. Ritchie, Chair

This dissertation was motivated by the alarming number of biomedical device failures reported in the literature, coupled with the growing trend towards the use of Nitinol for endovascular stents. The research is aimed at addressing two of the primary failure modes in Nitinol endovascular stents: fatigue-crack growth and overload fracture. The small dimensions of stents, coupled with their complex geometries and variability among manufacturers, make it virtually impossible to determine generic material constants associated with specific devices. Instead, the research utilizes a hybrid of standard test techniques (fracture mechanics and x-ray micro-diffraction) and custom-designed testing apparatus for the determination of the fracture properties of specimens that are suitable representations of self-expanding Nitinol stents. Specifically, the role of texture (crystallographic alignment of atoms) and the austenite-to-martensite phase transformation on the propagation of cracks in Nitinol was evaluated under simulated

body conditions and over a multitude of stresses and strains. The results determined through this research were then used to create conservative safe operating and inspection criteria to be used by the biomedical community for the determination of specific device vulnerability to failure by fracture and/or fatigue.

Professor Robert O. Ritchie
Dissertation Committee Chair

TABLE OF CONTENTS

LIST OF FIGURES

ultimately can lead to arrest of the crack, e.g., at the fatigue threshold. Crack propagation is from left to right, at ΔK = 1.25 MPa$\sqrt{m}$ (R = 0.7).

Figure 5.6: Scanning electron micrographs of fatigue striations in the mid-range of growth rates (Paris) regime (R = 0.1, ΔK = 8-9 MPa$\sqrt{m}$, da/dN = 1-2 x 10^{-7} m/cycle). The fatigue striation spacing was ~2-4 x 10^{-7} m/striation, which corresponds well with the measured global crack-growth rates. Macroscopic fatigue crack propagation is left to right in these photo-micrographs; however the striations in this analyzed region (near the C(T) specimen surface) are oriented top to bottom due to the curvature of the crack front near the sample edges.

Figure 5.7: Fatigue-crack growth behavior in Nitinol tube (45° orientation) at R = 0.5 comparing tests conducted in air at 50 Hz [117], with corresponding results in simulated body fluid (HBSS) at 50 and 1 Hz; n = 4 per condition (except at 1 Hz where n=1). It is apparent that there is no significant difference in fatigue-crack growth data collected in air or in HBSS. Moreover, lower frequencies, which more accurately represent *in vivo* conditions, produce marginally slower growth rates than at higher frequencies, indicating that the higher frequency tests that are invariably utilized may in this case provide slightly more conservative lifetime predictions for Nitinol biomedical devices.

Figure 5.8. Fatigue data from thin-walled superelastic Nitinol tube tested in 37°C air [117] and Hanks' Balanced Saline Solution (HBSS) in the current work showing (a) fatigue-crack growth rates as a function of stress-intensity range ΔK, and (b) the variation in fatigue threshold values with the load ratio (K_{min}/K_{max}), which are virtually identical.

Figure 5.9: Comparison of the current fatigue crack-growth behavior of Nitinol tube tested in HBSS (black circles) at R=0.1 with the same material tested in air (red circles) [117], and all other previously reports of superelastic material: Melton & Mercier [31], Dauskardt *et al*. [20], McKelvey & Ritche [56], and Filip *et al*. [58]. Visually, it is clear that Nitinol tube crack-growth curves are steeper than any previous study in bar, plate and strip. Statistical analysis confirms that visual observation: P-values for the hypothesis that the curves from the present work and [117] are collinear with any of the other data are <0.1%.

Figure 6.1: Schematic illustration of the compact-tension specimen and region of imaging. The blue box represents the approximate area surrounding the crack tip that was scanned by x-ray micro-diffraction; this region ranged in size from 0.1 x 0.1 to 1 x 1 mm^2, with many thousands of Laue diffraction patterns collected within that box. Specimen dimensions were crack size a ~ 5.4 mm, thickness B ~ 0.4 mm, and width W~10.8 mm. Green arrows denote the direction and location of applied load, which ranged from 0 to 62 N, corresponding to stress-intensity values up to 15 MPa$\sqrt{m}$.

Figure 6.2: Coarse scale (~1 mm^2; 16 x 16 μm step size) elastic strain and resulting phase maps. The top row shows the resultant strains (ε_{yy}, ε_{xx}, ε_{xy}) and regions of transformed martensite surrounding a crack loaded from 0 to 7.5 MPa√m, with the gray regions representing the crack and the phase-transformed material as determined by an absence of Laue diffraction spots. The second row of contour maps shows a dramatic increase in strains and volume fraction of martensite after the crack was further loaded to a stress intensity of 15 MPa√m. Finally, the sample was unloaded to back to 7.5 MPa√m where it is apparent that both the residual tensile strains parallel to the crack face (ε_{yy}) and the martensite volume fraction are much larger than during the first cycle of loading.

Figure 6.3: Evolution of the transformation zone in response to a single loading and unloading cycle. These fine step-size diffraction maps (3 x 3 μm grid) show the change in size and shape of the transformation zone in response to a loading cycle from 10 to 15 to 10 MPa√m. The black, peanut-shaped boundary in column 3 shows the transformation zone predicted by the combination of simple fracture mechanics solutions [114] with the anisotropic Nitinol yield criterion of Lexcellent and Blanc [132]. The partially transformed material, which comprises a mixture of the austenite and martensite phases, was experimentally-determined using three different criteria: a) *Criterion 1* based upon peak broadening, revealed a much smaller transformed region than was predicted by fracture mechanics; b) *Criterion 2* based on equivalent stresses > tensile transformational stresses, resulted in a zone size and shape in excellent accord with fracture-mechanics predictions; and c) *Criterion 3* based upon directionality-dependent stresses > tensile transformational stresses, again resulting in good correlation to the anisotropic predictions from fracture mechanics-based solutions but slightly larger than from Criterion 2 because of the inclusion of the dilational strains in this criterion. Note that the scale bar applies to all plots, except the zoomed-out views (column 3) which have a 100 μm scale bar inset.

Figure 6.4: Grain-by-grain evolution of the austenite-to-martensite transformation ahead of a crack tip in response to fatigue loading (7.5 to 15 MPa√m) through 100 cycles. The color maps represent Miller index planes or directions of individual austenite grains as indicated above each column, and the black regions are fully transformed martensite. During the first loading cycle to 7.5 MPa√m, the fully transformed zone is <50 μm wide. Subsequent loading to 15 MPa√m and unloading to 7.5 MPa√m results in a growing fully transformed zone size at the 7.5 MPa√m, which stabilizes at ~120 μm between cycle 2 and 10. Conversely, the transformation zone size at the upper stress-intensity level remains constant (~ 200 μm) throughout the fatigue loading cycles. Interestingly, instead of retaining the classic peanut-shaped zone that was seen in earlier experiments, instead several grains have apparently suppressed the phase transformation. These grains are further investigated in Fig. 6.5.

Figure 6.5: Atomistic loading diagram of preferentially untransformed grains shown in Fig. 6.4. The red planes are parallel to the C(T) surface, yellow planes are parallel to the fracture surface, red arrows show the direction of crack growth, and green arrows show the applied loading direction. Note that only the titanium atoms are shown in the diagram for clarity; nickel atoms reside at the [½,½,½] positions. Schematic diagrams of the crystallographic orientations of each grain are given as, a) Grain *A* is oriented with (110) planes parallel to both the C(T) surface (red) and the crack plane (yellow) with growth in the [100] direction; b) Grain *B* shows the lower-most untransformed grain from Fig. 4, with (120) planes parallel to the C(T) surface (red), (100) parallel to the crack plane, and growth in the [120] direction; and c) Grain *C* is immediately ahead of the crack tip, with its (110) plane parallel to the specimen surface, (100) parallel to the crack plane, and [110] in the direction of crack growth.

Figure 7.1. A typical fatigue-crack growth-rate curve plotted in log-log scale with critical locations marked. Threshold values, ΔK_{th}, for large cracks are determined from experimental data collected using standard fracture-mechanics specimens and typically represent the asymptotic stress-intensity range for crack growth. This asymptote of the data in Nitinol tube is invariably due to crack closure effects from interference or wedging of oxidation debris or fracture surface asperities inside the crack flanks. Physically small cracks, however, are more relevant to commercial biomedical devices, and are not subjected to the same closure effects as laboratory-grown large cracks; consequently, they may propagate at stress intensities lower than predicted by large-crack data. Estimates of the threshold stress-intensity range for small cracks can be made by extrapolation of the linear Paris growth-rate curve down to 10^{-10} m/cycle. For small-scale biomedical devices such as endovascular stents that are only a few hundred micrometers thick in specific regions, any stress-intensity ranges above the ΔK_{th} value, *i.e.*, in the Paris or unstable growth regime, can result in rapid through-thickness fracture. Accordingly, the threshold ΔK_{th} value can be considered as the critical limiting variable.

Figure 7.2. A safe-operating device design diagram is shown for devices manufactured from thin-walled superelastic Nitinol tube. Stress intensities attributed to single events, *e.g.*, crimping and deployment stresses in a stent, are represented on the horizontal axis and vary by the angle that the crack is propagating with respect to the tube-drawing direction. Stress-intensity ranges attributed to cyclic events, *e.g.*, contraction and dilation of a stent in response to the heartbeat, are represented on the vertical axis and vary with load ratio, *R*, and whether the experimental large-crack fatigue data or the more conservative small-crack estimates are used. Any combination of defect sizes and single-event stresses and/or cyclic stresses falling into Region 1 pose no threat of fracture or crack propagation under the evaluated conditions. Devices whose stress intensities fall in Regions 2 and 3 are mildly susceptible (depending on exact *R*-ratio and crack-growth directions) to fatigue-crack growth and fracture, respectively; in region 4, the device is susceptible to fracture by either mechanism. Parts that are subjected to any portion of Region 5 are

in great risk of fracture either by fatigue or overload, regardless of the crack angle and *R*-ratio.

Figure 7.3. Kitagawa-Takahashi diagram [137] for thin-walled superelastic Nitinol tubing showing regions of safe operation (green), risk of failure by fatigue but not overload fracture (yellow), and eminent risk of failure by either fatigue or overload fracture. The transition crack-size between small-crack behavior, governed by the S/N endurance strength (100 – 200 MPa [52, 71]), and large-crack fracture mechanics data, is ~15-50 μm. Above that flaw size, fatigue fracture is best defined by the fracture mechanics-based threshold criterion ΔK_{th}, which is a function of the positive load-ratio, *R*. Failure by overload is bounded by the martensitic yield stress for Nitinol tube (1000 – 1200 MPa [138, 139]) up to a flaw size of ~25 μm, at which point the crack-initiation fracture toughness of the material dominates failure. For crack sizes exceeding ~400 μm, the steady-state fracture toughness value (~34 MPavm) governs the point of fracture, hence the jump from the longitudinal, circumferential and 45° safe operating curves. It should be noted that for the purposes of determining this particular diagram, the geometry factor *Y* was taken as unity and general yield stress defined in uniaxial tension. For an actual device, these would have to be calculated for the specific loading, crack and device geometry.

LIST OF TABLES

ACKNOWLEDGEMENTS

This dissertation would not have been possible without the tremendous support and encouragement from family and friends, especially my parents who have always encouraged me to follow my dreams and happiness. I owe immense thanks to Professor Robert Ritchie. Rob's excellent guidance, advice, mentoring, and most importantly friendship was instrumental in my development as a graduate student. He continually put the needs of myself, and his other graduate students, at the top of his list of priorities.

I would also like to acknowledge the support of my office mates, Jay Foulk and Jessica Stankiewicz, and other members of the Ritchie Group for helpful discussions which contributed to the success of my work. Without the friendship of Valentina Imbeni, who sacrificed her own funding to support my first year at UC-Berkeley, I may never have had the opportunity to study at this great university. Beamline physicists, Drs. Apurva Mehta and Nobumichi Tamura, provided so much guidance and imparted me with so much knowledge on those countless sleepless nights at the beamline.

Lastly, I must thank Nitinol Devices and Components, Inc. which funded this research and provided material. More importantly, however, were the great friendships that I developed with the people at NDC, namely Drs. Tom Duerig, Alan Pelton and Xiao-Yan Gong. In particular, I owe a huge debt of gratitude to Alan who was always there with advice or knowledge when I needed it and patiently answered all my questions regarding Nitinol.

CHAPTER 1: INTRODUCTION

1.1 What is Nitinol?

Nitinol is an alloy of roughly 50% Nickel and 50% Titanium. Discovered only recently (1960s) as part of a Naval research project [1], Nitinol derives its name from its chemical components and its founders: Ni (Nickel) + Ti (Titanium) + NOL (Naval Ordinance Lab). It has good biocompatibility (response is similar to stainless steel) [2-5] and good magnetic resonance imaging opacity (i.e. can readily be seen by X-ray or MRI) [6, 7], making it ideally suited for design of biomedical implantable devices. More importantly are two characteristics that make Nitinol extraordinarily unique from other bioengineering metallic alloys, namely its superelasticity and shape-memory, which are described in Section 1.3. These two unique properties are attributed to a first-order phase transformation from the parent austenite phase to the daughter martensite phase (see Section 1.2) which can occur via the addition of an energy source either in the form of heat or stress [8].

Since its commercial introduction in the 1970s, Nitinol has been used for a variety of applications: pipe couplings, bra underwires, earthquake dampeners, eyeglass frames, orthodontic wires, mobile phone antennas, micro-actuators, and a variety of biomedical devices [6, 9-11]. Recently, however, the Nitinol community's trend has been to turn its efforts to the biomedical device field [6, 10, 12].

1.2 Microstructural Phases in Nitinol

Nitinol's first-order phase transformation progresses from the parent austenite, a simple cubic B2 (i.e. CsCl) structure, to the daughter martensite, monoclinic B19', phase via an athermal transformation [8, 13]. This transformation is instantaneous once enough

energy, in the form of temperature flux or stress, has been introduced to the system. Specifically the martensite forms upon cooling below the martensite-start temperature, M_s, or via the application of stresses which form so-called stress induced martensite (SIM) [8]. This phase change occurs by simple displacement of atoms (via Bain strain and lattice invariant shear) without diffusion of atoms or the breaking of bonds [8].

At temperatures below the martensite finish temperature, M_f, the martensite is stable and a transformation cannot occur by the addition of stress. Additionally, if temperatures exceed the so-called martensite deformation temperature, M_d, the energy (in the form of applied stress) required to form SIM exceeds the energy to plastically deform the austenite (via dislocation mobility), thereby making the structure a stable, non-transforming austenite phase. Only within temperatures between the austenite finish, A_f, and the M_d can a stress-induced phase transformation occur. In the present study, all mechanical tests were performed at ~7°C above the A_f such that the superelastic SIM response could occur.

Sometimes, due to annealing, chemical alloying elements, or microstructural defects in the material, the direct austenite-to-martensite transformation is interrupted by an intermediate rhombohedral phase (R-phase) [14-16]. This intermediate phase transformation, resulting in relatively small recoverable strains (~0.5%) [16], is undesirable, yet often unavoidable, for many Nitinol applications (including endovascular stents) where a perfectly linear-elastic austenite loading/unloading regime is preferred [17]. However, precise manufacturing procedures perfected over many decades of research has minimized the contributions of this phase [18]. For the Nitinol tube studied in this text, it is recognized that the R-phase does occur, however the contribution of

strain is <0.2% and irrelevant since fatigue and fracture necessarily occur in the martensite phase at strains/stresses well in excess (2-6 times) of those required for R-phase formation [19].

During the austenite-to-martensite phase transformation, there is a small volume contraction, termed "negative dilation" by the authors in ref. [20]. The exact value of this contraction is debated in the literature - Holtz *et al.* [21] report -0.39% and Dauskardt *et al.* [20] report -0.54%. Using the synchrotron diffraction data presented in ref. [22], which tested the exact material that is utilized throughout this text, one can calculate that, at body temperature 37°C, this volume change is –0.33%, and increases with increasing temperature above the A_f. Unlike other transforming materials that have a positive volumetric change which serve to toughen the material [23-25], it has been proposed that this negative dilation in Nitinol has a deleterious effect on the fracture- and fatigue-resistance by locally raising the stress intensity ~13% [20, 21].

1.3 Unique Mechanics: Shape-Memory and Superelasticity

Shape-memory is the ability of Nitinol to "remember" its shape following a deformation, and is graphically depicted in Fig. 1.1. This phenomenon utilizes the temperature effects on the phase transformation. From the austenite phase, Nitinol is cooled below its M_f temperature such that the stable phase is (twinned) martensite. While in this phase, the twinned martensite is deformed which causes non-plastic detwinning, all while still maintaining a martensite crystal structure [8]. Upon removal of the load, the martensite elastically recovers, but retains some permanent deformation (strain). Finally, the addition of heat to above the A_f temperature returns the material to its original shape and austenite phase [8]. An example of the application of this unique mechanical

property is the Simon vena cava filter which is cooled to below M_f, collapsed into a chilled saline catheter, tortuously inserted into the heart at which point the human body temperature is sufficiently above the A_f to cause expansion of the filter into its preprogrammed shape [26].

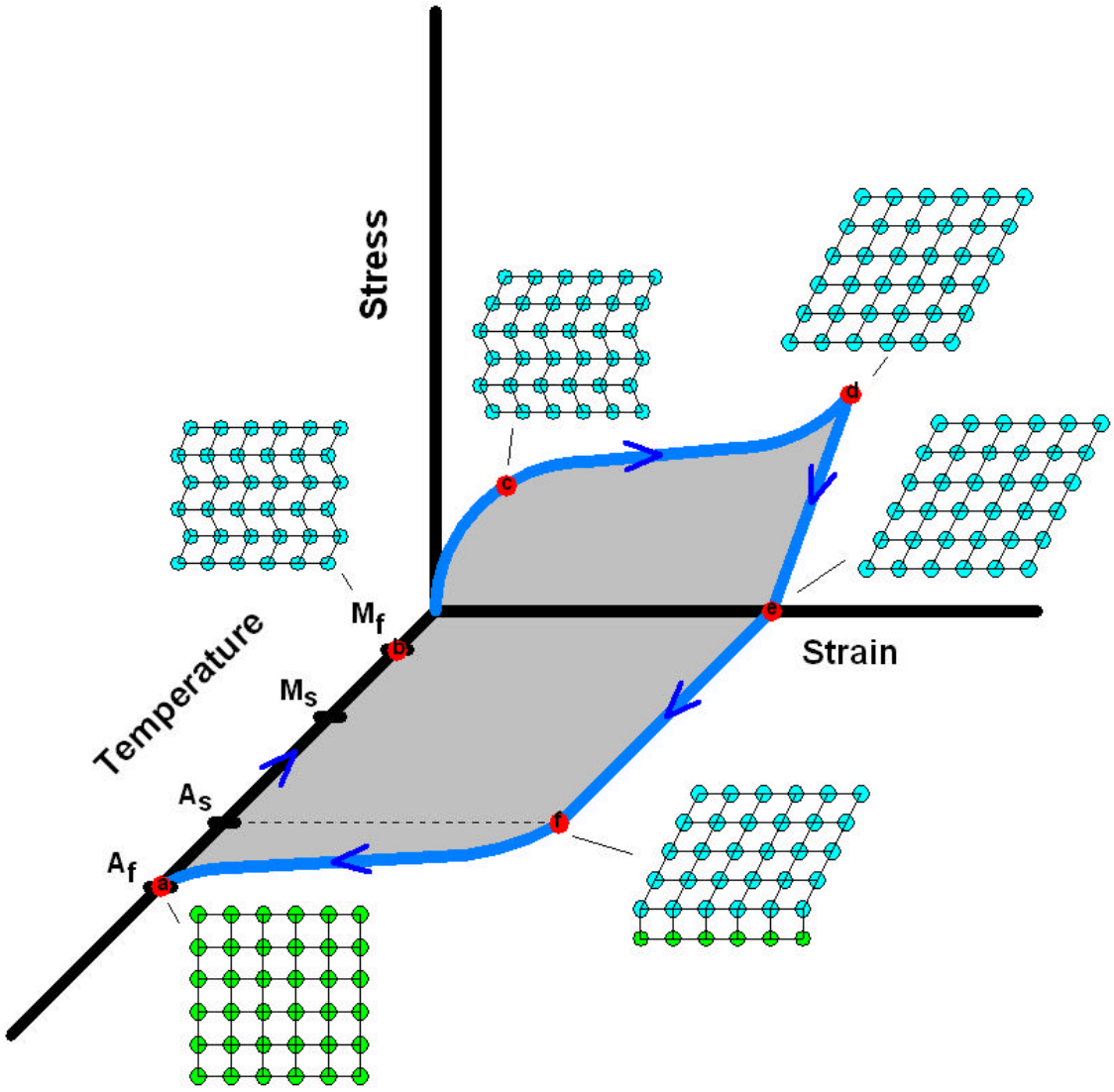

Figure 1.1: Schematic diagram of the shape memory effect (after [8]). At high temperature (a), the material is fully austenite. Lowering the temperature below the M_f (b) without the addition of stress causes a phase transformation to twinned martensite. As the martensite is loaded, it begins to detwin (c), until full detwinning has occurred (d). Upon unloading to (e), the martensite elastically recovers, but does not return to a twinned state. Raising the temperature to the austenite start temperature, A_s (f), begins the reverse transformation from martensite to austenite, which is complete at A_f (a).

Superelasticity, see Fig 1.2, is the ability to elastically deform to higher than normal levels when mechanically deformed between the A_f and M_d temperatures [8]. Specifically Nitinol can elastically deform to nearly 11% strain [6, 7], whereas most metals only have the ability to elastically deform to less than 1% strain. While in this temperature range, Nitinol deformation above ~1% results in a phase transformation from austenite to detwinned martensite. An additional forward strain is required, typically at a relatively constant stress "plateau", to fully transform all of the austenite phase to martensite. Upon unloading, the martensite phase becomes unstable and transforms back to its original austenite phase, resulting in full strain-recovery upon the removal of load.

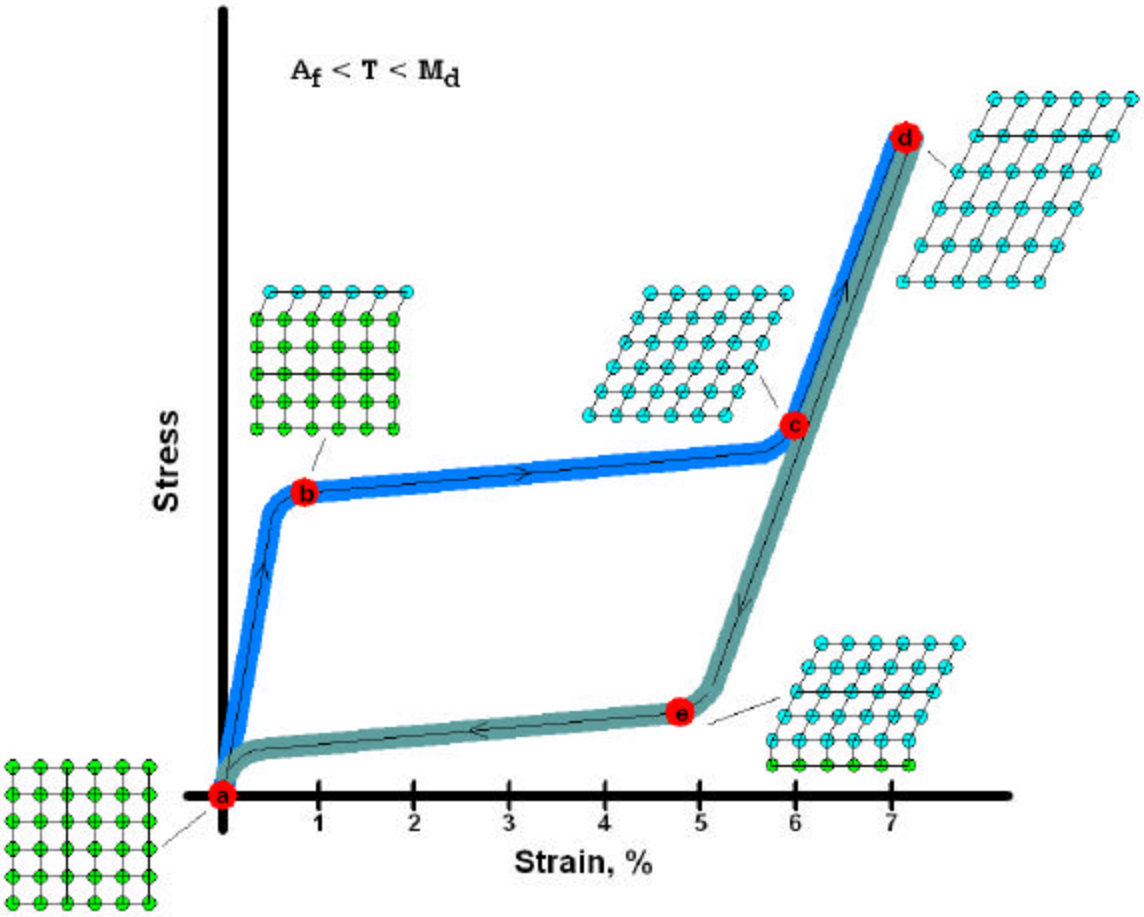

Figure 1.2: At temperatures above the austenite finish temperature, A_f, but below the martensite deformation temperature, M_d, the superelastic effect occurs in Nitinol as shown (after [8]). Starting at (a) the material is fully austenite. The austenite is

elastically loaded to point (b) at which time transformation to martensite occurs (the martensite forms in twins, and instantaneously detwins due to the high applied stresses). Further loading along a stress "plateau" to point (c) fully transforms the material to martensite. Continued loading to (d) requires increased stress and elastically deforms the martensite (note that the SIM elastic modulus is lower than the austenite modulus of elasticity). Unloading back through point (c) recovers the elastic strains in the martensite, and continued unloading to (e) forces the onset of the reverse transformation to austenite, with full reverse transformation upon complete unloading to (a).

1.4 Biomedical Application of Nitinol: Endovascular Stents

Named after the dentist Dr. Charles Stent (1845 – 1901), today the term stenting refers to the practice of bracing or scaffolding traumatized or diseased tubular vessel walls in the human body to: a) increase the diameter and thereby the flow through the tube, and/or b) so that the vessels do not collapse due to their own inherent weakness [27]. Although most Nitinol stents are particular focused on scaffolding of blood vessels, it should be noted that many other parts of the human anatomy are stented as well, e.g. tracheal stenting following trauma from a seat belt during a car crash or esophageal stenting following tissue damage from chronic gastric reflux [28].

Nitinol self-expanding stents utilize the superelastic effect both for deployment and *in vivo* operation [29], see Fig. 1.3 for a representation of stresses witnessed by a stent during its deployment and service. During manufacturing, a stent in the austenite phase ($A_f < T < M_d$) with an originally large diameter (e.g. 8 mm) is collapsed (e.g. 1.5 mm diameter) whereby it transforms to martensite, and inserted into a catheter for implantation in the body. When deployed from the catheter *in vivo*, the stent expands (creating a reverse martensite-to-austenite transformation), but is constrained by the arterial walls (e.g. 6.5 mm diameter) such that complete strain recovery cannot occur. This incomplete phase recovery is not by accident. Indeed, an incompletely reverse-transformed Nitinol stent imparts very beneficial mechanics to the device, termed

"biased-stiffness" [7, 30], which is explained as follows. In order to collapse the stent, forward transformation (austenite-to-martensite) must occur which requires loading along the elastic curve of austenite (high stiffness), thereby making collapse of the artery very difficult (i.e. requiring significant applied stress). Conversely, further expansion of the artery requires continued reverse (martensite-to-austenite) transformation which is primarily a strain-based transformation requiring very little stress; therefore the stent preferentially continues to expand through the luminal wall until reaching a stress equilibrium with the surrounding tissue.

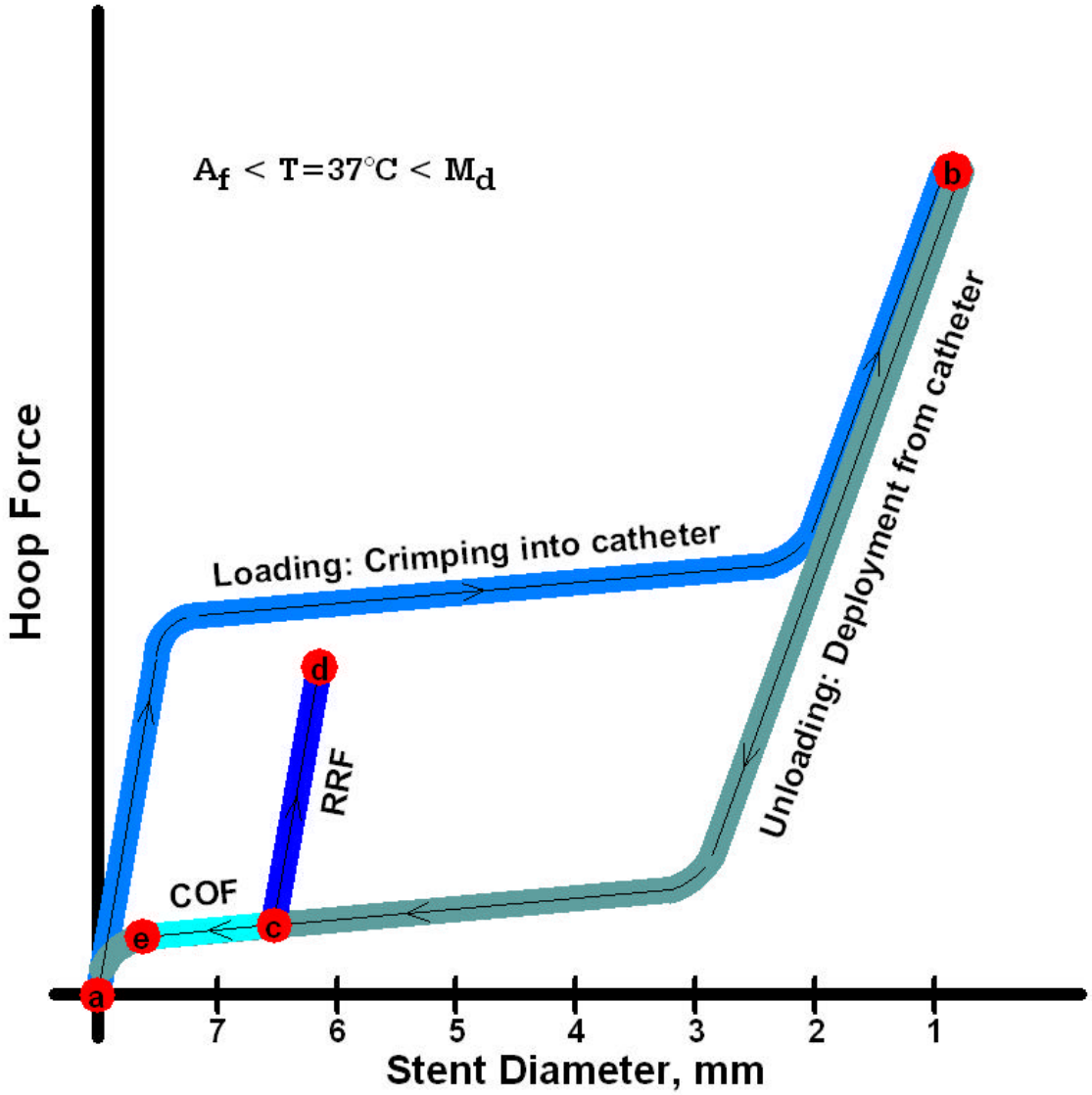

Figure 1.3: At body temperature, the superelastic effect is produced in an endovascular stent, resulting in a "biased stiffness" in operation (after [6]). During manufacture, the stent is compressed from an initially large diameter (a) to a small diameter (b) to fit within a catheter, resulting in transformation to martensite. During *in vivo* deployment from the catheter, the stent expands to a larger diameter (c) but is constrained from full recovery to (a) by the lumen walls. In operation, the stent exerts a mild chronic outward force (c-e) on the blood vessel, which keeps the stent and blood vessel open. To collapse the stent, and therefore the blood vessel, requires the addition of significant hoop force (c-d). This resistance to collapse from (c-d) is called a radial resistive force, RRF, and requires elastic loading of the austenite phase.

1.5 Objective of this Work

Since its discovery nearly a half century ago, much research has been conducted on Nitinol's unique mechanical response [6-8, 31-36], fatigue and fracture properties [20,

21, 31, 37-74], and phase transformation [8, 13, 31, 75-77]. However, there is a dearth of information in the literature regarding those responses and properties in a product form that is relevant to biomedical devices: Nitinol tube. Motivated by the cited failures of many hundreds of stents *in vivo* [78-89], as well as personal experience with investigation of failed biomedical devices, it is the primary goal of this research to determine the fracture and fatigue properties, and the relevant microstructural variables, that influence the failure of Nitinol tube.

The remainder of this document is organized as follows. Chapter 2 reviews the material that was used to accurately mimic Nitinol stent material, and the experimental procedures utilized to determine the relevant fracture mechanics data. Chapter 3 characterizes the crystallographic alignment of atoms, i.e. texture, of a variety of Nitinol product forms and annealing heat treatments. Chapters 4 and 5 are respectively devoted to the determination of the fracture toughness and the fatigue-crack growth behavior, both critical in estimating the susceptibility of Nitinol to *in vivo* failure. The highly localized (~1 μm resolution) effects of microstructure immediately ahead of a growing crack tip were studied by synchrotron x-ray micro-diffraction at the Advanced Light Source (Lawrence Berkeley National Laboratories, Berkeley, CA), with the results given in Chapter 6. Chapter 7 provides a simple engineering design criterion, based upon the results in the earlier chapters, for evaluating the susceptibility of a Nitinol biomedical device to failure by fatigue, overload fracture, or both. Finally, concluding remarks and a discussion of potential future work is given in Chapter 8.

CHAPTER 2: EXPERIMENTAL PROCEDURES

2.1 Material

Nitinol (Ti, 50.8 at.% Ni) in the form of tubing, sheet, and rod was received from Nitinol Devices & Components, Inc. (NDC, Fremont, CA). All samples were processed from multi-vacuum-arc remelted (VAR) material and had an austenite transformation finish temperature (A_f) of 30°C or below. Accordingly all samples were fully austenitic at test temperatures, transforming to martensite (SIM) only when stress was applied to the samples.

The thin-walled tube was received in two conditions: a) as-received (drawn plus straightened via thermomechanical processing) with dimensions 4.6 mm outer diameter and 3.9 mm inner diameter), and b) flattened. Much of the Nitinol tubing was flattened such that standard geometries (e.g. compact tension, C(T), and dogbone) could be fabricated for fracture mechanics testing. The flattening procedure, which is similar to the shape-setting procedure used in stent manufacture, is described below and schematically shown in Fig. 2.1.

a) superelastic Ti-50.8Ni (atomic %) tubing with 5.84 mm OD x 4.98 mm ID was laser cut longitudinally so the tube could be uncurled.
b) laser cut pieces were then flattened through a series of five thermo-mechanical shape-setting procedures to form flat strips of 76.2 mm x 17.0 mm.
c) resulting flat strips were annealed to produce an A_f of 28°C.
d) after heat treatment, the strips were laser cut to form dog-bone and compact tension shaped test samples at various angles to the original tube drawing direction.
e) laser cut samples were microblasted with 1200-grit alumina and electropolished to remove the laser-affected zone and to achieve a uniform surface finish and passive oxide.

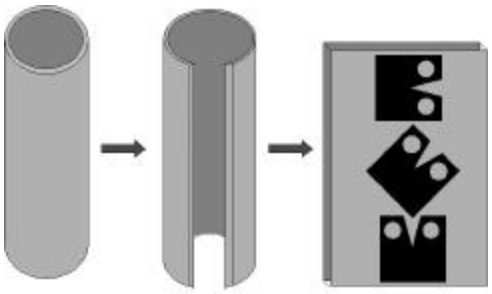

Figure 2.1: Schematic illustration depicting the procedures used to produce standard compact-tension C(T) specimens from an originally tube-shaped geometry. The tube is first longitudinally laser cut, then unrolled through a series of shape-setting procedures, followed by laser machining of the C(T) specimens from the flattened configuration in a variety of angles to the drawing direction.

With the exception of the microdiffraction work, all tests conducted in the flattened tube (texture, fracture toughness, and fatigue crack growth) were performed on as-processed flatted tube such that the microstructural conditions (nano-scale grains) were nominally equivalent to an endovascular stent. Microdiffraction studies required larger grain sizes and hence the material was annealed at 700-750°C for 10-30 min. to grow the grains to ~25 μm average size.

The sheet was received as 0.90-mm thick, as-rolled material. Two rod samples were also obtained from NDC with diameters of 15 and 41 mm. The 15 mm diameter is the predecessor to the deep-drawn tubing described above, whereas the 41 mm diameter material is similar to the Nitinol rods that are being proposed for use in structural applications, such as earthquake-proofing civil structures

2.2 Heat Treatments

The effect of annealing heat treatments on the tube and sheet texture was studied using as-received materials that were processed to the following conditions:

- *"485" condition:* as-received material was reheated for 5 min at 485°C (~ 0.5 T_m, where T_m is the melting temperature) in an air furnace, followed by an ice-water quench. This heat treatment is common in the Nitinol industry and serves only to stress relieve, slightly lower the tensile strength, and slightly raise the A_f.
- *"850" condition:* as-received Nitinol was annealed *in vacuo* at 850°C (~ 0.7 T_m) for 30 min followed by a slow cool (10°C per min). This heat treatment does not fully normalize the microstructure, but is used here as it represents a typical industry anneal for studying large-grain phenomena.
- *"1100" condition:* as-received Nitinol was annealed *in vacuo* for 12 hr at 1100°C (~ 0.85 T_m), followed by an ice-water quench. The rationale for this heat treatment was to relieve processing residual stresses, to recrystallize the material, and to eliminate the R-phase.

The specific transformation temperatures for each raw material form are given in Table 2.1, with corresponding optical micrographs presented in Fig. 2.2. Several of these micrographs show the presence of martensitic grains (needle-like appearance); however, these are polishing artifacts as the stresses from grinding and polishing cause transformation in exposed grains which leaves residual surface relief on etching. Moreover, the apparent grain sizes of ~20 μm, observed with optical microscopy for the "485" conditions, also give a false impression; there exist much smaller "sub-grains" (~ 10 nm) that can only be revealed by transmission electron microscopy [90].

Table 2.1: Transformation temperatures and average grain sizes for the eight sample conditions described in Sections 2.1 and 2.2.

Condition		Transformation Temperatures*, °C						Ave Grain
		R_s	R_f	M_s	M_f	A_s	A_f	Size, μm
Tube	485°C, 5 min	22	0	-47	-90	16	28	25**
	850°C, 30 min	0	-27	-54	-68	-8	4	40
	1100°C, 720 min	n/a	n/a	-52	-72	-42	-29	75
	flattened	25	13	-26	-63	12	26	25
Sheet	0.90 mm, 485°C, 5 min	13	5	25	3	13	30	50**
	0.90 mm, 850°C, 30 min	-35	-6	-57	-76	-7	2	75
Rod	15 mm ϕ	-60	-32	-58	-90	-35	-20	90

41 mm ϕ	23	11	-27	-55	14	30	90

* Determined by Differential Scanning Calorimetry (tangent intercept method). R_s, R_f, M_s, M_f and A_s, A_f are, respectively, the R-phase, martensite and austenite start and finish temperatures

** These grain sizes represent the optical microscope resolved dimensions. Transmission electron microscopy above 50,000X magnification reveals a sub-grain structure of ~10 nm average size, which are annihilated at the higher temperature heat treatments [90].

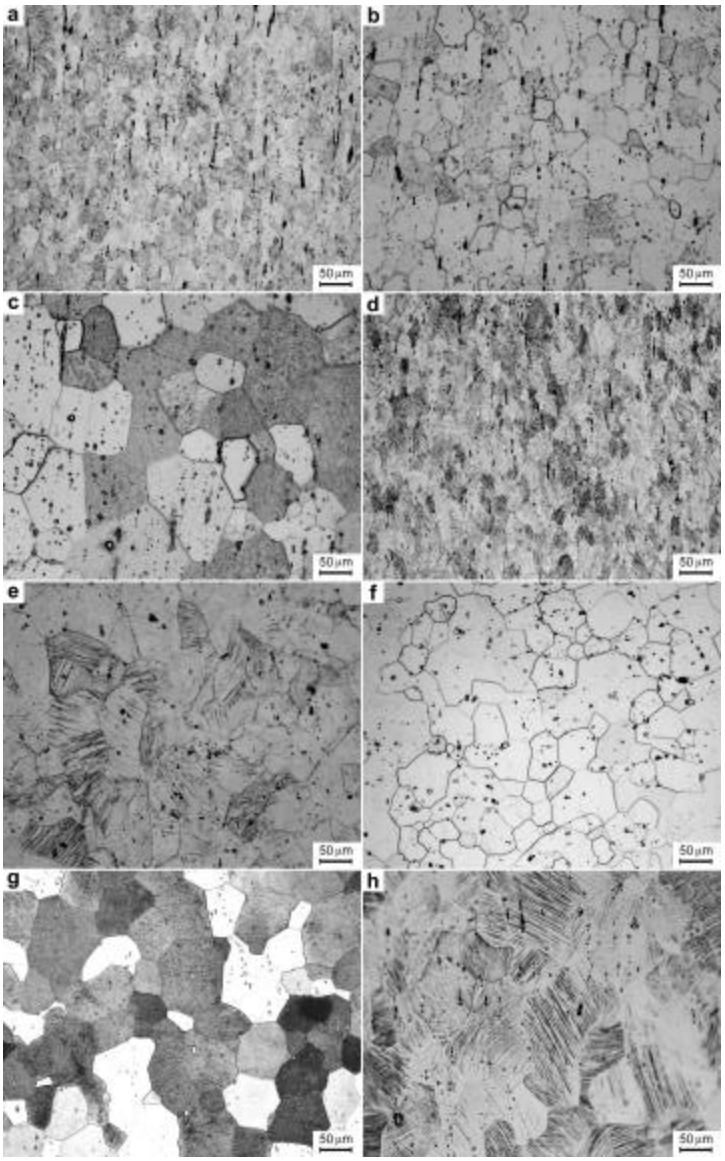

Figure 2.2: Photo-micrographs of the eight raw material forms documented in Table 2.1; (a) tube, 485°C (~0.50T_m), 5 min, quench, (b) tube, 850°C (~0.70T_m), 30 min, -10°C/min, (c) tube, 1100°C (~0.85T_m), (d) tube, flattened through a nine-step thermo-mechanical shape-setting process, (e) 0.90 mm thick sheet, 485°C (~0.50T_m), 5 min, quench, (f) 0.90 mm thick sheet, 850°C (~0.70T_m), 30 min, -10°C/min, (g) 15 mm diameter rod, no heat treatment, (h) 41 mm diameter rod, no heat treatment. Etchant: 3.2% HF, 14.6% HNO_3, balance deionized water. The drawing/rolling direction is vertical.

2.3 Texture Analysis

Crystallographic textures were measured in reflection geometry with a Huber x-ray pole figure goniometer, with Cu-Ka radiation source at 40 kV and 14 mA, and a graphite monochromator. To provide large enough flat samples, the tubes were sliced into sections, the sections were then lined up side-by-side to form an approximate 10 mm square, cold-mounted in epoxy and polished flat. All tube and sheet samples were mechanically ground and polished to a 0.05 μm finish to permit optimal reflective x-ray diffraction and establish consistency among the samples. The rod samples were longitudinally laser cut and electropolished to remove any machining effects. All samples were heated to ~50°C prior to testing and slow cooled back to room temperature to ensure they were fully austenitic throughout the test.

The crystallographic texture of the Nitinol was determined from three "incomplete measured" pole figures, namely the 110, 200 and 211 diffraction peaks, at ? values of, respectively, 21.3°, 30.8° and 38.9° for Cu-Ka radiation, where ? is half of the angle between the incident x-rays and the detector. The raw intensities were corrected for background and defocusing and only data out to a maximum tilt angle distance of 65º were used. The Williams-Imhof-Matthies-Vinel (WIMV) algorithm [91], which calculates orientation distributions from pole figures, was employed in the BEARTEX software package for quantitative texture analysis in order to obtain the orientation distribution functions (ODF) [92]. From the ODF, pole figures and inverse pole figures were recalculated following standard smoothing and rotation operations. The smoothing operation was performed mainly to reduce the effects (if any) of highly oriented single

crystals in the bulk sample. Rotation was necessary to orient each pole figure in the sample reference orientation for comparison among the samples.

Except for the flattened tube, the experimental pole figures for the Nitinol tube samples represent the average of three separate tests. For the Nitinol sheet, rod, and flattened tube samples, only one test was used in the texture analysis because of limited sample supply. However, each sample was tested multiple times and yielded nearly identical results each time.

2.4 Uniaxial Tension Testing

Standard "dog-bone" tensile specimens were laser machined from the flattened tube at orientations longitudinal, circumferential, 22.5°, 45°, and 67.5° to the tube drawing direction. Dog-bone gauge dimensions were nominally 0.75 mm wide, 0.40 mm thick, and 7.5 mm long. Uniaxial tensile testing was performed on an EnduraTEC/BOSE desktop tester ELF3200 (ELectroForce) series. A customized air-heating chamber was used to maintain a temperature of 37°C during testing at a crosshead displacement rate of 4.0 μm/sec to ensure adiabatic conditions. Strains were determined from a miniature extensometer with gauge length of 3.00mm.

2.5 Fracture Mechanics Testing

All fatigue and fracture tests were conducted using an automated servo-hydraulic MTS mechanical testing system. The C(T) specimens were machined from flattened Nitinol tube 12 mm square with a thickness of 0.37-0.41 mm. Each sample was submerged in boiling water for 5 sec immediately prior to testing to raise the sample temperature significantly above the A_f to transform any residual martensite to austenite.

Samples were then allowed to equilibrate to the testing temperature, 37°C, for 10 to 20 min prior to starting each test. All fatigue-crack growth and fracture toughness data presented herein represent the average of at least four independent tests per condition (n = 4). The specific details pertaining to the fracture toughness and fatigue testing are given in the following subsections.

2.5.1 Fracture Toughness Measurement

Specimens were machined with the starter notches oriented in one of three configurations: longitudinal (i.e., in the drawing direction), 45° to the drawing direction, and circumferential (Fig. 2.1). Each sample was first fatigue pre-cracked prior to toughness testing at low *R*-ratio, near-threshold stress intensities (< 5 MPa$\sqrt{m}$) to produce a nominally atomically sharp flaw, with a crack-length to sample width ratio of $a/W \sim 0.45$. Toughness tests were then conducted in air (to allow the measurement of crack extension by telescope with a resolution of 1 μm), with the temperature maintained at 37°C inside an enclosure surrounding the servo-hydraulic test system. Using a crosshead displacement rate of 400 nm/sec, stable crack growth was monitored from $a/W \sim 0.45$ to 0.60, in general accordance with ASTM E399 [93]; corresponding measurements of the crack extension, Δa, as a function of the applied stress intensity, were then used to determine the crack-resistance or R-curves as a function of specimen orientation.

2.5.2 Fatigue Crack Growth Setup

Unlike the fracture toughness tests which studied the effects of crack orientation on fracture, the specimens used for fatigue-crack growth studies were all cut with the crack-growth direction oriented at 45° to the tube drawing direction because the experiments in

Chapter 5 showed that fatigue-crack extension favored this direction regardless of the initial orientation of the pre-notch.

In vitro fatigue-crack growth rates measurements were conducted with custom-designed grips containing a reservoir for containment of a simulated body fluid, Hanks' Balanced Salt Solution (HBSS)[1], with laminar fluid flow controlled via a valve-regulated submerged hydraulic pump at a rate of approximately 50ml/min across the fatigue specimens. Fluid was maintained at a temperature of 37°C and pH of 7.4 to simulate *in vivo* conditions. Deleterious bacterial growth was inhibited by Gentamicin at a ratio of 2ml/l of HBSS. Testing was performed in force control at a cyclic loading frequency of 50 Hz (sine wave), except where the frequency was lowered to 1 Hz to simulate the human sinus rhythm, over a range of positive load ratios (ratio of minimum to maximum load) of R = 0.1, 0.5 and 0.7; crack lengths were continuously monitored with a capacitance-based load-line displacement gauge located on the grips. A computer-controlled feedback loop was utilized for K-control with a force shedding rate of –0.16 mm^{-1} during the slow growth phase of the fatigue curve, i.e., near the fatigue threshold, ΔK_{th}. The value of the ΔK_{th} threshold was operationally defined, as per ASTM E647 [94], as the stress-intensity range, $?K = K_{max} - K_{min}$, to give a growth rate, da/dN, of 10^{-10} m/cycle, based on linear extrapolation of data between 10^{-9} and 10^{-10} m/cycle.

2.6 Characterization by X-ray Micro-diffraction

To investigate the microstructural changes that occur locally at a growing crack in Nitinol, a technique was developed that combined micro-mechanical loading of C(T)

[1] Chemical formulation (in g/L of deionized water): 8.00 Sodium Chloride, 0.05 Sodium Phosphate Dibasic, 0.40 Potassium Chloride, 0.06 Potassium Phosphate Monobasic, 0.098 Magnesium Sulfate (anhydrous), 0.14 Calcium Chloride (anhydrous), D-Glucose (anhydrous), and 0.01 Phenol Red colorant

specimens with *in situ* high-resolution imaging with x-ray micro-diffraction (at Beamline 7.3.3 at the Advanced Light Source synchrotron radiation facility, Berkeley, CA). The C(T) specimens were fatigue pre-cracked, per Section 2.5.2, at near threshold stress intensities (~3 MPa$\sqrt{m}$ at R = 0.1) to generate an atomically-sharp crack with minimal residual stress prior to being loaded on the beamline with an *in situ* micro-tensile loading device. The custom-designed tensile loading apparatus was displacement-controlled via a stepper motor traversing at 0.25 μm/s, with a force capacity of 100N. Using the synchrotron radiation source at the ALS, Laue diffraction patterns were obtained under white-beam conditions (photon energy 5-14 keV) from very highly localized regions (spot size <1 μm diameter) in the vicinity of the crack tip.

Each specimen used for this studied was annealed at 700-750°C for 10-30 minutes in order to grow the grains to an average size of 25 μm, i.e., to a size where diffraction scans (with a spot size of ~1 μm) could result in several diffraction patterns collected per grain to accurately measure grain-by-grain and intergranular strains. The specimens were further heat treated (475-500°C, 3-5 min.) to tune the A_f to ~15°C such that testing at room temperature would have the same relative deviation (~7°C) as experienced by a stent in the human body (A_f ~ 30°C, body temperature ~ 37°C).

CHAPTER 3: NITINOL TEXTURE

3.1 Introduction

When conventional engineering materials, such as stainless steel, are mechanically loaded, they undergo typically less than 1% elastic deformation (which is completely recoverable), followed by plastic deformation (which is permanent). Nitinol, a nearly equiatomic nickel-titanium alloy, responds differently; its elastic response is followed by a stress-induced phase transformation from a cubic (austenite) phase to a monoclinic (martensite) phase that can result in fully recoverable macroscopic strains as high as 8% or more. On unloading, the martensite becomes unstable and fully transforms back to austenite, with a concomitant macroscopic strain recovery phenomenon referred to as superelastity. As these martensitic phase transformations depend on coordinated atomic movements, any significant alignment of the atomic planes, i.e., texturing, in the polycrystalline material can have a marked influence on the mechanical response by either limiting or promoting the transformation.

Previous work [95-106] has shown that in drawn and heat-treated sheet or bar, the mechanical properties of Nitinol are strongly influenced by the texture. In particular, Gall and Sehitoglu [95] concluded that texture, and consequently the martensite variants active during the transformation, are the source of the compression-tension asymmetry in Nitinol. Similarly, Gao and Yi [96] demonstrated a marked influence of texture on the elastic modulus, transformation stress, and transformation strain in Nitinol, and Vaidyanathan *et al*. [105] showed that texturing occurs in Nitinol only when martensite is stress-induced from austenite. Despite the obvious significance of texture on the mechanical performance of Nitinol, there have been few studies that quantify this texture,

particularly in tubing that is used in one of the most important applications of the alloy, that of the manufacture of endovascular stents and other biomedical devices.

Accordingly, it is the objective of the this chapter to seek further understanding of how processing and heat treatment can affect the texture in Nitinol, specifically by quantifying the texture of a variety of raw material forms and heat treatments. The motivation for this investigation is to provide a comparison of the texture of the Nitinol tubes that are used in the fabrication of many biomedical devices (e.g., stents, vena cava filters) with other product forms (sheet and rod), and to determine if annealing heat treatments can be utilized to change the strength and orientation of the texture in order to vary the mechanical response.

3.2 Product Form Comparison

To determine the role of product form, pole figures and inverse pole figures for tube, sheet, and rod with nominally similar heat treatment were compared. Using Fig. 3.1 to define the legends for all pole figures and inverse pole figures shown in this chapter, it is apparent from Fig. 3.2 that although the intensity, or the relative texture strength, is approximately the same, the specific nature of the texture depends markedly on the form of the raw material. The texture of the sheet is characteristic of hot-rolled body-centered-cubic (bcc) materials, as is the 110 fiber texture for the rod [107].

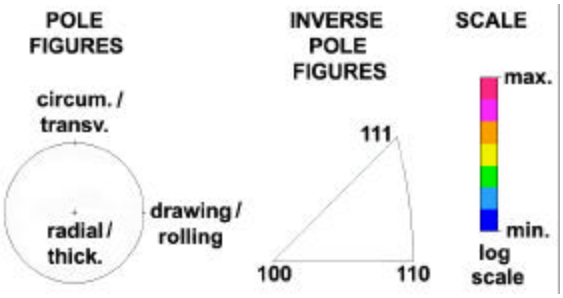

Figure 3.1: Legend for the pole figures (stereographic projection) and inverse pole figures (equal area projection). Intensities for every texture figure in this text are plotted on the same logarithmic scale from 100 (min) to 600 (max), i.e. 1-times to 6-times random distribution.

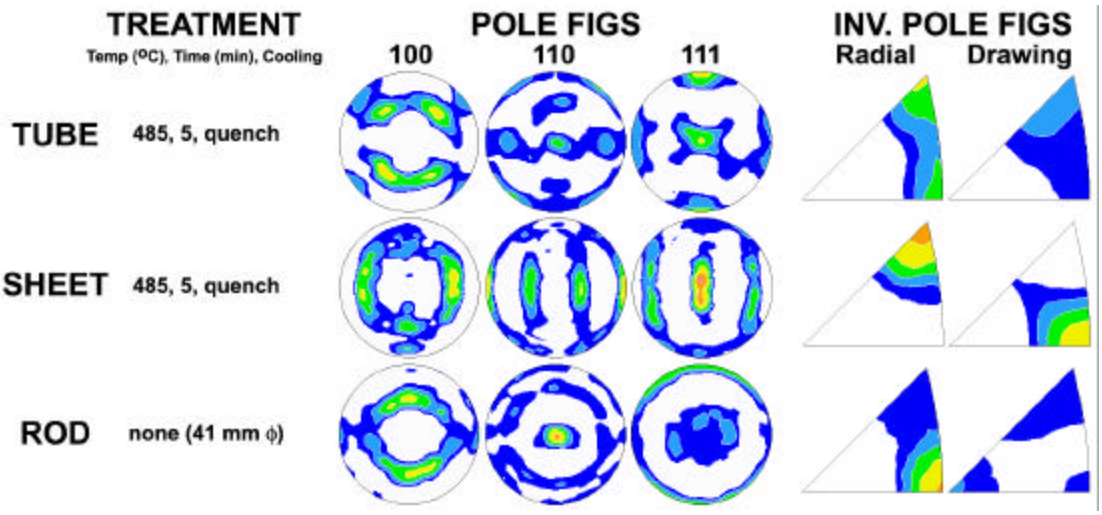

Figure 3.2: Raw material form texture comparison: tube, sheet, and rod, showing significant variation between the product forms.

To reproduce the effect of processing that a product may undergo during manufacturing, i.e., through the shape-setting procedure, tube samples were longitudinally cut and flattened. Despite the severity of the flattening process in this sample, the texture of the tube remained relatively constant (Fig. 3.3). The only significant difference in the "485" versus the flattened tube is the redistribution of 111 poles from the circumferential to the drawing direction.

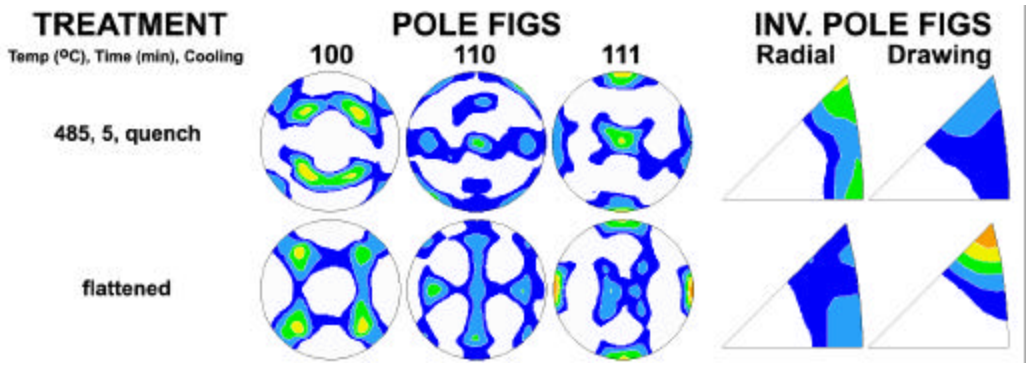

Figure 3.3: Texture effects as a function of shape-set processing, showing generally the same texture with the exception of a redistribution of 111 texture from the radial to drawing direction upon flattening.

With the results from the tube showing consistency in texture following mechanical processing, it was quite surprising to discover widely varying textures in rod (Fig. 3.4) of various dimensions and lots. The texture from two different diameter rods was quite different (Fig. 3.4). The 15 mm diameter rod, which is the precursor to the deep-drawn tubes that were analyzed in Fig. 3.3, exhibited an extremely high texture strength and highly localized texture components. Comparison of the 15 mm diameter rod texture (Fig. 3.4) with that of the "485" tube (Fig. 3.3) shows distinctly different textures following the processing. It is interesting that the severe process of deep-drawing a rod into a tube shape has a profound impact on the texture, whereas the process of flattening or uncurling the tube resulted in minimal textural changes. This observation suggests that although the form of the starting material has a marked effect on the texture, the shape setting procedures produce little change. These results are of significance for biomedical Nitinol components, as most manufacturers use some form of shape setting or material "training" during processing.

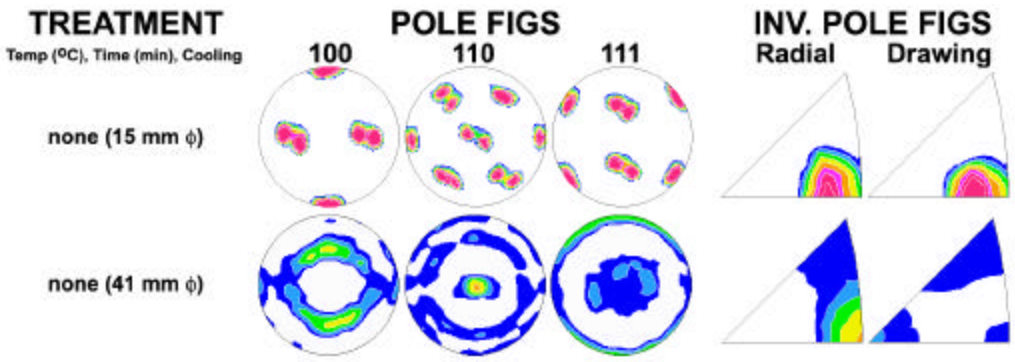

Figure 3.4: Rod material comparisons showing nearly single crystal texture in the 15 mm diameter rod, and lower texture intensity in the 41 mm diameter rod texture, and are both significantly different than tube.

3.3 Heat Treatment Comparison

As most biomedical Nitinol products undergo some form of heat treatment to "tune" the transformation temperatures, it is important to understand the effect of such treatments on the texture of Nitinol. In this section, the effect of annealing heat treatments was primarily evaluated on tubular raw material form, which is most widely used in the biomedical community, although sheet samples were also examined for comparison.

Unlike many engineering alloys that normalize, or randomize, their grain structure following annealing heat treatments at high homologous temperatures, the strength of the texture in Nitinol was found to be increased. This is indicated by the progressively higher intensity (relative density of red in the pole figures) as the annealing temperatures and times increase (Fig. 3.5). The inverse pole figures demonstrate a progressive redistribution of texture from 111 and 110 poles in both radial and drawing directions in the "485" condition, to 111 radial and 110 drawing direction textures. Except for these differences, the tube texture remains generally similar throughout the heat treatment process.

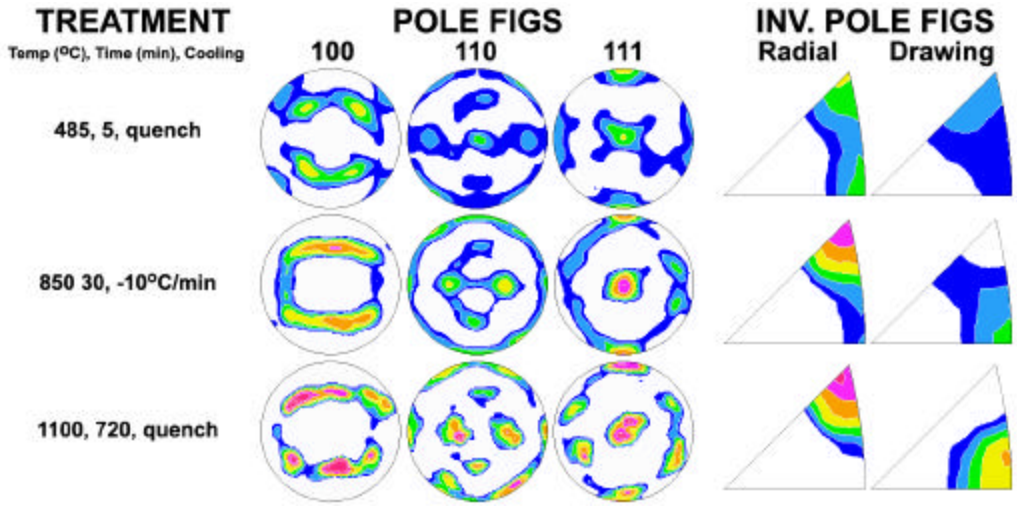

Figure 3.5: Effect of annealing heat treatment on the texture of Nitinol thin-walled tube, showing a progressive strengthening of texture and slight redistribution of towards of the 111 poles in the radial direction upon increased annealing time.

Sheet material exhibits the same trend of increasing texture intensity with increasing heat treatment (Fig 3.6). The sheet texture also redistributes upon heating, and grows from predominantly 111 radial and 110 drawing to 111 and 110 radial and strong 110 drawing texture.

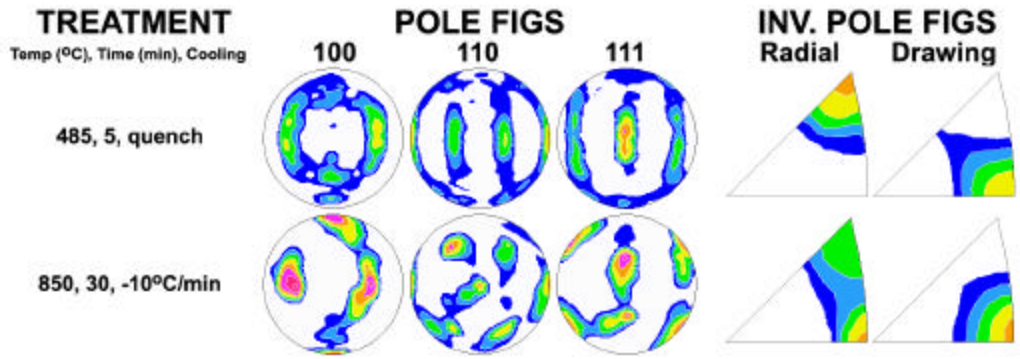

Figure 3.6: Effect of annealing heat treatment on texture in 0.90 mm thick Nitinol sheet, showing a similar strengthening of texture as the tube product form.

Textures measured for Nitinol sheet compare favorably with previous measurements cited in the literature [98, 100, 101], although there are no other reported data on the texture of Nitinol tubes. Specifically, the current textures for 0.90 mm thick "485" sheet are very similar to those determined by Monasevich *et al*. [101], Li *et al*. [100], and Inoue *et al*. [98] on other Nitinol plate and sheet geometries. However, pole figures derived by Kitamura *et al*. [99] are quite different, presumably because their study was focused on a much thinner (100 μm) Nitinol sheet; they showed a texture maximum of the 110 pole normal to the sheet, which was not observed in the present study.[2]

[2] 110 normal-direction texture was observed in a different Ni-rich (55.5 at. %) Nitinol material (not included in this dissertation) processed by both vacuum-induction-melting and vacuum-arc-melting (VIM-VAR). Unlike the multi-VAR material used here, due to interaction with the crucible, the VIM-VAR process leads to a different as-cast structure and a higher carbon content (0.07 at. % C in this alloy), which may be responsible for the 110 normal-direction texture.

3.4 Texture Quantification

Quantification of the major components of textures in each set of samples was performed using the BEARTEX software; results are presented in Tables 3.1 through 3.3 and show the texture components representing 4% or more of the total volume, with the remainder assumed to be randomly distributed. In these tables, each Euler-angle-described component was approximated as a Miller index pair {hkl}<uvw> representing the {hkl} plane families normal to the radial/thickness direction, and <uvw> direction families parallel to the drawing/rolling direction.

Table 3.1 shows a shift in the major textural component from a {-110}<223> in the "485" sample to a {-111}<13-2> and {-212}<120> in the "850" and "1100" samples, respectively. In addition, there is a trend of increasing texture from 40% in the "485" to a surprising 82% in the "1100", indicating a structured recrystallization upon heat treatment. Interestingly, 73% of the grains in the "1100" tube sample can be described by solely two texture components, {-212}<120> or {-432}<14-4>. Although it was previously stated that the "485" and flattened tubes appeared to have similar textures, their quantified results show distinct differences. However, as the major component in each sample both represent ~27% of the texture volume and differ by only 8 degrees in α–Euler space, it is fair to conclude that the textures are similar with only minor differences.

Table 3.1: Quantified textures for tube raw material form.

CONDITION	COMPONENT EULER ANGLES ($\alpha, \beta, \gamma, \Delta\beta$)	APPROX. MILLER INDEX {hkl}<uvw>	VOL %
485°C, 5 min	45, 45, 0, 20	$\{\bar{1}10\}\langle 223\rangle$	26
	30, 56, 45, 15	$\{\bar{1}11\}\langle 110\rangle$	10
	0, 57, 45, 10	$\{\bar{1}11\}\langle 211\rangle$	4
850°C, 30 min	45, 58, 45, 12	$\{\bar{1}11\}\langle 13\bar{2}\rangle$	20
	55, 45, 0, 15	$\{\bar{1}10\}\langle 112\rangle$	10
	90, 45, 45, 10	$\{\bar{2}23\}\langle 110\rangle$	8
	275, 40, 25, 10	$\{\bar{2}13\}\langle 120\rangle$	5
1100°C, 12 hr	270, 48, 25, 20	$\{\bar{2}12\}\langle 120\rangle$	40
	41, 70, 35, 15	$\{\bar{4}32\}\langle 14\bar{4}\rangle$	33
	120, 50, 35, 15	$\{\bar{3}23\}\langle 432\rangle$	5
	330, 55, 45, 15	$\{\bar{1}11\}\langle 110\rangle$	4
Flattened	37, 45, 0, 20	$\{\bar{1}01\}\langle 1\bar{1}1\rangle$	28
	0, 35, 45, 15	$\{\bar{1}12\}\langle 1\bar{1}1\rangle$	11
	287, 50, 35, 10	$\{\bar{3}23\}\langle 331\rangle$	8
	219, 66, 26, 15	$\{\bar{2}11\}\langle 01\bar{1}\rangle$	5

Like the tubes, the sheet samples (Table 3.2) produced similar increased texture volume percentages with increasing heat treatment time and temperature; the sheet increased from ~40% total texture in the "485" to 75% texture in the "850" sample. This spike in texture volume occurred at a lower annealing temperature and time than in the tube, which went from 40% to only 43% texture for the same heat treatment. This difference could be associated with the difference in thickness of the samples, as the tubes were 0.37 mm thick whereas the sheet was 0.90 mm thick. It is presumed that the additional geometric constraint in the tube samples inhibited crystal redistribution at the medium heat-treated condition. It is also possible that prior deformation, i.e., the extent of drawing or rolling, or the pre-existing texture itself, may play a role in preventing or promoting recrystallization in the different raw material forms.

Table 3.2: Quantified textures for sheet raw material form.

CONDITION	COMPONENT EULER ANGLES ($\alpha, \beta, \gamma, \Delta\beta$)	APPROX. MILLER INDEX {hkl}<uvw>	VOL %
0.90 mm thick 485°C, 5 min	60, 45, 45, 15	$\{11\bar{1}\}\langle 112\rangle$	15
	270, 45, 45, 15	$\{\bar{2}23\}\langle 110\rangle$	13
	270, 75, 45, 15	$\{\bar{2}21\}\langle 110\rangle$	11
0.90 mm thick 850°C, 30 min	313, 45, 35, 25	$\{\bar{4}35\}\langle 312\rangle$*	45
	0, 45, 0, 20	$\{\bar{1}10\}\langle 110\rangle$	30

* This orientation pair is not perfectly co-planar; however, it represents the nearest low-index correlation.

Approximately 60% of the 15 mm diameter rod crystallites were represented by a sole texture component, {-203}<302>, (Table 3.3). Conversely, the larger 41 mm diameter rod exhibited an even distribution, ~10% each, of four different texture components. The exact source of such pronounced texture in the one rod sample and not the other is uncertain, but one can speculate that it is due to the prior degree of mechanical working and/or geometric effects.

Table 3.3: Quantified textures for rod raw material form.

CONDITION	COMPONENT EULER ANGLES ($\alpha, \beta, \gamma, \Delta\beta$)	APPROX. MILLER INDEX {hkl}<uvw>	VOL %
15 mm ϕ	0, 35, 0 10	$\{\bar{2}03\}\langle 302\rangle$	60
	0, 56, 15, 10	$\{\bar{3}12\}\langle 203\rangle$	12
41 mm ϕ	90, 45, 0, 15	$\{\bar{1}10\}\langle 001\rangle$	10
	35, 45, 0, 15	$\{\bar{1}10\}\langle 111\rangle$	10
	0, 45, 0, 20	$\{\bar{1}10\}\langle 110\rangle$	9
	125, 45, 0, 15	$\{\bar{1}10\}\langle 112\rangle$	8

In light of these findings, it is clear that selection of the appropriate raw material product form is critical to obtaining accurate mechanical test results when characterizing Nitinol materials, particularly in proof testing for quality assurance. In addition, a critical

finding is that the texture of Nitinol materials cannot be removed, or even reduced, in these product forms using standard annealing or normalization heat treatment procedures.

3.5 Texture-Dependent Mechanical Behavior

To demonstrate the effect of texture on the mechanical properties of Nitinol, the strains at the end of the transformation stress plateau (i.e., on the stress/strain curve) were estimated. Following the technique of Yuan and Yi [106] for textured Nitinol sheet, this transformation strain can be calculated from the modified Taylor factors derived by Ono *et al*. [108, 109] for polycrystalline Nitinol. Specifically, using optimization algorithms for the formation of the twelve variants of martensite, Ono *et al*. created a modified Taylor factor, *M'*, distribution map, as shown in Figure 3.7, which shows modified Taylor factors as a function of the texture in the tensile loading direction. Using this map and the inverse pole figures determined from the current experimental data, the transformation strain, e, was calculated from:

$$e = \frac{hV_m}{M'_{ave}} \quad , \tag{3.1}$$

where h is the maximum habit plane displacement magnitude (= 13.08 from ref.[109]), V_m is the volume fraction of martensite (= 1.00 for 100% conversion in this case), and M'_{ave} is the average modified Taylor factor:

$$M'_{ave} = \frac{\int \left(E(h,k,l) \times M'(h,k,l) \right)}{\int E(h,k,l)} \quad , \tag{3.2}$$

where E(h,k,l) is the discrete texture intensity at a given (h,k,l) Miller index position on the experimentally measured inverse pole figures, and M'(h,k,l) is the corresponding modified Taylor factor intensity from Figure 3.7. Thus, M'_{ave} represents the normalized Taylor factor for each specific polycrystalline form of Nitinol in this study.

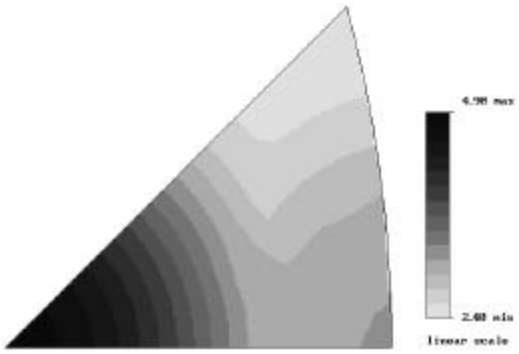

Figure 3.7: Modified Taylor factor distribution, *M'*, after Ono *et. al.* [109] showing the factor as a function of texture and uniaxial *tensile* loading direction.

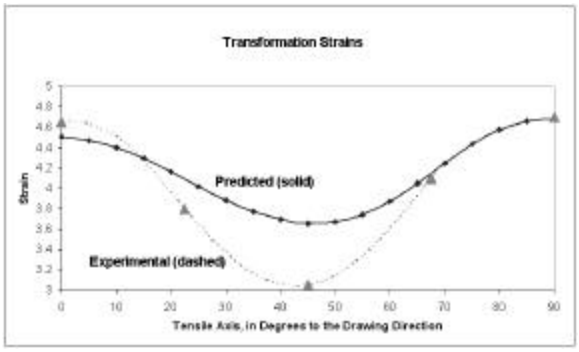

Figure 3.8: Texture-predicted *tensile* transformation strains versus loading angle relative to the drawing axis for flattened tube (solid line), with experimentally determined (by uniaxial tension tests) transformation strains (dashed line) showing good correlation; 16% maximum difference at 45°.

Inverse pole figures were produced for the flattened tube for inclined sample directions between 0 and 90 degrees, in 5 degree increments, with respect to the drawing direction. These inverse pole figures provided the necessary *E*(h,k,l) distributions to predict the flattened tube transformation strain as a function of applied load direction. The tensile transformation strain predictions are plotted in Figure 3.8, and clearly show that a lower strain is necessary for complete transformation when the sample is loaded parallel to the 45° direction. The transformation strains from the laboratory uniaxial tension experiments follow the same general trend as this predicted mechanical response. The discrepancy is surprisingly small, namely 16% maximum. The good agreement indicated that the modified Taylor factor calculations are a very good estimation to predict the transformation strain from the determined Nitinol texture. It is also of note that these predicted results are consistent with paths of fatigue cracks in this material which, irrespective of the path of maximum driving force, preferentially follow the 45°

direction, (see Chapter 5). Conversely, the strains predicted for complete transformation in compression have a reverse trend, see Figures 3.9 and 3.10.

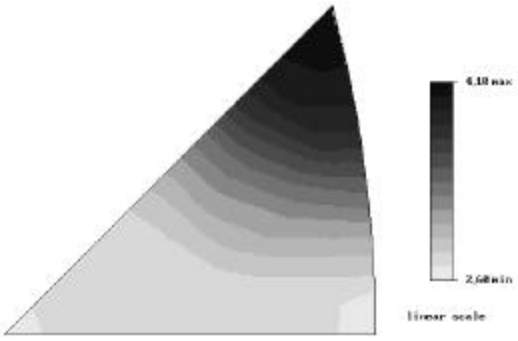

Figure 3.9: Modified Taylor factor distribution, *M'*, after Ono *et. al.* [109] showing the factor as a function of texture and uniaxial *compression* loading direction.

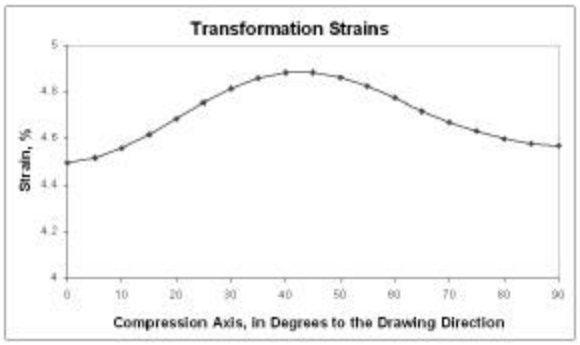

Figure 3.10: Texture-predicted *compression* transformation strains versus loading angle relative to the drawing axis for flattened tube showing a reverse trend to the *tensile* transformation strains predicted in Fig. 3.8.

Finally, Figure 3.11 shows the predicted transformational strains of the tube, sheet and rod raw material forms that are commonly used for industrial Nitinol products. The wide variability in the transformation strains for tube, rod and sheet demonstrates the need for quantification of texture in every raw material form appropriate for each Nitinol supplier and manufacturer.

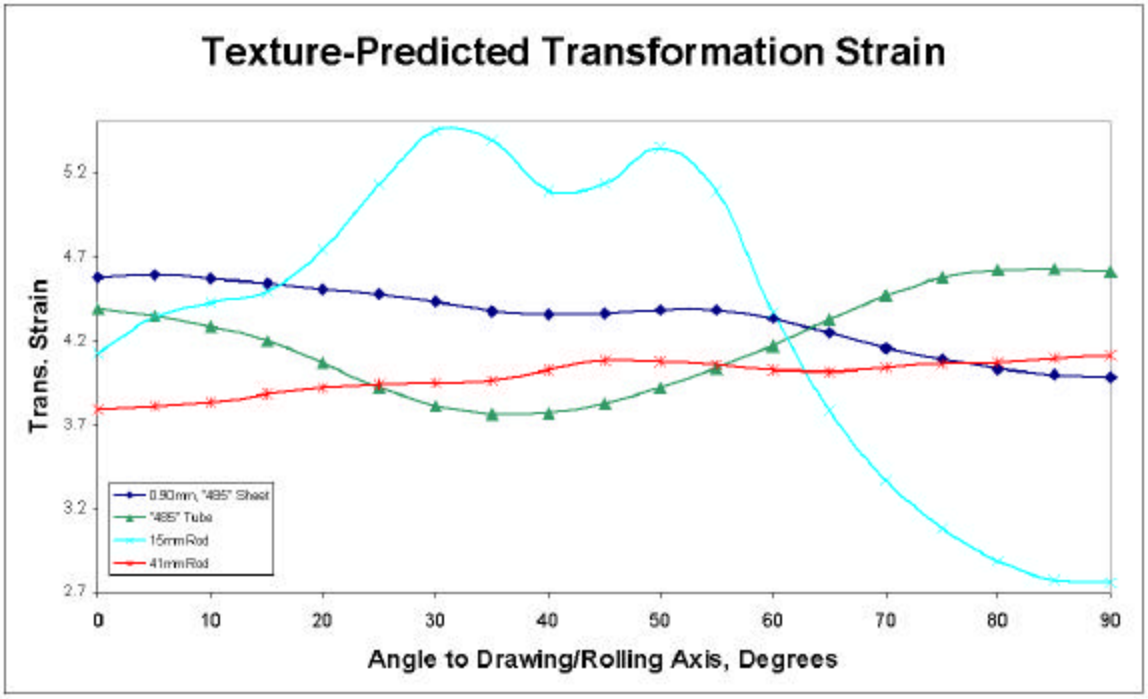

Figure 3.11: Texture-predicted *tensile* transformation strains versus loading angle relative to the drawing direction for tube and sheet Nitinol raw material forms.

3.6 Conclusions

Nitinol derives its unique mechanical behavior from the coordinated atomic movements manifesting in a phase transformations from cubic austenite to monoclinic martensite. Therefore, any significant alignment of the atomic planes from texture in the polycrystalline material can have a marked influence on the mechanical response by either limiting or promoting that phase transformation. The texture analysis presented in this chapter has shown that Nitinol does exhibit crystallographic orientation resulting from its forming and processing, which cannot be eliminated by annealing at high homologous temperatures up to ~0.85 T_m. Interpretation and quantification of the pole figures and inverse pole figures leads to the following specific conclusions:

1. Each material product form (tube, sheet and rod) possess a unique characteristic texture. Indeed, even rods of different diameter have widely different textures.

2. Annealing Nitinol tube and sheet for increasing time and temperature increases the crystallographic alignment in the sample. The location of the texture components, i.e., the Miller index quantification, however, remains somewhat constant upon continued annealing despite the increasing volume percent of textured grains. Annealing at ~0.5 T_m in sheet and ~0.85 T_m in tube resulted in over 70% of the crystallites distributed across only two principal texture components.
3. Shape-setting of tubular Nitinol does not significantly affect either the major texture component identity or its intensity. The only significant difference after the severe shape setting process of flattening a tube was found to be the redistribution of 111 texture from the circumferential to the drawing direction.
4. The texture of 15 mm diameter rod was highly oriented; specifically, 60% of the grains were oriented in the {-203}<302> direction. The manufacturing step of producing tubes from this rod via a deep-drawing step significantly changed the texture to a principal orientation of 26% {-110}<223>, and introduced a more evenly distributed texture over several components.
5. Experimental transformation strains were in good agreement with Taylor factor calculations for transformation to the twelve variants of martensite. These predictions and mechanical tests show that the transformation strain for Nitinol tube is lowest at a loading direction 35-45° to the drawing direction, and that texture in various raw material forms has a profound influence on the transformation strains.

It is for these very reasons that it became apparent that in order to estimate the fracture behavior of Nitinol stents, experimental testing ***must*** be performed in a product form that accurately mimics stent material. Therefore, the remainder of the tests presented herein were conducted exclusively on flattened Nitinol tube with nominally the same texture, microstructure, and phase transformation temperatures as endovascular stents.

CHAPTER 4: ORIENTATION-DEPENDENT FRACTURE TOUGHNESS

4.1 Introduction

Stresses from implantation and *in vivo* operation subject stents to a variety of overload stresses, for example from flexions of the joints or simply maneuvering the device through highly tortuous paths during implantation. These events can lead to "single-event" overload fracture potentially result in degraded performance or, in the worse-case scenario, complete failure of the device. Despite the recognized importance of this issue, the fracture toughness of Nitinol tubing has not been determined.

When reporting fracture toughness values for engineering applications, it is preferable to cite the plane strain (mode I) critical fracture toughness, K_{Ic}, as this is a true material constant. This value has never been measured for Nitinol. Indeed, there are only three reports of fracture toughness in the literature and each represents a highly specific condition [21, 54, 110], none of which are the plane strain (mode I) value.

When plane-strain conditions are not applicable such as in the case of biomedical devices (i.e. when the specimens are reasonably small[3]), toughness values may become both crack size and geometry dependent, resulting in elevated toughness values. However, in this case, since the goal is to determine the engineering parameter "fracture toughness" for a highly specific application, endovascular stents, the measure of toughness in these small C(T) specimens is more appropriate than the K_{Ic} values. Since the K_{Ic} value will invariable be lower than the toughness measured herein, design using

[3] Sample thickness, B, and crack length, a, typically assumed = $2.5(K_{Ic}/\sigma_y)^2$ for plane strain conditions [93. American Society of Testing Materials I, Subcommittee E08.06. E399: Standard test method for measurement of the plane strain fracture toughness in metallic materials. ASTM Book of Standards, 2005.].

that parameter may result in an overly conservative estimate of the fracture resistance resulting in unattainable design considerations.

4.2 Stress Intensity Calculations

Stress-intensity values, K, were calculated from standard handbook solutions [93, 111] for a compact tension specimen geometry using the following equations with a range of validity for 0.2 = a/W = 1:

$$K = \left(\frac{P}{B\sqrt{W}}\right) F\left(\frac{a}{W}\right), \text{ where} \tag{4.1}$$

$$F\left(\frac{a}{W}\right) = \frac{\left(2+\frac{a}{W}\right)\left(0.886+4.64\frac{a}{W}-13.32\left(\frac{a}{W}\right)^2+14.72\left(\frac{a}{W}\right)^3-5.6\left(\frac{a}{W}\right)^4\right)}{\left(1-\frac{a}{W}\right)^{3/2}}, \tag{4.2}$$

and where a is the crack length measured from the loadline (4-6 mm in these samples), W is the width of the specimen measured from the loadline (~10 mm), B is the sample thickness (~0.4 mm), and P the applied load.

As indicated by the texture results in Chapter 3, Nitinol has directionality-dependent mechanical properties. Thus, it came as no surprise that some cracks were inclined at an angle α (~25 deg) to the drawing direction, presumably due to texture. Therefore, fracture toughness values are presented as equivalent toughness values to account for that kinking, and are computed from the maximum strain-energy release rate, G, utilizing both mode I, k_I, and mode II, k_{II}, components, i.e.,

$$K_{eq} = [G(\alpha)E']^{1/2} = [k_I^2(\alpha) + k_{II}^2(\alpha)]^{1/2} \tag{4.3}$$

where E' is the appropriate elastic modulus, specifically, in plane stress $E' = E$ (Young's modulus), whereas in plane strain, $E' = E/(1 - \nu^2)$, where ν is Poisson's ratio. This approach compensates for the witnessed angled crack growth in the circumferentially-oriented samples. The angle was measured by optical microscopy following each experiment, and the crack extension was continually monitored throughout testing using a telescope with 1 μm accuracy.

4.3 Fracture Toughness Behavior

To simulate the types of stent fractures and failures that may result in numerous sites in the device from a single overload event, such as macroscopic bending/buckling of a superficial femoral artery stent in response to knee flexion, the fracture toughness of flattened Nitinol tube was evaluated at various angles to the tube drawing direction. Cracks grown from pre-notches oriented in the longitudinal and 45° directions propagated by pure mode I fracture, i.e., cracks did not kink from the pre-notch orientation. However, cracks grown from pre-notches oriented in the circumferential direction kinked from the pre-notch orientation producing a mixed-mode I + II loading configuration. Note that in terms of a crack-driving force, the effects of these differences in crack-path orientation are accounted for in the computation of the equivalent stress intensity K_{eq} (Eq. 4.3), but from an energetic viewpoint the cracks should not have diverged from the favorable mode I crack path unless the material microstructure (texture) overwhelmed this driving force, making a more energetically-favorable path along a mixed mode (kinked) orientation.

Results for all three sample configurations, namely circumferential, longitudinal and 45° fracture are shown in Fig. 4.1, and display so-called crack resistance or rising R-

curve behavior, i.e., the stress intensity to initiate and sustain subcritical cracking increases with initial crack extension. The fracture toughness at the onset of crack extension, i.e., as Δa ? 0, is known as the crack-initiation toughness, K_o, and is significantly lower than the toughness required to induce significant advance of the growing crack. In the present case, the initiation toughness values for Nitinol in the circumferential, 45° and longitudinal crack-growth orientations were 16, 10 and 27 MPa√m, respectively. It is suspected that the difference in initiation toughness values as a function of crack-growth angle is due to the influence of texture in the material, as previous reports have demonstrated variable mechanical properties as a function of angle to the drawing direction in processed Nitinol sheet [96] and in this work with tube (Chapter 2). Specifically, these studies show that the tensile stress [96] and strain (see Chapter 2) required to initiate the austenite-to-martensite phase transformation are significantly lower in the 45° direction to the drawing direction, which is in good agreement with the fatigue-crack growth results (Chapter 5) showing lowest crack-initiation toughness values in that direction. Despite significantly different crack-initiation values, all three sample configurations reach the same steady-state fracture toughness value of K_{ss} ~ 34 MPa√m. The presence of an R-curve in this material suggests that there are competing effects ahead of the crack tip, and in the plastic wake of the growing crack. These competing effects may be due to such factors as superelasticity, modulus mismatch between the austenite and martensite phases, and crystallographic texture.

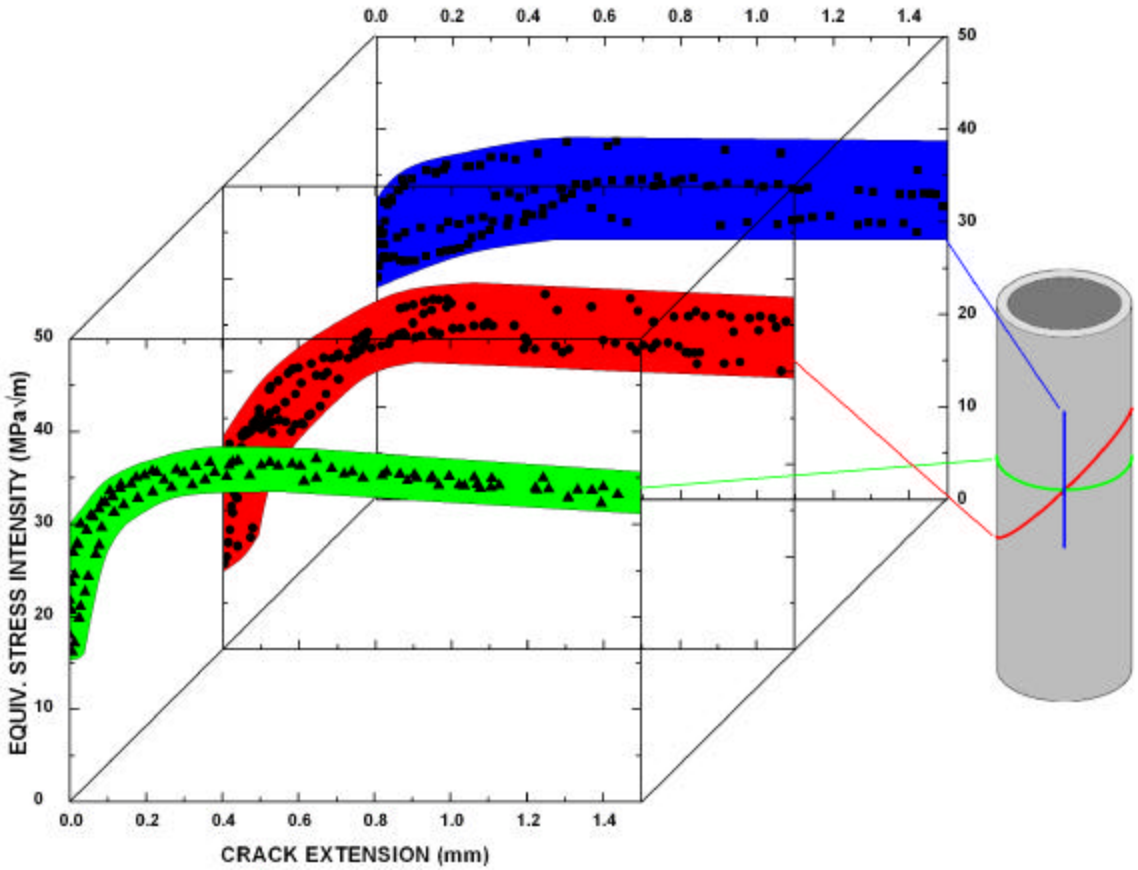

Figure 4.1: Fracture toughness properties of flattened Nitinol thin-walled tubing (longitudinal, 45 deg and circumferential orientations) in 37°C air, in the form of crack-resistance curves (R-curves), show a dependence on both crack-growth direction and the extension Δa of a non-stationary crack; n = 4 per orientation. Initial pre-notch orientations are given on the tube schematic to the right. Crack-initiation toughness values, i.e., the value of the stress intensity at Δa? 0, range from K_o ~ 10 to 27 MPa√m; with crack advance, toughness values approach a steady-state fracture toughness of K_{ss}, ~ 34 MPa√m after ~0.4 mm crack extension.

Scanning electron microscopy of the fracture toughness specimens revealed a ductile fracture with slight evidence of microvoid coalescence (Fig. 4.2). No differences in fracture morphology were detected between the three sample configurations, or between the initiation and steady-state regions.

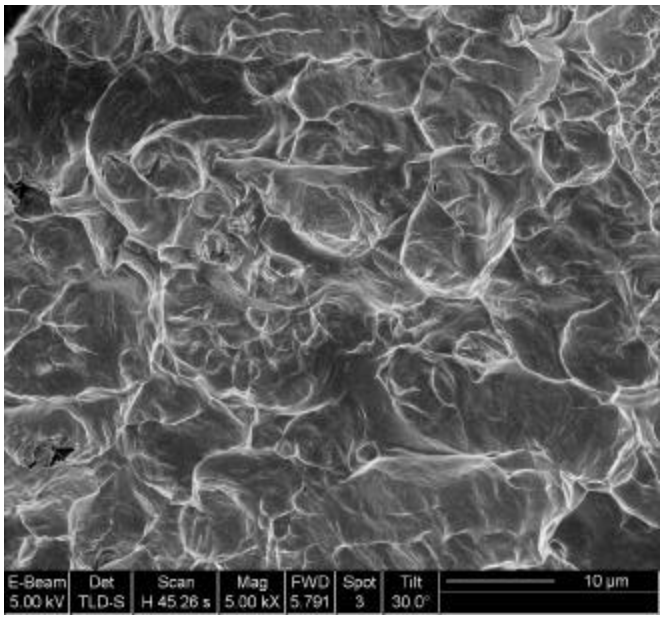

Figure 4.2: Scanning electron micrograph of the overload fracture morphology, corresponding to the steady-state plateau on the R-curve (K_{eq} ~ 34 MPa$\sqrt{m}$), in a circumferentially-oriented pre-notch specimen, showing ductile fracture. No difference in fractography was observed between the initiation and steady-state regions, nor between the three pre-notch orientations (longitudinal, 45 deg, and circumferential).

4.4 Comparison of Fracture Toughness with other Nitinol Product Forms

Very little research into the fracture toughness is reported in the literature (Table 4.1). Indeed, there are only three citations in the literature addressing this critical engineering parameter. Moreover, all of that data appears to be derived from non-standard fracture toughness tests. For example, one study concluded the fracture toughness from a tensile bar with a machined blunt notch [54], another determined the fracture toughness from the unstable growth phase of a fatigue-crack growth curve [48], and the remaining manuscript [21] reported values from specimens that were in non-plane-strain conditions. Certainly there are no reports of the critical engineering design parameter, K_{Ic}, but instead the reports of fracture toughness pertain to very specific product forms and crack criterion and may be crack size and geometry dependent, but in some cases may be far more appropriate than the plane strain (mode I) fracture toughness.

Table 4.1: Summary of material properties, specimen descriptions and fracture toughness values reported in the literature.

Ref	Temperatures, °C					at% Ni	Prod. Form	Dimen., mm		*K*, MPa√m
	M_f	M_s	A_s	A_f	Test			*b*	X*	
[21]	70	80	100	120	30-150	49.9	Plate	12.7	50.8	40-65
[48]	35	49	66	76	20	49.4	HIP bar	10	50	27-32
[54]	-	-	<20	-	20	49.9	-	0.5**	3**	39
Current Work	-	-	-	25	37	50.8	Tube	0.4	12	10-35

* Global size of the specimen; either diameter for disk specimens, or side length for square specimens
** A non-standard specimen was used with gage dimensions 0.5 x 3 mm, and gage length 20 mm

Steady state fracture toughness values (~35 MPa√m) measured herein compare quite well with the other literature citations. However, the current work clearly is the only one that demonstrates an R-curve behavior in Nitinol, and has demonstrated the lowest (initiation) fracture toughness ever reported.

Holtz *et al.* [21] conduct tests over a variety of temperatures such that the toughness as a function of stable microstructural phase was determined. Below the M_s temperature, i.e. where martensite is the stable phase such that there is no superelasticity or phase transformation, the fracture toughness was lowest at ~40 MPa√m. A dramatic increase in fracture toughness, 53 MPa√m, was measured when the specimens were raised in temperature to between the A_s and A_f (100 – 120°C) such that austenite and martensite coexisted and the phase transformation could presumably proceed. Further increase in the toughness, 65 MPa√m, was observed when the material was in the superelastic austenite form (150°C, which is 30°C above A_f) where the transformation to martensite could occur in response to the stresses ahead of the crack tip.

While studying the role of carbide inclusions (TiC) on the fatigue-crack growth properties in hot-isostatic-pressed bar Nitinol (in the stable martensite, non-transforming, phase), Vaidyanathan *et al.* [48] deduced a fracture toughness of 27 MPa√m from the

unstable growth portion of the fatigue-crack growth curve. Interestingly, although the fatigue-crack growth behavior was affected significantly by the presence of TiC inclusions, the fracture toughness values were similar regardless of inclusion density (0-20% inclusion volume content), and ranged from 27-32 MPa√m. Although it is recognized that the unstable growth regime of a fatigue-crack growth curve is dominated by K_{max} approaching the fracture toughness, determination of the fracture toughness from such data cannot account for the role of cyclic deformation, crack size effects, and loading rate; therefore this determination of fracture toughness is questionable.

He *et al*. [54] studied the role of hydrogen embrittlement on the fatigue and fracture of Nitinol. It is unknown what product form of Nitinol that these researchers used, but it was clear from the text that the material was superelastic austenite at the test temperature (20°C). These researchers determined a fracture toughness value of 39.2 ± 2.8 MPa√m in the virgin (non-embrittled) form. The fracture toughness logarithmically decay with increased hydrogen content per: $K_I = 78.8 - 9.8 \ln C_t$, where C_t is the total hydrogen concentration (atomic hydrogen + hydrides) measured in wppm. It should be noted that these researchers used a highly non-standard specimen geometry for determining fracture toughness. Specifically, a tensile "dogbone" specimen with gage dimensions 0.5 x 3.0 mm, and gage length 20 mm were used. Although the authors of that text refer to their measured values as (mode I) fracture toughness values, these values are highly questionable[4], and should be considered "notch toughness" values.

[4] Typically, the apparent fracture toughness scales with the square root of the root radius of the stress concentrator [112. Ritchie RO, Horn RN. Further considerations on the inconsistency of toughness evaluation of AISI 4340 steel austenitized at increasing temperatures. Metallurgical and Materials Transactions A 1978;9A:331-341.]. Consequently, as shown in both metallic [112. Ritchie RO, Horn RN. Further considerations on the inconsistency of toughness evaluation of AISI 4340 steel austenitized at increasing temperatures. Metallurgical and Materials Transactions A 1978;9A:331-341.] and biological

4.5 Conclusions

The fracture toughness of Nitinol tube shows R-curve behavior with crack-initiation toughness significantly lower than the peak toughness value at steady-state. Crack-initiation toughness values ranged from 10 – 27 MPavm, with the lowest initiation toughness associated with fracture in the 45-degree direction to the drawing axis. Steady-state fracture toughness values, conversely, were independent of orientation and were approximately constant at ~34 MPavm, which was achieved after roughly 400 μm of crack extension.

As toughness measurements were performed on actual stent starting material, i.e., ~400 μm thick flattened tube, deformation conditions did not constitute plane strain. Consequently, the values presented herein are not plane strain (mode I) fracture toughness K_{Ic} values. Despite this, they are accurate and entirely appropriate for the specific product form (Nitinol tube) that is used for endovascular stent manufacture. However, it should be noted here that when plane-strain conditions are not applicable, toughness values may become crack size and geometry dependent. Whereas the crack size effect is fully accounted for through the measurement of R-curves, care must be exercised in utilizing the present data for all crack configurations as the cited toughness values may be changed somewhat in different geometries [114]. However, as the present study is performed on compact-tension samples, which develop the most highly constrained (Prandtl) field at the crack tip [115], the present toughness values and R-

---

materials [113. Imbeni V, Nalla RK, Bosi C, Kinney JH, Ritchie RO. *In vitro* fracture toughness of human dentin. Journal of Biomedical Materials Research A 2003;66A:1-9.], when the fracture toughness is measured in specimens containing notches, rather than nominally atomically sharp (e.g., fatigue) precracks, the resulting fracture toughness values can be highly inaccurate.

curves can be considered as worst-case, at least for section sizes with sub-millimeter dimensions.

CHAPTER 5: FATIGUE-CRACK GROWTH IN SIMULATED BODY FLUID

5.1 Introduction

Stresses from *in vivo* operation subject stents to cyclic stresses from the systolic/diastolic sinus rhythms of the blood vessels, which can lead to fatigue damage; damage can potentially result in degraded performance or, in the worse-case scenario, complete failure of the device. The majority of prior research on Nitinol fatigue has focused on determining the stress/strain-life (*S-N*) properties of wire and stent-like samples [31, 42-44, 49, 51, 52, 55, 65, 68, 72-74]. Although vital in determining safe-operating mean and alternating stresses and strains in Nitinol devices, such *S-N* properties do not reveal the individual contributions from the crack nucleation and crack growth, which are critical in estimating conservative device lifetimes and determining critical flaw size detection limits. In particular, a fracture-mechanics based (so-called damage-tolerant) characterization of the fatigue behavior, which compliments existing total-life data and life-prediction analyses, is crucial from the perspective of defining the effect (in terms of potential fracture or reduced lives) of pre-existing crack-like defects in the device (see ref. [116] for such an analysis); *S/N* analyses alone can give little indication of such defect-induced fracture risks. However, fatigue-crack propagation data for Nitinol are extremely limited; in fact, there have only been seven previous studies which isolate crack-growth phenomena in this material, and the majority of this work involves Nitinol product forms that are inappropriate for the manufacture of endovascular stents, namely >1 mm thick plate [21, 31, 45], >10 mm diameter bar [20, 48, 53, 56] and 200 μm thin strip [57, 58]. Moreover, virtually all experimental studies on the fatigue of Nitinol have been conducted at frequencies far in excess of physiological loading, and to

date the effect of frequency on fatigue-crack growth remains undefined. Only one study [117] reports fatigue-crack growth in Nitinol tube material suitable for endovascular stents at both low and high frequencies (5 - 50 Hz); however, this experiments still did not address frequencies as low as those seen *in vivo* (~1 Hz), and did not use a simulated body fluid.

Consequently, it is the primary objective of this chapter to provide a comprehensive characterization of the *in vitro* fatigue-crack growth properties (especially at the all important near-threshold growth rates) in thin-walled Nitinol tubing typically used in commercial stent manufacture in simulated physiological environment, in order to realize quantifiable engineering parameters for designing against premature failure from *in vivo* fatigue damage in endovascular self-expanding stents.

5.2 In Vitro Fatigue-Crack Growth Behavior

To simulate the types of fractures/failures that may result from cumulative damage events, e.g., rhythmic heartbeat, at pre-existing flaws, such as surface scratches or inclusions in the material, the *in vitro* fatigue-crack growth behavior of flattened Nitinol tube was measured in 37°C Hanks' Balanced Salt Solution (HBSS). Preliminary results in specimens with the pre-notch oriented in the circumferential direction were quite interesting. Instead of following an energetically-favorable mode I path, the fatigue pre-cracks grew at an angle of ~45°; see Figs. 5.1 and 5.2. These phenomenon, attributed to the strong texture in the material (Chapter 3), warranted the need for C(T) specimens with the notch oriented at 45° to the drawing direction. Testing in specimens with this orientation resulted in pure mode I crack paths.

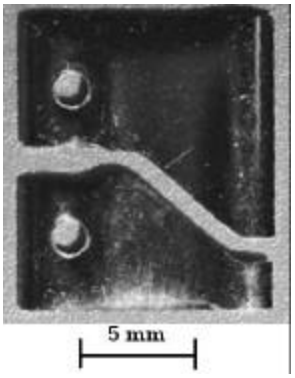

Figure 5.1: A compact-tension C(T) specimen with pre-notch oriented in the circumferential direction and fatigue propagation path deflected ~45 deg to the expected mode I crack path (horizontal in this photograph).

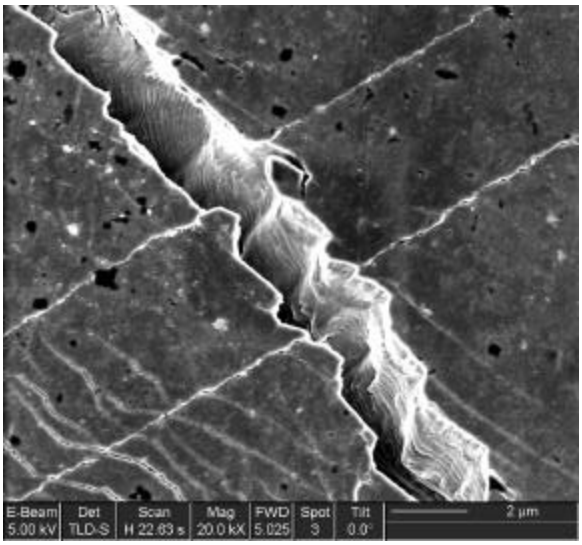

Figure 5.2: Scanning electron micrograph of a kinked fatigue fracture surface showing both the primary crack and secondary microcracks angled from the energetically-favorable mode I crack path, demonstrating the influence of texture on the mechanical properties of Nitinol tube which has its lowest tensile transformational strain in the 45 deg plane (Chapter 3) through which this sample fatigue fractured. The crack-growth direction is diagonal from top-left to bottom-right, with the applied tensile load parallel to the vertical axis (ΔK ~ 6 MPa$\sqrt{m}$, da/dN ~ 10^{-7} m/cycle, R = 0.1).

Figures 5.3 and 5.4 show the results of the fatigue-crack growth tests for positive load ratios of R = 0.1, 0.5 and 0.7, where the stress intensity values were again calculated from handbook solutions [94, 111] per Eqn. 4.1 and 4.2. The variation in crack-growth rates as a function of ΔK for the three load ratios at 50 Hz is shown in Fig. 5.3, where it can be seen that typical of most metallic and intermetallic alloys [118, 119], with an increase in the (positive) load ratio, growth rates are progressively increased, particularly at near-threshold levels. This implies that growth rates depend upon K_{max} as well as ΔK, as can be seen in Fig. 5.4 where the growth rate data of Fig. 5.3 is replotted as a function of K_{max}.

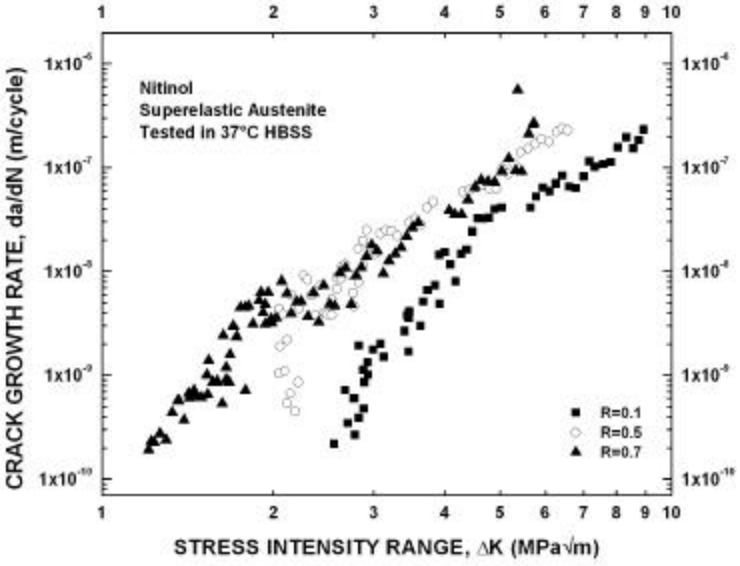

Figure 5.3: Variation in *in vitro* fatigue-crack growth rates (*da/dN*) with the stress-intensity range, ΔK, in 37°C HBSS at 50 Hz test frequency for load ratios of R = 0.1, 0.5, and 0.7, showing the dependencies of the fatigue threshold, ΔK_{th}, and subsequent growth rates on both ΔK and R in Nitinol tube (45° orientation). Fatigue threshold values increase from 1.15 to 2.48 MPavm as the R-ratio decreases from 0.7 to 0.1; n = 4.

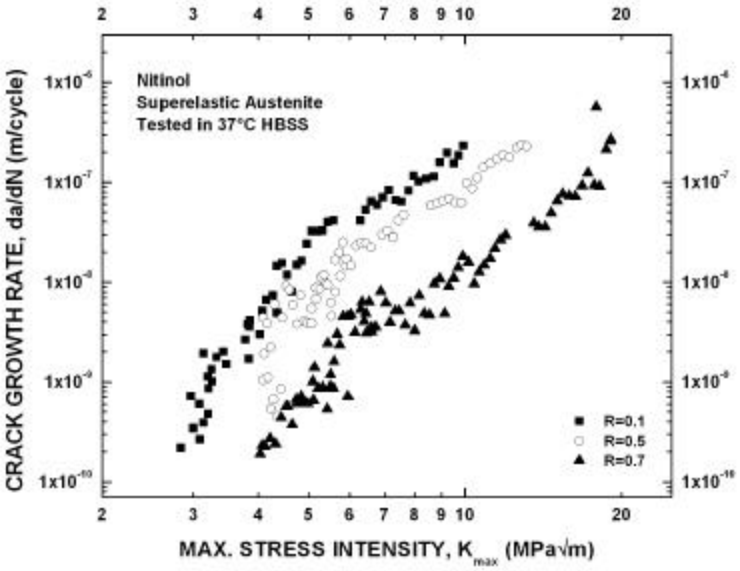

Figure 5.4: *In vitro* fatigue-crack growth data from Fig. 5.4 replotted as a function of K_{max}, still demonstrates a growth-rate dependency on load ratio R, indicating that growth rates in Nitinol tube (45° orientation) have a combined dependence on both ΔK and K_{max}. This combined dependence is quantified as modified Paris-law constants that are presented in Table 1; n = 4 per condition.

5.3 Fatigue Thresholds:

ΔK_{th} fatigue thresholds are progressively decreased at increasing load ratio, specifically by ~53% from 2.48 MPavm at R = 0.1 to 1.15 MPavm at R = 0.7 (Table 5.1). The occurrence of such thresholds is most likely associated with the presence of crack-closure mechanisms, e.g. [118, 119], (Fig. 5.5); their existence is of importance to stents as medical devices operating *in vivo* at stress intensities below ΔK_{th} will not likely experience significant subcritical cracking from surface imperfections or other pre-existing defects in the material. As for the load-ratio dependence of crack-growth rates in Nitinol, an alternative mechanistic explanation to crack dosure is the occurrence of K_{max}-dominated fracture mechanisms ("static modes") [120], that are typically observed in brittle materials. As instability and catastrophic fracture are approached, these mechanisms are often increasingly evident and consequently growth rates become progressively affected by the maximum stress-intensity, rather than simply the stress-intensity range. However, since in the present data, the effect of R is increasingly enhanced at lower growth rates, i.e., as K_{max} approaches the threshold rather than the fracture toughness (Fig. 5.3), the existence of static modes (in addition to striation growth) is unlikely to be prime explanation for load ratio effects in Nitinol. Indeed, there was little evidence of such static modes in scanning electron microscopy images of the fracture surfaces; ductile striation growth was observed at all stress-intensity amplitudes in the higher Paris regime (Fig. 5.6), with the mean striation spacings corresponding well with macroscopic crack-growth rates in the scanned region.

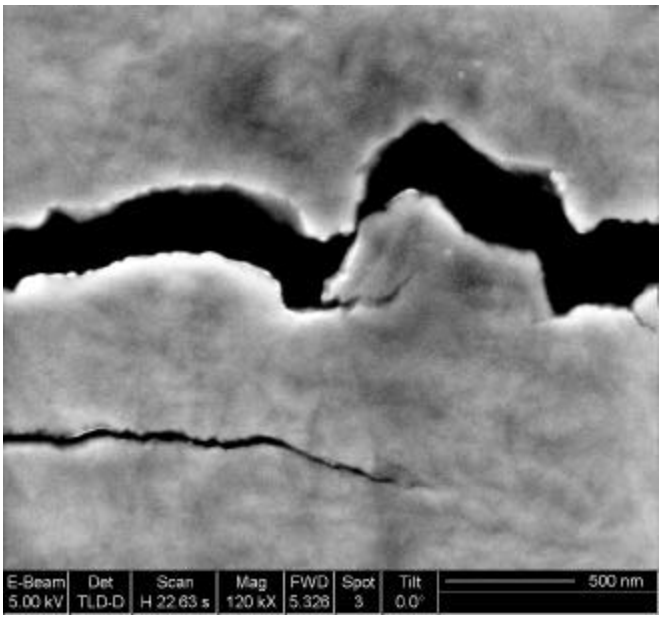

Figure 5.5: Micrograph of near-threshold fatigue crack showing a tortuous crack path following the Nitinol microstructure that creates frictional interference between mating fracture surfaces; this leads to (roughness-induced) crack closure effects that ultimately can lead to arrest of the crack, e.g., at the fatigue threshold. Crack propagation is from left to right, at ΔK = 1.25 MPa$\sqrt{m}$ (R = 0.7).

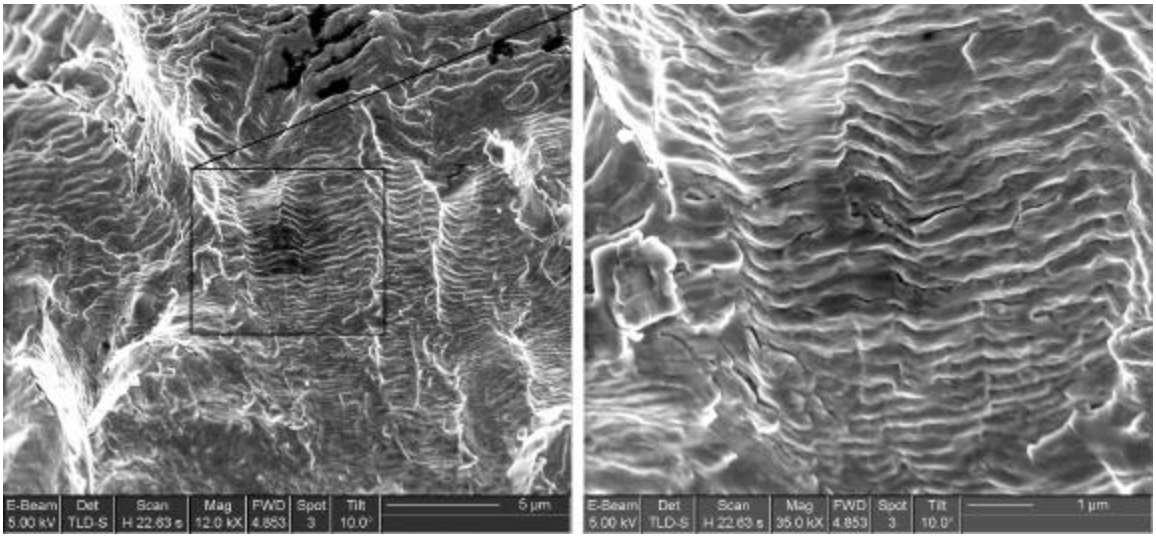

Figure 5.6: Scanning electron micrographs of fatigue striations in the mid-range of growth rates (Paris) regime (R = 0.1, ΔK = 8-9 MPa$\sqrt{m}$, da/dN = 1-2 x 10^{-7} m/cycle). The fatigue striation spacing was ~2-4 x 10^{-7} m/striation, which corresponds well with the measured global crack-growth rates. Macroscopic fatigue crack propagation is left to right in these photo-micrographs; however the striations in this analyzed region (near the C(T) specimen surface) are oriented top to bottom due to the curvature of the crack front near the sample edges.

5.4 Crack-Growth Relationships:

Irrespective of the mechanism of fatigue-crack growth, it is important to reiterate that *in vitro* fatigue-crack growth rates in Nitinol are a function of both ΔK and K_{max}. This can be well described in terms of a modified Paris power-law formulation [119]. Traditionally, "mid-range" fatigue-crack growth data can be fit to Paris-law expressions, which in their simplest connotation are of the form [121]:

$$da/dN = C\,(\Delta K)^m\ , \tag{5.1}$$

where C and m are experimentally determined scaling constants. However, a more complete description for Nitinol can be made using a modified Paris law where growth rates are quantified in terms of both ?K and K_{max} [119]:

$$da/dN = C'(K_{max})^n(\Delta K)^p\ , \tag{5.2}$$

where $C' = C(1\text{-}R)^n$ and $m = n + p$. The traditional and modified Paris-law constants (m, C, n, p, and C') for Nitinol tube are given in Table 5.1 and show a nominally equal dependence on both ?K and K_{max}, although the dependence on K_{max} is higher. This trend is typical for both ductile metals and intermetallics [118, 119], and it is therefore not surprising that Nitinol, which is an intermetallic with a B2 crystal structure in the body-temperature austenite phase, also displays roughly similar dependencies of fatigue-crack growth rates on the maximum and range of the applied stress intensities. Comparisons to crack-growth data collected for Nitinol tube samples tested in air [117] show excellent correlation with the tests conducted in a liquid environment, as indicted by the comparisons in Table 5.1, suggesting that corrosion (at high frequencies) is negligible in this alloy.

Table 5.1: Paris-law fatigue-crack growth constants (defined in Eqs. 5.1 and 5.2) and ΔK_{th} thresholds experimentally determined for flattened Nitinol tube (45° orientation) tested in Hanks' Balanced Saline Solution (HBSS) at 37°C to simulate in vivo conditions. Results are very similar to those collected for the same material tested in air at 37°C [117]. Experimentally determined constants are for fatigue-crack growth at 50 Hz, and show excellent correlation with crack-growth studies performed at typical in vivo frequencies (1 Hz); n = 4 for each condition except the 1 Hz testing where time permitted only n = 1.

R-ratio	Paris constants (37°C-HBSS/air [117])		Modified Paris constants (37°C-HBSS/air [117])			ΔK_{th} (MPa√m)
	m	*C* (m/cycle/(MPa√m)^m)	*n*	*p*	*C'* (m/cycle/(MPa√m)^m)	
0.1	4.43 / 4.21	1.85×10^{-11} / 1.88×10^{-11}	1.87 / 1.53	2.56 / 2.68	1.52×10^{-11} / 1.60×10^{-11}	2.48 / 2.48
0.5	3.81 / 3.43	1.56×10^{-10} / 2.96×10^{-10}	1.25 / 0.75	2.56 / 2.68	6.55×10^{-11} / 1.76×10^{-10}	2.02 / 1.86
0.7	3.62 / 3.71	2.45×10^{-10} / 2.49×10^{-10}	1.06 / 1.03	2.56 / 2.68	6.87×10^{-11} / 7.21×10^{-11}	1.15 / 1.44
0.5 (1 Hz)	3.03	2.79×10^{-10}	-	-	-	-

5.5 Role of Cyclic Frequency:

The vast majority of fatigue data on Nitinol for biomedical devices have been determined at frequencies of 30 Hz or more [20, 42-44, 52, 53, 55-58, 65, 72, 117], primarily for reasons of expediency. Clearly such frequencies do not simulate physiological loading, such as human sinus rhythms, which is unfortunate since in the presence of a "corrosive" environment, fatigue-crack growth rates *per cycle* in most metallic materials are actually accelerated by lower frequencies due to an increased time period for the corrosion kinetics to be active, e.g. [122]. The implications of this are that life predictions may not be conservative when based on such higher frequency fatigue data. Despite this, only one study [117] has addressed the influence of frequency on crack-growth behavior in Nitinol, but that study was in air, not a corrosive medium, and frequencies (5-50 Hz) were still significantly higher than the human heartbeat (1.2 Hz).

To investigate this effect, the present work on the crack-growth rate behavior in HBSS at 50 Hz (Fig. 5.3 and 5.4) was compared with measurements of the corresponding

growth rates at 1 Hz for specific ΔK levels. Results, shown in Fig. 5.7, indicate that at nominal ΔK levels of 2, 3, 4, 5 and 7 MPavm, there is only a minimal difference between crack-growth rates at 1 and 50 Hz. This apparent lack of a corrosion fatigue effect in Nitinol *in vitro* is also evident by the fact that the Paris-law constants from the tests at 50 Hz in HBSS are virtually identical to those determined previously for identical tests in air [117] (Table 5.1). This result is consistent with the studies of Filip *et al*. [57, 58] who concluded that fatigue-crack growth in thin strip Nitinol was not adversely affected by the presence of a simulated body fluid.

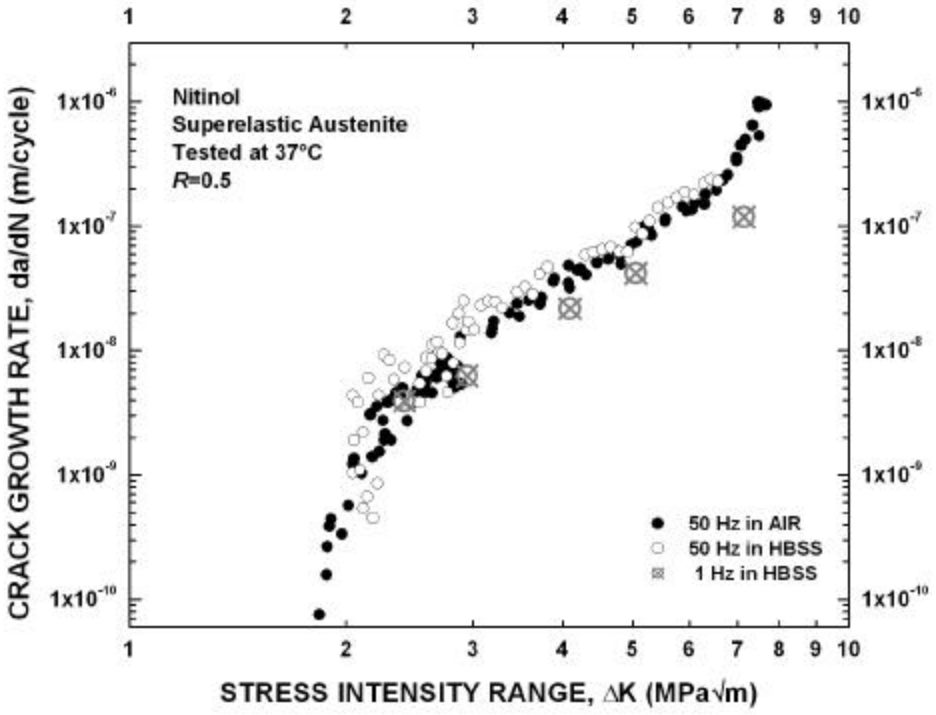

Figure 5.7: Fatigue-crack growth behavior in Nitinol tube (45° orientation) at $R = 0.5$ comparing tests conducted in air at 50 Hz [117], with corresponding results in simulated body fluid (HBSS) at 50 and 1 Hz; n = 4 per condition (except at 1 Hz where n=1). It is apparent that there is no significant difference in fatigue-crack growth data collected in air or in HBSS. Moreover, lower frequencies, which more accurately represent *in vivo* conditions, produce marginally slower growth rates than at higher frequencies, indicating that the higher frequency tests that are invariably utilized may in this case provide slightly more conservative lifetime predictions for Nitinol biomedical devices.

It is interesting to note that in both the current tests and in previously reported experiments in this exact material [117], near-threshold growth rates at the lower frequency are marginally *slower* than at 50 Hz, which implies that the current policy with many stent manufacturers of using high-frequency testing may well provide a conservative basis for predicting *in vivo* device lifetimes. The difference in growth rates at 1 and 50 Hz is small, and could be simply associated with sample-to-sample variations; however, alternative explanations are that more crack-tip corrosion products are able to form at the lower frequency, leading to marginally enhanced (oxide-induced) crack-closure effects [123][5], or possibly that heat, generated adiabatically due to the *in situ* phase transformation in Nitinol, is more effectively dissipated at the lower frequencies in the fluid environment.

Whatever the specific mechanisms, the fatigue data (Fig. 5.7) clearly demonstrates for the first time that coupon or product fatigue testing at frequencies an order of magnitude higher than typical physiological (e.g., human heart beat) frequencies, does not necessarily lead to non-conservative lifetime predictions for Nitinol devices, as *in vitro*

[5] This is actually an unlikely explanation as oxide-induced crack closure effects predominate at lower growth rates at lower ΔK levels [118. Ritchie RO. Mechanisms of fatigue crack propagation in metals, ceramics, and composites: Role of crack-tip shielding. Materials Science & Engineering A 1988;103:15-28.], whereas the present difference in growth rates at 1 and 50 Hz is seen throughout the entire spectrum of growth rates.

fatigue-crack growth rates in superelastic Nitinol tube appear to be essentially frequency-independent in simulated body fluids over the range of 1 to 50 Hz.

5.6 Comparison of Fatigue-Crack Growth Behavior to Prior Work

Previous studies of fatigue-crack growth data in superelastic austenitic Nitinol bar reported threshold ΔK_{th} values of ~1.6 to 2 MPa√m at $R = 0.1$ [20, 53, 56], 2.4 MPa√m in plate [31] at $R<0.1$, ~3 MPa√m in 200 μm thin strips at $R = 0.2$ [57, 58], and 2.48 MPa√m in flattened Nitinol tube in air at $R = 0.1$ [117]. The current test results on flattened Nitinol tube tested in HBSS at $R = 0.1$ give higher threshold values (~2.5 MPa√m) than the bulk Nitinol bar [20, 53, 56], and slightly lower values than the thin strip specimens [57, 58]; results, however, are statistically the same as tests on similar samples tested in 37°C air [117] ($P = 0.53$)[6], see Fig. 5.8. The traditional Paris power-law exponent, m, is slightly greater (~4) in the flattened Nitinol tube investigated in the current study (and ref. [117]), as compared to m values of ~3 in bulk Nitinol bar [20, 53, 56] and thin strip [57, 58]. This observation indicates that crack-growth rates (under constant cyclic loads) increase more rapidly in Nitinol tube than bar or strip, meaning that once a crack reaches steady-state growth in tube, that crack will more rapidly propagate than in other Nitinol product forms. This increased crack growth rate is readily observed when plots of the various product forms are superimposed on each other (Fig. 5.9). Statistical evaluation using grouped linear regression with covariance analysis of the raw data from [20, 31, 53, 56-58], was compared with the current research and showed no significant correlation ($P < 0.001$ at 95% confidence level).

[6] Grouped Linear Regression with Covariance Analysis performed [124. Armitage P, Berry G. Statistical Methods in Medical Research 3rd Ed.: Blackwell Publishing, 1994.], indicating the probability that the two curves are statistically the same is 53% (95% confidence level).

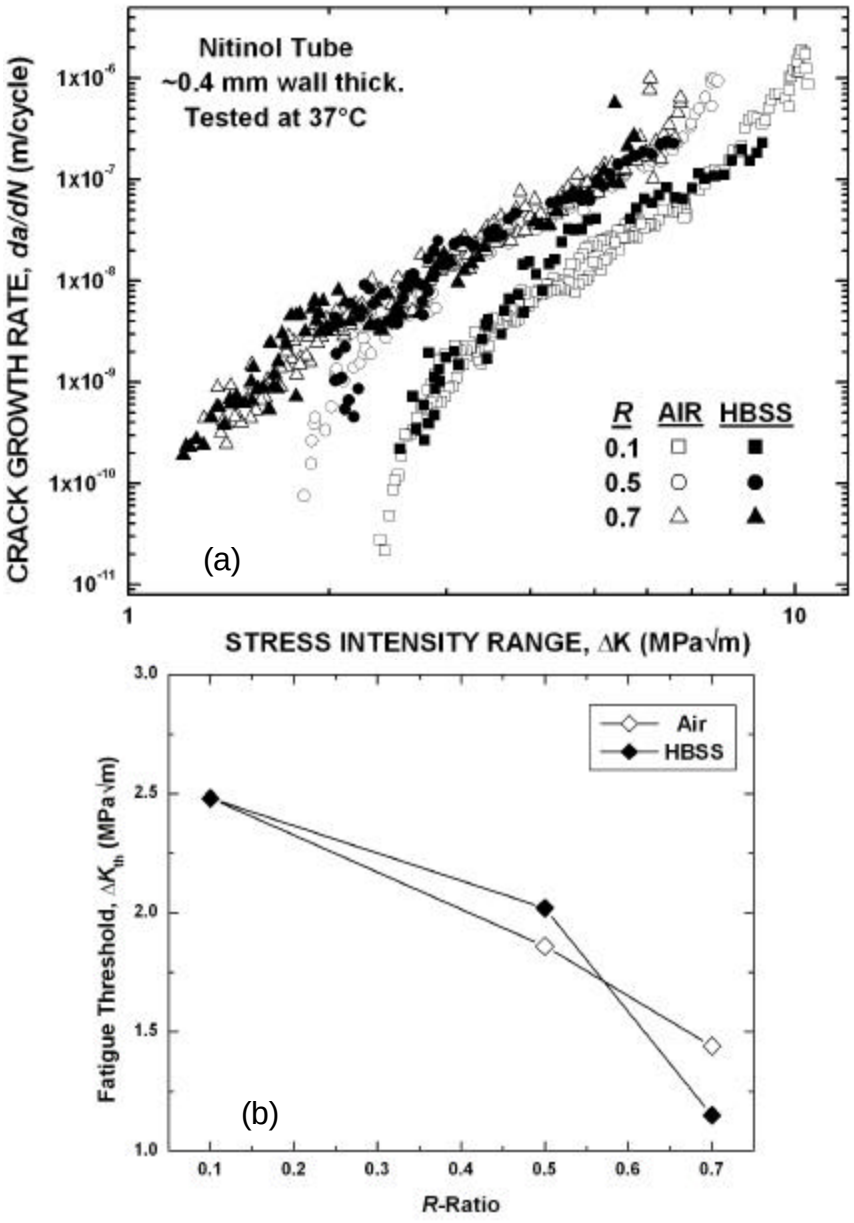

Figure 5.8. Fatigue data from thin-walled superelastic Nitinol tube tested in 37°C air [117] and Hanks' Balanced Saline Solution (HBSS) in the current work showing (a) fatigue-crack growth rates as a function of stress-intensity range ΔK, and (b) the variation in fatigue threshold values with the load ratio (K_{min}/K_{max}), which are virtually identical.

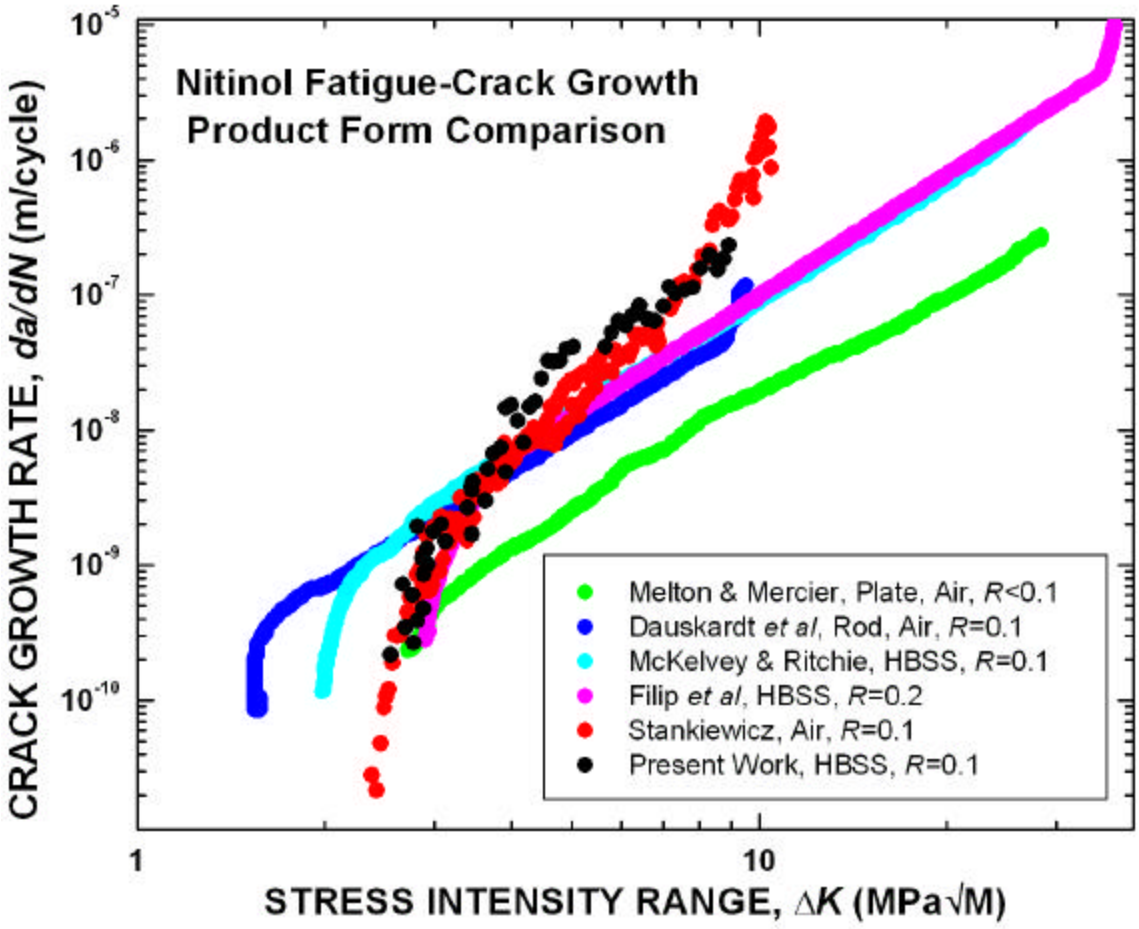

Figure 5.9: Comparison of the current fatigue crack-growth behavior of Nitinol tube tested in HBSS (black circles) at R=0.1 with the same material tested in air (red circles) [117], and all other previously reports of superelastic material: Melton & Mercier [31], Dauskardt *et al*. [20], McKelvey & Ritche [56], and Filip *et al*. [58]. Visually, it is clear that Nitinol tube crack-growth curves are steeper than any previous study in bar, plate and strip. Statistical analysis confirms that visual observation: P-values for the hypothesis that the curves from the present work and [117] are collinear with any of the other data are <0.1%.

5.7 Conclusions

The *in vitro* fatigue-crack growth behavior as a function of load ratio and frequency, has been characterized. This study represents the first report of such fracture mechanics-based evaluation specific to the Nitinol tubing used in the manufacture of many biomedical devices (e.g., stents) in a simulated body solution. The following specific conclusions can be drawn:

1. Fatigue-crack growth behavior in 37°C Hanks' Balanced Saline Solution (HBSS) at 50 Hz frequency was found to display a clear dependence on the load ratio, with increasing growth rates and decreasing fatigue thresholds being measured with increasing positive load ratio from 0.1 to 0.7.

2. Fatigue-crack threshold values, ΔK_{th}, ranged from 1.15 – 2.48 MPavm, with the lowest value being associated with a load ratio of 0.7. Typical of intermetallic materials, crack-growth rates exhibited a similar dependency on ΔK and K_{max}.

3. Fatigue-crack growth rates at 50 Hz frequency were found to be virtually identical in 37°C air as in 37°C HBSS, indicating that at this test frequency corrosion fatigue effects in this alloy in simulated body fluids are minimal.

4. Fatigue-crack growth rates in 37°C HBSS are essentially identical at 1 and 50 Hz, indicating that the fatigue parameters quantified from 50 Hz testing represent a reasonable estimate of the crack-growth behavior at physiological loading frequencies.

CHAPTER 6: X-RAY MICRODIFFRACTION CHARACTERIZATION AT A GROWING FATIGUE CRACK

6.1 Introduction

Previous studies [20, 21, 31, 45, 48, 53, 56-58, 117] have characterized the fatigue resistance of Nitinol, but none have focused on understanding, *at the micron-scale and below*, how cracks propagate in the presence of an *in situ* phase transformation. To start to address this problem, a technique was developed that combines micro-mechanical loading of fracture-mechanics specimens with *in situ* high-resolution imaging with x-ray micro-diffraction (at Beamline 7.3.3 at the Advanced Light Source synchrotron radiation facility, Berkeley, CA). To make these results realistic as possible in terms of modeling stent behavior, the same 400–μm thick thin-walled Nitinol tubing used in Chapters 4 and 5 were employed here (Fig. 6.1) with the exception that the specimens were annealed to produce an average grain size of ~25 μm.

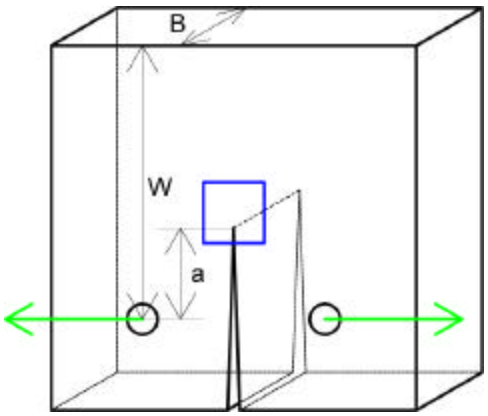

Figure 6.1: Schematic illustration of the compact-tension specimen and region of imaging. The blue box represents the approximate area surrounding the crack tip that was scanned by x-ray micro-diffraction; this region ranged in size from 0.1 x 0.1 to 1 x 1 mm^2, with many thousands of Laue diffraction patterns collected within that box. Specimen dimensions were crack size $a \sim 5.4$ mm, thickness $B \sim 0.4$ mm, and width $W \sim 10.8$ mm. Green arrows denote the direction and location of applied load, which ranged from 0 to 62 N, corresponding to stress-intensity values up to 15 MPa$\sqrt{m}$.

The micro-diffractometer was used to obtain Laue diffraction patterns from very highly localized regions (spot size <1 μm diameter) in the vicinity of the crack tip. By comparing Laue patterns taken in unstrained material, the local strains and grain orientations could be computed [125] at the growing crack tip by analyzing the deviations in the spot locations in diffraction patterns collected near the highly-strained tip region. Each contour plot presented represents data obtained from the analysis of literally thousands of such Laue patterns collected in a grid pattern around the crack tip, involving hundreds of hours of diffraction pattern collection and computational analysis.

Attention was focused on understanding the specific nature of the complex phase transformation ahead of a growing crack tip in Nitinol, as the exact size and shape of the transformation zone has never been characterized at this resolution in a superelastic material. Whereas synchrotron radiation sources have been used to map strains and phases in Nitinol specimens to the same, or lesser, resolution [126-129], the only studies centered on the materials with a phase transformation ahead of a crack trip have been performed at much coarser scales, by optical microscopy and Moiré interferometry [130, 131]. In the present work, x-ray micro-diffraction permits a resolution of ~1 μm resolution, with the Laue diffraction patterns providing a direct measure of the atomic response to applied mechanical forces in this highly unique material.

6.2 Strains Ahead of a Crack Tip

A large region (~1 mm^2) was investigated surrounding a crack tip with diffraction collection points spaced on a 16 x 16 μm grid which provided a coarse view of the microscopic strains (Fig. 6.2). Loads were applied in a sequence such that the sample experienced a stress intensity of 7.5 MPa√m (just below the crack-initiation fracture

toughness of 10 MPa√m, per Chapter 4), followed by continued loading to 15 MPa√m (close to the onset of catastrophic fracture), and finally reverse loading back to 7.5 MPa√m. The strains presented in Fig. 6.2 are on the scale of ±1.25%, which represents a median value of the anisotropic strain required to induce the austenite-to-martensite phase transformation.

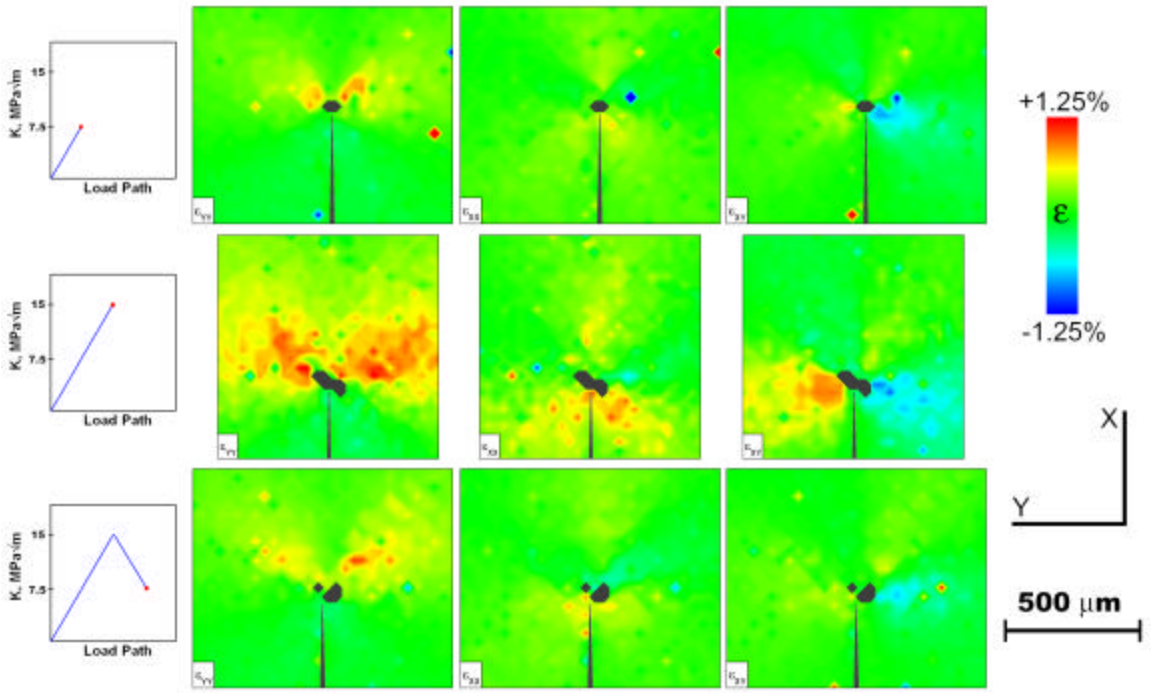

Figure 6.2: Coarse scale (~1 mm^2; 16 x 16 μm step size) elastic strain and resulting phase maps. The top row shows the resultant strains (ε_{yy}, ε_{xx}, ε_{xy}) and regions of transformed martensite surrounding a crack loaded from 0 to 7.5 MPa√m, with the gray regions representing the crack and the phase-transformed material as determined by an absence of Laue diffraction spots. The second row of contour maps shows a dramatic increase in strains and volume fraction of martensite after the crack was further loaded to a stress intensity of 15 MPa√m. Finally, the sample was unloaded to back to 7.5 MPa√m where it is apparent that both the residual tensile strains parallel to the crack face (ε_{yy}) and the martensite volume fraction are much larger than during the first cycle of loading.

As expected, the largest normal strains occur in the plane of the crack surface in the direction of applied loading (the *Y* direction). Loading to the maximum stress intensity (15 MPa√m) resulted in a dramatic increase in the size and extent of the strains around

the crack tip. Reverse loading back to 7.5 MPa√m naturally result in their decrease, although the magnitude of the strains after unloading are much larger than after initial loading to the same stress intensity; this is indicative that cycles of loading can impart residual strains in the vicinity of the crack tip. Although this is well known for the cyclic loading of fatigue cracks in metals, where dislocation plasticity can leave a zone of compressive strain directly ahead of he crack tip (the cyclic plastic zone), it is uncertain whether similar notions apply to a superelastic metal where deformation is occurring via a totally different mechanism, i.e., via a phase transformation.

6.3 Transformation Zone Size and Shape

As deformation resulting from the phase transformation in Nitinol is highly anisotropic, due primarily to crystallographic effects, e.g., texture [95], isotropic plasticity/yield models, such as Tresca or von Mises, are unlikely to have much application to Nitinol. Lexcellent and Blanc [132], however, have proposed a yield model that does account for Nitinol's anisotropy based upon plateau stress variations in tension (370 MPa), compression (515 MPa), and mixed mode derived from experimental tension and bending tests conducted in Nitinol tube. Their yield criterion was applied to the prediction of a partially transformed zone ahead of the crack tip in the C(T) specimens, utilizing standard fracture-mechanics handbook solutions for the angular-dependent stresses around a crack tip [114][7]; results are shown in Fig. 6.3 where stresses

[7] Computer software was written (Appendix A) to calculate the principal stresses in response to an applied stress intensity, K, as a function of angle, q, and distance, r, from the crack tip per the standard fracture mechanics relationship: $s_{1,2} = \frac{K}{\sqrt{2pr}}\cos\left(\frac{q}{2}\right)\left(1 \pm \sin\left(\frac{q}{2}\right)\right)$[114. Anderson TL. Fracture Mechanics: Fundamentals and Applications. 3rd ed. Boco Raton, FL: CRC Press, 2004.]. Unlike conventional fracture mechanics estimations (e.g. Tresca or von Mises) which compare these principal stresses to the yield stress to determine a plastic zone size, these principal stresses here were compared to the anisotropic

within the boundary exceed the anisotropic transformational stresses as described by Lexcellent and Blanc [132]. Perhaps, the most striking feature of the predicted zones (Fig. 6.3) is their "peanut" shape (with less transformation directly ahead of the crack); this is actually characteristic of isotropic, plane-strain conditions, although the sampled regions in this work are clearly in plane stress, due to the limited penetration (of a few micrometers) of the x-rays below the surface. Because the experimentally measured zones also display this peanut (Fig. 6.3), the importance of using an anisotropic yield model for Nitinol is confirmed. However, the measured size of the transformed zones (deduced in Fig. 6.2 from the strain maps and shown in gray) are approximately six times smaller than those predicted by the simple fracture-mechanics solutions.

This apparent contradiction, between observed and predicted zone sizes, appears to result from the fact that the experimentally-determined transformed zones in Fig. 6.2 represent only the material that has *fully* transformed to martensite, whereas the fracture-mechanics predictions are based on a stress to initiate, but not necessarily complete, the transformation. What is difficult here is that complete transformation in Nitinol does not occur at a finite strain or stress level [8]; instead, due to textural effects, the strains for complete transformation range from <1% to as much as 4-5%, with the corresponding stresses ranging from 350 to 800 MPa [133]. Furthermore, x-ray micro-diffraction of a grain that is only partially transformed (i.e., containing both austenite and martensite phases) will necessarily produce Laue diffraction spots from the austenite, but the spots in those patterns will widen due to the scattering effects of the martensite. Only regions

---

transformation stresses (defined at the beginning of the "plateau" in a Nitinol stress/strain diagram) per Lexcellent and Blanc's [132. Lexcellent C, Blanc P. Phase transformation yield surface determination for some shape memory alloys. Acta Materialia 2004;52(8):2317-2324.] yield criterion to derive a boundary that defines a region containing stresses sufficient to drive the phase transformation.

of full transformation (i.e., with no austenite) result in no Laue diffraction spots, which is the method by the transformed regions were determined that are shown as gray regions in Fig. 6.2.

To further investigate the nature of these partially vs. fully transformed zones, three different approaches were taken to estimating partially transformed grains. Each approach assumes complete transformation determined by a lack of Laue diffraction pattern, with partial transformation estimates described in each criterion below.

Criterion 1: partial transformation based upon peak broadening. This approach utilized the fact that the nanoscale lath microstructure of martensite acts as a scattering center, which causes peak widening of the Laue diffraction spots when both phases are present. Most (>90%) of the average peak-width values fell within a very tight range. To determine boundaries representing partial transformation, the lower bound (representing 0% martensite) was set equal to 1.4 times the pixel width at the lower end of the range, and the upper bound (representing 100% martensite) set equal to 4 times that lower pixel width. The calculated zone using this criterion is presented in Fig. 6.3a, and shows that the partial transformation zone is very small, extending only ~50 μm beyond the fully transformed zone, which is much smaller than predicted by the fracture mechanics solutions. Although this is the most direct measure from the Laue diffraction data of phases present, the imposed boundaries are somewhat arbitrary as they were selected based upon visual inspection of individual diffraction patterns to estimate the presence of the martensite.

Criterion 2: partial transformation based upon the equivalent stress > the tensile stress at the onset of transformation (i.e. the plateau stress in a Nitinol stress/strain

diagram)[8]. From laboratory experiments [133], it was found that the onset of the "plateau" tensile stress ranged from 350-550 MPa, and the end of the "plateau" was between 400 and 800 MPa, depending on the loading direction. Therefore the lower bound of partial transformation (0% martensite) was set coincident with the lower-most transformational stress (350 MPa) and upper bound of transformation (100% martensite) with the uppermost transformation stress (800 MPa). This criterion produced a region of partial transformation that coincided quite well in both dimension and shape with the fracture-mechanics predicted solution, as shown in Fig. 6.3b.

Criterion 3: partial transformation based upon the individual stress components, σ_{ij}, > the tensile stress required for transformation in each specific direction. The third criterion was similar to the second in the fact that it imposed stress-based boundaries; however, it utilized knowledge of variations in the transformational stresses [133] as a result of texture orientations within the sample. For the C(T) specimen, the onset of transformation in both the direction of crack propagation (σ_{11}) and in the direction of applied load (σ_{22}) was 350 MPa, with transformation complete at 400 MPa. In the direction 45° between the crack path and applied loading direction, the stress ($s_{45^\circ} = \sqrt{s_{11}^2 + s_{22}^2}$) for the onset of the transformation is 550 MPa, with complete transformation at 800 MPa. At each scan location, the individual stress components were calculated (per App. B), and boundary conditions set as: a) for σ_{11}, 0 and 100% martensite coincided with 350 and 400 MPa, b) for σ_{22}, the bounds were the same as in (a), and c) for σ_{45°, 0 and 100% martensite coincided with 550 and 800 MPa. At each location the total amount of martensite was set equal to the average of the percent

[8] See Appendix B for the determination of stresses from only the deviatoric strains calculated using the Laue diffraction patterns.

martensite determined by boundary conditions (a) – (c) above. Using these directionality-dependent transformation criteria, the calculated partial transformed zones (Fig. 6.3c) were very similar to those from the equivalent stress criterion (Fig. 6.3b). The slightly larger zone size predicted by this *Criterion 3* is attributed to the fact that the additional strain (and therefore stress) associated with dilation is accounted for, whereas the equivalent stress based *Criterion 2* ignores that strain component.

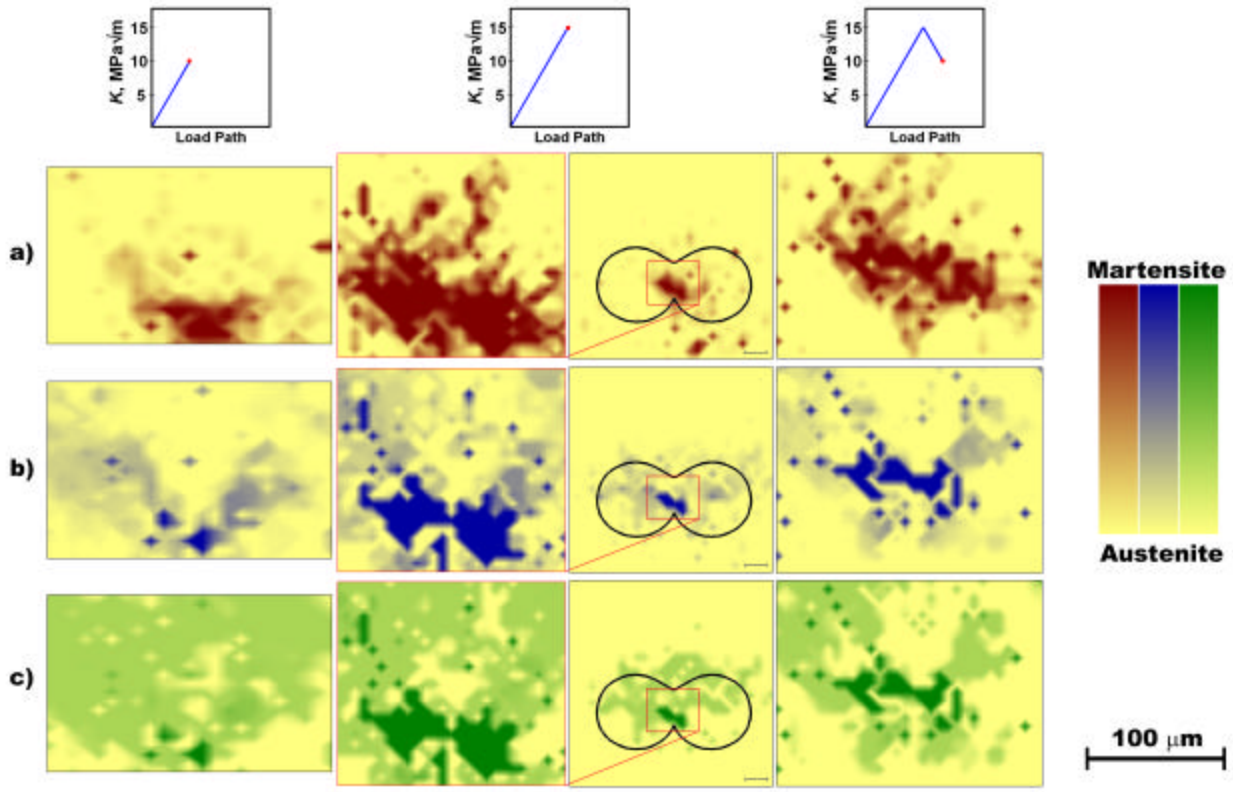

Figure 6.3: Evolution of the transformation zone in response to a single loading and unloading cycle. These fine step-size diffraction maps (3 x 3 μm grid) show the change in size and shape of the transformation zone in response to a loading cycle from 10 to 15 to 10 MPa√m. The black, peanut-shaped boundary in column 3 shows the transformation zone predicted by the combination of simple fracture mechanics solutions [114] with the anisotropic Nitinol yield criterion of Lexcellent and Blanc [132]. The partially transformed material, which comprises a mixture of the austenite and martensite phases, was experimentally-determined using three different criteria: a) *Criterion 1* based upon peak broadening, revealed a much smaller transformed region than was predicted by fracture mechanics; b) *Criterion 2* based on equivalent stresses > tensile transformational stresses, resulted in a zone size and shape in excellent accord with fracture-mechanics

predictions; and c) *Criterion 3* based upon directionality-dependent stresses > tensile transformational stresses, again resulting in good correlation to the anisotropic predictions from fracture mechanics-based solutions but slightly larger than from Criterion 2 because of the inclusion of the dilational strains in this criterion. Note that the scale bar applies to all plots, except the zoomed-out views (column 3) which have a 100 μm scale bar inset.

Although estimated zone sizes from the *Criterion 2* and *3* matched quite well with the fracture-mechanics calculations, neither is entirely appropriate for this particular alloy due to its large grain size. Because multiple diffraction patterns were collected from within each grain, *Criterion 1*, involving peak-widening, is actually more appropriate as it is the only one that directly measures the phase of that grain. The other criteria, however, are appropriate for finer (nanoscale) grained Nitinol (such as those used in the fracture mechanics testing in Chapters 4 and 5) where each diffraction pattern (ring, rather than Laue) would represent the average of many grains in which peak broadening due to individual grain contributions would not be discernable.

The question then arises, why there is such a large discrepancy between the transformation-zone size estimated with the peak-widening criterion and that calculated using fracture mechanics? Although one cannot be certain, it is believed that this is again due to the large grain size, as there are fewer microstructural sites, i.e., grain boundaries, for the nucleation of martensite. Thus, even though the stresses calculated in the second and third criteria are sufficiently high to transform the material out to a zone dimension equivalent to the predicted value, the lack of nucleation cites prevents such widespread transformation.

6.4 Crystallographic Texture Effects on Local Transformation

An interesting observation in the phase maps in Fig. 6.3 is the presence of untransformed "islands" of austenite near the crack tip that are surrounded by transformed material. As these islands are roughly the size of the grains (~25 μm), their presence suggests that the crystallographic alignment of the grains (i.e., the texture) may significantly influence the transformation of material ahead of the growing crack. To investigate this, an *in situ* low-cycle fatigue experiment was performed where a C(T) specimen was cycled between 7.5 and 15 MPa√m (i.e., with $R = 0.5$) for a total of 100 cycles, in order to observe the evolution of the phase transformation throughout the fatigue process. The texture was completely described in three-dimensions for each grain by two planes (one parallel to the crack surface and one parallel to the specimen surface) and a direction vector chosen to be coincident with the crack-growth direction. Results are presented in Fig. 6.4.

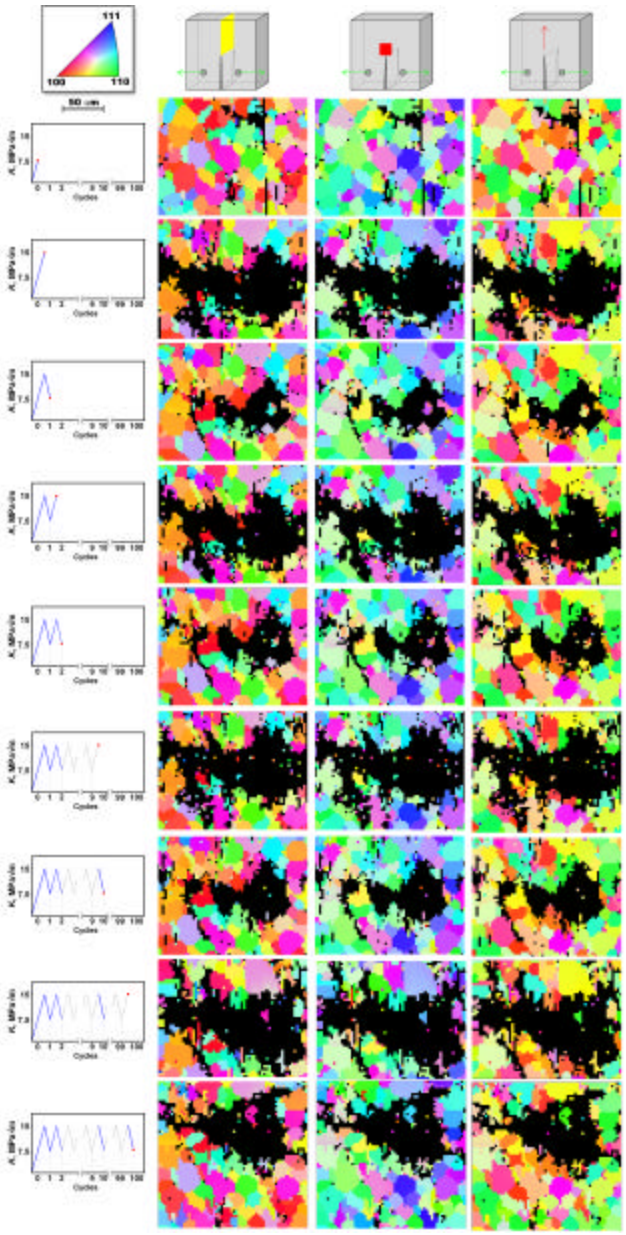

Figure 6.4: Grain-by-grain evolution of the austenite-to-martensite transformation ahead of a crack tip in response to fatigue loading (7.5 to 15 MPa√m) through 100 cycles. The color maps represent Miller index planes or directions of individual austenite grains as indicated above each column, and the black regions are fully transformed martensite. During the first loading cycle to 7.5 MPa√m, the fully transformed zone is <50 μm wide. Subsequent loading to 15 MPa√m and unloading to 7.5 MPa√m results in a growing fully transformed zone size at the 7.5 MPa√m, which stabilizes at ~120 μm between cycle 2 and 10. Conversely, the transformation zone size at the upper stress-intensity level remains constant (~ 200 μm) throughout the fatigue loading cycles. Interestingly, instead of retaining the classic peanut-shaped zone that was seen in earlier experiments, instead several grains have apparently suppressed the phase transformation. These grains are further investigated in Fig. 6.5.

During the first forward cycle to 7.5 MPa√m, the fully transformed zone remained relatively small (~50 μm width) when compared to subsequent cycles (~125 μm), consistent with all previous experiments. This zone size grew substantially, however, after this first cycle, and stabilized in width between the second and tenth cycle. During each fatigue cycle, the crack grew incrementally and then stabilized instantaneously. The diffraction scans were therefore taken while the crack was in a stable configuration. Over the course of the 100 cycles, the crack advanced a total of ~30 μm (da/dN ~ 3 x 10^{-7} m/cycle), which is at the upper end of the Paris regime of fatigue-crack growth for this alloy (see Chapter 5).

Three grains were of special interest. These are highlighted as *A*, *B* and *C* in Fig. 6.5, which shows the grain maps and corresponding crystallographic texture from the C(T) specimen loaded to a stress intensity of 7.5 MPa√m during the second cycle. Although grains *A* and *B* are all well within the phase-transformed region, it is clear that they locally continue to suppress the transformation. In grains *A* and *C*, with crystallographic orientations depicted respectively in Fig. 6.5a and 6.5c, the plane in which the load is applied (the red plane) approximately represents the habit plane (551) [134], i.e., the shared plane between the parent austenite crystal and transformed martensite. One may therefore imagine that loading of that habit plane would promote, rather than inhibit, the phase transformation. However, the transformation from austenite to martensite progresses via a shearing (lattice invariant shear), rather than tensile loading, around that plane [8]. This suggests that the transformation is suppressed in these grains because of a combination of the crystallographic alignment along with the applied loading direction.

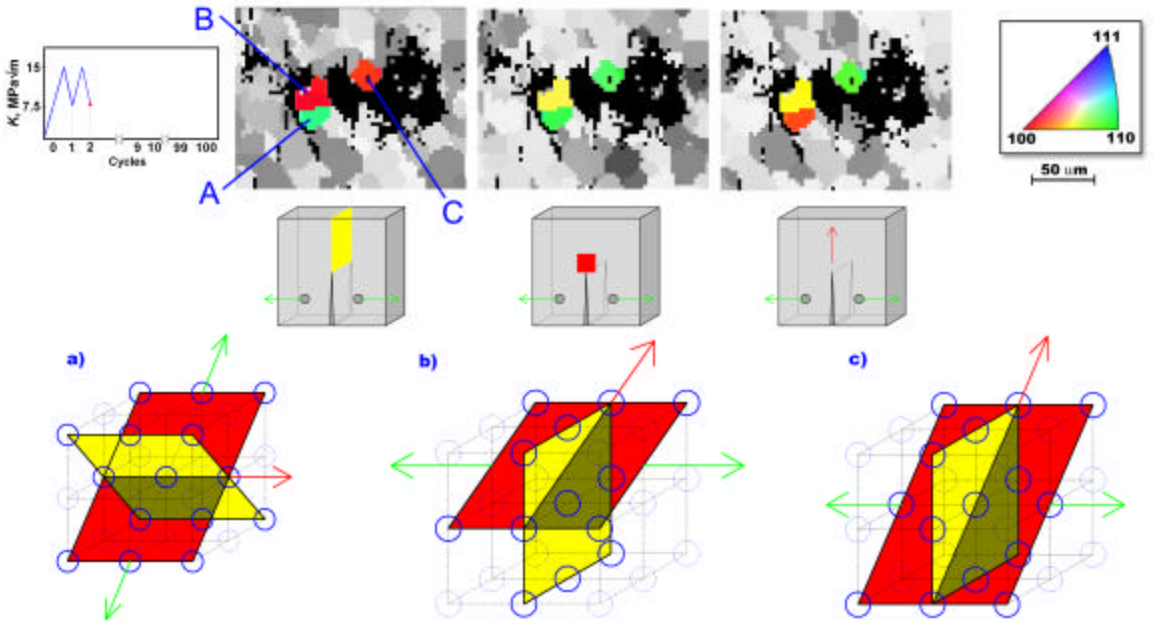

Figure 6.5: Atomistic loading diagram of preferentially untransformed grains shown in Fig. 6.4. The red planes are parallel to the C(T) surface, yellow planes are parallel to the fracture surface, red arrows show the direction of crack growth, and green arrows show the applied loading direction. Note that only the titanium atoms are shown in the diagram for clarity; nickel atoms reside at the [½,½,½] positions. Schematic diagrams of the crystallographic orientations of each grain are given as, a) Grain *A* is oriented with (110) planes parallel to both the C(T) surface (red) and the crack plane (yellow) with growth in the [100] direction; b) Grain *B* shows the lower-most untransformed grain from Fig. 4, with (120) planes parallel to the C(T) surface (red), (100) parallel to the crack plane, and growth in the [120] direction; and c) Grain *C* is immediately ahead of the crack tip, with its (110) plane parallel to the specimen surface, (100) parallel to the crack plane, and [110] in the direction of crack growth.

Grain *C* immediately ahead of the crack tip partially suppressed the transformation during the first ten cycles, and then sometime between the tenth and hundredth cycles transforms and fractures, as indicated by the moving transformation front in Fig. 6.4. It is interesting to note that the orientations of grains *B* and *C* share the same crack plane and applied loading direction, and that grains *A* and *C* share the same loading plane. Clearly grain *C* is subjected to higher strains than the other two grains, due to its proximity to the advancing crack front, yet is still able to suppress the transformation for several cycles while its adjacent grains are transforming preferentially.

These observations of the non-transformation of grains with a preferred orientation not transforming suggest that when the habit plane is loaded predominantly in tension rather than shear (as indicated by the strain maps in Fig. 6.2), the transformation can be suppressed. Furthermore when certain other planes are loaded, e.g., the (120) plane in grain *B* (with crystallographic orientation schematic in Fig. 6.5b), in the [001] direction the transformation may also be suppressed due to elevated stresses required to completely transform to martensite along that loading direction; see discussion below.

These observations of suppressed grain transformation in response to tensile loading along the [100] direction appear to compete with previous theoretical and experimental evidence [108, 109] and Chapter 3 of this text. Those studies concluded that polycrystalline Nitinol loaded in tension along the [100] direction required the least *strain* for complete transformation to martensite when compared to loading upon any other crystallographic direction. In the present research, however, it was shown that two grains, *B* and *C* in Fig. 6.5, that are tensile loaded along that direction suppress the transformation. However, apparent discrepancy can be resolved if the transformation is *stress*, and not *strain*, driven. The results in Refs. [108, 109] and Chapter 3 may indicate a smaller amount of *strain* required, but do not address the *stress* values necessary to reach those strain values. The results presented herein conclusively show that the orientation-dependent transformation ahead of a crack tip with a finite applied load is stress-dominated.

6.5 Conclusions

The role of the austenite to martensite phase transformation, strain state, and texture of Nitinol on crack propagation in a standard fracture-mechanics type compact-tension

specimen has been investigated. Unlike previous studies, the current research was conducted using materials that accurately mimic the manufacturing conditions of biomedical implants, specifically endovascular stents. Furthermore, by utilizing x-ray micro-diffraction techniques, it was possible to obtain a direct measure of strains and crystallographic alignments with a resolution of ~1 μm.

As expected, the strain states surrounding a growing fatigue crack were predominantly tensile in nature. Forward loading to an initial minimum stress intensity always produced a lower strain state and smaller transformation zone than after the specimens experienced a higher stress intensity followed by reverse loading to the minimum value. Stabilization of the zone size at the lower stress intensity occurred between two and ten cycles. Both the fully and partially transformed zones were "peanut-shaped" which was consistent with the fracture-mechanic predictions based *anisotropic* yield surfaces criterion. However, the size of that transformed zone was much smaller than predicted. This discrepancy is attributed to a lack of sufficient nucleation sites in the large grained material which inhibited a large-scale partially-transformed zone ahead of the crack tip. Finally, it was observed that certain crystallographically-oriented grains were able to suppress the phase transformation within the expected fully transformed zone. Grains oriented with the habit plane (551) parallel to the tensile loading direction preferentially suppress the transformation due to a lack of shear across that plane which is required for the phase transformation, and other grains could also suppress the transformation due to the higher stresses required to produce the transformation with orientations near the [100] crystallographic direction.

CHAPTER 7: NITINOL PRODUCT DESIGN USING FRACTURE MECHANICS PARAMETERS

7.1 Introduction

Several key fracture-mechanics parameters associated with the onset of subcritical and critical cracking, specifically the fracture toughness, crack-resistance curve, and fatigue threshold, have been determined in Chapters 4 and 5. These values were obtained for highly specific material: superelastic Nitinol tube that is used for the manufacture of endovascular stents and other biomedical devices. Since the motivation of this work was to determine those critical variables for that very specific engineering application, it warrants a discussion on how to turn those basic materials science parameters into a practical engineering design criterion.

Specifically, these critical materials parameters were used to construct simple decision criteria for assessing the quantitative effect of crack-like defects in such Nitinol devices with respect to their resistance to failure by deformation or fracture. The criteria are based on the (equivalent) crack-initiation fracture toughness and fatigue threshold stress-intensity range presented earlier, together with the general yield strength and fatigue endurance strength from complimentary literature, and are used to construct a basis for design against single-event (overload) failures as well as for time-/cycle-delayed failures associated with fatigue.

7.2 Materials Parameters used for Determination of Safe Operating Conditions

7.2.1 Design against Single-Event Fracture

Fracture toughness values reported for superelastic Nitinol tubing (in Chapter 4) show dependence on both the extent of crack advance, as characterized by the R-curve, and the

orientation of the crack path within the tube. Recall that toughness values for crack initiation are lowest (K_{eq} ~ 10 MPa√m) for cracks growing at 45º to the axis of the tube, and highest (K_{eq} ~ 27 MPa√m) for cracks growing longitudinally, with K_{eq} ~ 16 MPa√m for the circumferential crack-growth orientation. From the perspective of developing conservative design criteria for Nitinol devices, the lower-bound crack-initiation toughness is the parameter of relevance. When local stress intensities are below this value, the device can be considered to be safe from instantaneous overload fracture.

7.2.2 Design against Cumulative Fracture Event

Because of their small-section geometry, combinations of applied stresses and crack sizes leading to stress intensities much above the threshold value can lead to the growth of through-thickness cracks and premature failure of the device. Consequently, for safe *in vivo* operation, it is desirable that stress-intensity conditions remain below the threshold where crack growth is presumed to be dormant.

Conventionally, the fatigue threshold is operationally defined as the stress-intensity range to yield a growth rate less than 10^{-10} m/cycle [94]. However, this rather arbitrary assignment of the threshold, which for physiological frequencies translates to crack extensions of ~4 mm per year, is somewhat precarious when dealing with small devices such as stents which may contain physically-small flaws. Unlike the relatively large cracks, typically millimeters in length, found in laboratory fatigue specimens, biomedical devices are likely to contain far smaller flaws on the order of tens of micrometers in size, *e.g.*, microstructural voids, inclusions or crack-like defects. Thresholds for such small cracks tend to be lower than the large-crack thresholds (this is sometimes referred to as the "small-crack effect" [135]). Although difficult to measure precisely by experiment,

such small-crack thresholds can be usefully estimated by extrapolating the linear, mid growth-rate, portion of the *da/dN* vs. ΔK curve, i.e., the Paris regime, to lower growth rates [121] (as shown schematically in Fig. 7.1). Mechanistically, this can be justified by noting that due to their limiting wake, small cracks do not develop significant levels of crack closure, i.e., microscopic crack wedging processes primarily due to oxide debris or asperity contact inside the crack, which act to effectively lower the near-tip ΔK by increasing K_{min} [118, 123, 136]; such closure tends to prematurely "arrest" cracks leading to asymptotic crack-growth behavior at the large-crack threshold.

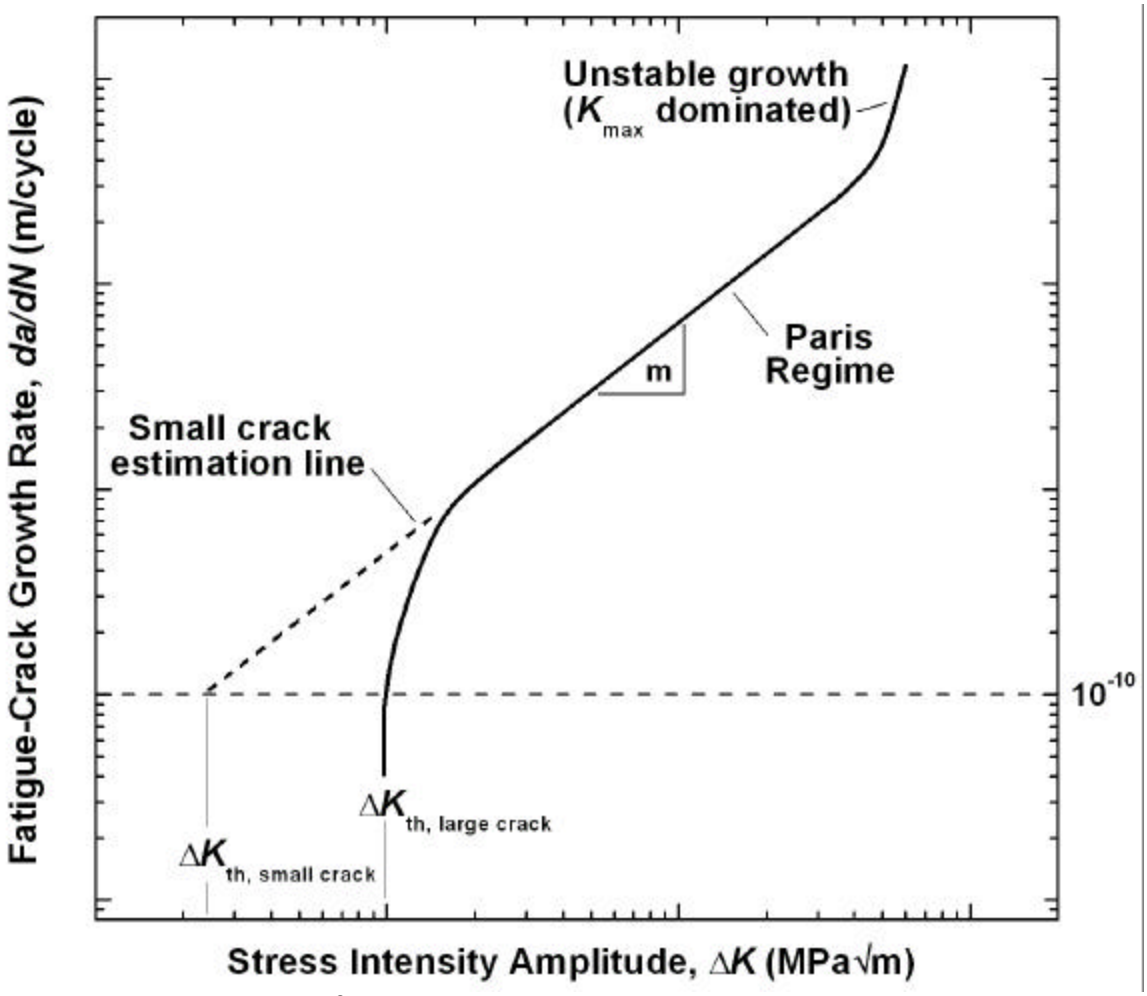

Figure 7.1. A typical fatigue-crack growth-rate curve plotted in log-log scale with critical locations marked. Threshold values, ΔK_{th}, for large cracks are determined from

experimental data collected using standard fracture-mechanics specimens and typically represent the asymptotic stress-intensity range for crack growth. This asymptote of the data in Nitinol tube is invariably due to crack closure effects from interference or wedging of oxidation debris or fracture surface asperities inside the crack flanks. Physically small cracks, however, are more relevant to commercial biomedical devices, and are not subjected to the same closure effects as laboratory-grown large cracks; consequently, they may propagate at stress intensities lower than predicted by large-crack data. Estimates of the threshold stress-intensity range for small cracks can be made by extrapolation of the linear Paris growth-rate curve down to 10^{-10} m/cycle. For small-scale biomedical devices such as endovascular stents that are only a few hundred micrometers thick in specific regions, any stress-intensity ranges above the ΔK_{th} value, *i.e.,* in the Paris or unstable growth regime, can result in rapid through-thickness fracture. Accordingly, the threshold ΔK_{th} value can be considered as the critical limiting variable.

In Chapter 4 it was shown that fatigue-crack growth rates and corresponding threshold values in Nitinol thin-walled tube are sensitive to load ratio but relatively insensitive to test frequency. Small-crack fatigue thresholds can be estimated from the Paris-law constants C and m from Table 5.1, according to:

$$\Delta K_{th,small\ crack} = \left(\frac{10^{-10}}{C} \right)^{1/m} \tag{7.1}$$

The large and small crack threshold values are presented in Table 7.1. Extrapolation of the R = 0.5 data at 1 Hz (Fig. 5.7) resulted in ~9% lower small-crack threshold values when compared to the same data from the higher (unrealistic) 50 Hz frequency test. Therefore, all small-crack ΔK_{th} threshold values estimated from 50 Hz data are reduced by 9% in Table 7.1 to account for the difference between the experimental test frequency and *in vivo* conditions.

Table 7.1: Fatigue-crack growth ΔK_{th} thresholds for thin-walled superelastic Nitinol tube as a function of load ratio, R. Threshold values are shown for both large cracks from experimental results (Chapter 5) and for small cracks based on a linear extrapolation of the Paris regime (Eqn. 7.1). Unless indicated otherwise, the data below was determined from 50 Hz testing.

	DK_{th}, MPaÖm	
R	**Large Crack**	**Small Crack**
0.1	2.48	1.33

0.5	2.02	0.81
0.7	1.15	0.71

7.3 Stress Intensity Factor-Based Device Design Diagram

Mechanical analysis to calculate the stresses experienced by a biomedical device, which is most easily performed by finite-element modeling, can reveal the maximum stress intensities generated at presumed worst-case defects during single-event type occurrences, such as deployment of the stent, and the stress-intensity range (and load ratio) attributed to cyclic deformation, arising from the pulsatile motion of stents in response to the heartbeat (see, for example, ref. [116]). In addition, such analyses can be used to reveal "critical locations" on the biomedical device where cracking problems may arise; these are usually defined as regions of particularly high stress, or where experimental testing or *in vivo* data has shown that cracking events may occur.

By considering the computed stress-intensity values at such critical locations, and comparing them to the critical fracture mechanics parameters of the fracture toughness and fatigue threshold, regions of safe operation can be mapped out in terms of the applied stresses and likely defect sizes. Conservative values here would pertain to the crack-initiation fracture toughness for the appropriate (or worst-case 45º) orientation, and the threshold stress-intensity range for worst-case small cracks at an appropriate (or worst-case highest) load ratio. Figure 7.2 presents such a safe-operating device design diagram based on the fracture mechanics data for Nitinol thin-walled tubing described in this work; this diagram readily permits a quick assessment of the susceptibility of a particular device to failure by time/cycle delayed fatigue or to instantaneous fracture due to an overload. Specifically, the maximum stress intensity produced during single-event type

occurrences is represented by the x-position on the grid, and the stress-intensity range attributed to cyclic events is plotted as the y-coordinate. The location of the (x,y) positional pair on the plot then reveals if the device is susceptible to fatigue-crack growth, overload fracture, or both.

Using worst-case values, Region 1 in Fig. 7.2 represents the area that is safe from fatigue-crack growth and overload fracture under all conditions analyzed (R = 0.1 - 0.7, crack-growth angle = longitudinal, 45°, and circumferential). Regions 2 and 3 represent a degree of susceptibility to fatigue-crack growth and overload fracture, respectively; region 4 represents the unsafe region where the device would be susceptible to both modes of failure. Depending on the individual device mechanics, *e.g.*, if the *in vivo* operating conditions are such that $R < 0.7$, and/or the crack path is nearer the circumferential or longitudinal direction), the safe zone (Region 1) may be expanded to encompass all, or parts of, Regions 2-4. Region 5 represents the worst-case scenario where failure by overload fracture or fatigue-crack growth is an eminent risk.

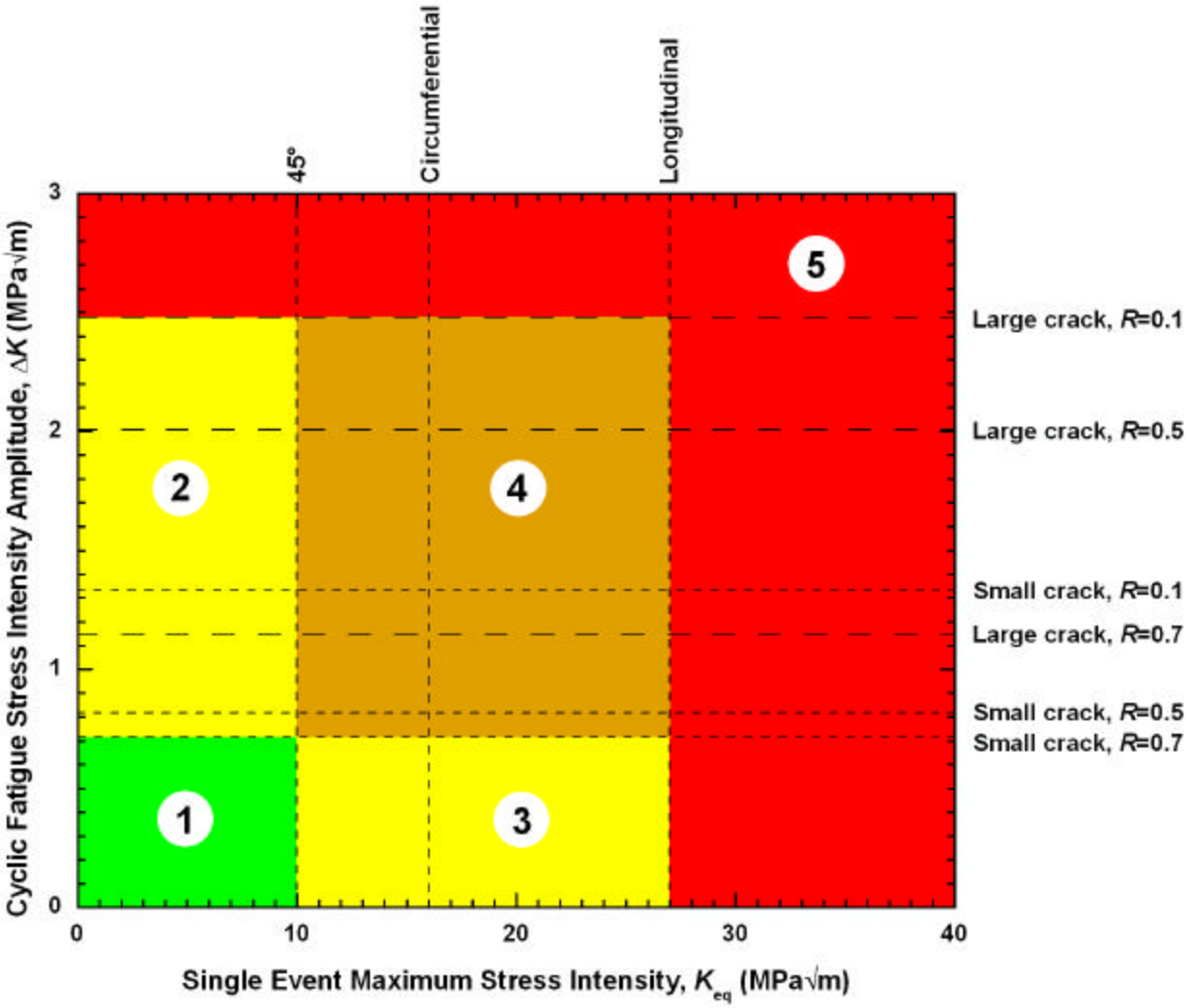

Figure 7.2. A safe-operating device design diagram is shown for devices manufactured from thin-walled superelastic Nitinol tube. Stress intensities attributed to single events, *e.g.*, crimping and deployment stresses in a stent, are represented on the horizontal axis and vary by the angle that the crack is propagating with respect to the tube-drawing direction. Stress-intensity ranges attributed to cyclic events, *e.g.*, contraction and dilation of a stent in response to the heartbeat, are represented on the vertical axis and vary with load ratio, *R*, and whether the experimental large-crack fatigue data or the more conservative small-crack estimates are used. Any combination of defect sizes and single-event stresses and/or cyclic stresses falling into Region 1 pose no threat of fracture or crack propagation under the evaluated conditions. Devices whose stress intensities fall in Regions 2 and 3 are mildly susceptible (depending on exact *R*-ratio and crack-growth directions) to fatigue-crack growth and fracture, respectively; in region 4, the device is susceptible to fracture by either mechanism. Parts that are subjected to any portion of Region 5 are in great risk of fracture either by fatigue or overload, regardless of the crack angle and *R*-ratio.

7.4 Stress and Flaw Size-Based Device Design Diagram

An alternative, and perhaps more insightful, approach to safe design criteria, using applied stresses and flaw sizes (rather than stress-intensity factors as in Fig. 7.2), is afforded by the Kitagawa-Takahashi diagram [137]. For modeling the threshold conditions for fatigue, this approach combines a fracture mechanics-based "damage tolerant" approach, which defines a large-crack limit (in terms of the fatigue threshold ΔK_{th}), with the more traditional "total-life" (*S/N*) approach, which is used to define a small-crack limit in terms of the fatigue limit (or endurance strength) $\Delta\sigma_{fat}$. The benefit of such a combination is that the traditional approach quantifies the effects of crack nucleation and propagation from small, often blunt, flaws that are present in as-manufactured parts, and relates this to the typical data collected from damage-tolerant (*da/dN* vs. ΔK) experiments. The 10^6-cycle endurance strength, $\Delta\sigma_{fat}$, determined for tension-tension fatigue testing in Nitinol tube, varies with heat treatment and *R*-ratio, and ranges from 100-200 MPa [52, 71]. For corresponding modeling of overload failure, the diagram combines the fracture toughness of the material as the large-crack limit and the general yield stress, i.e., limit-load stress for plastic failure, at the small-crack limit. For this particular example, the general yield stress was estimated as simply the uniaxial (0.2% offset) yield stress, from the linear-elastic martensite loading curve, σ_y^{mart}, for Nitinol tubing; this ranges from 1000-1200 MPa [138, 139].

Figure 7.3 shows the constructed Kitagawa-Takahashi diagram for thin-walled superelastic Nitinol tube. The intersection of the damage-tolerant fatigue curves and the endurance strength represents the transition from large to small crack fatigue behavior. In the case of Nitinol tubing, this transition (sometimes referred to as the intrinsic crack

size) occurs at ~15-50 μm. Devices with flaws below this length scale are best analyzed in terms of the endurance strength in fatigue and general yield strength in single-event overloads, whereas fracture mechanics provides the more appropriate means of analysis for flaws larger than this scale, specifically in terms of the fatigue threshold, ΔK_{th}, and fracture toughness, K_{eq}. The steady-state fracture toughness, K_{ss}, is reached following ~400 μm of crack extension, which results in the horizontal transition lines from the longitudinal, circumferential, and 45° crack-initiation toughness-based curves to the steady-state curve at that value of crack size, a.[9] The importance of the Kitagawa-Takahashi diagram for Nitinol is that it provides an alternative design diagram, now presented in terms of applied stresses and flaw sizes, instead of stress-intensity factors, to indicate regions of safe operation (green), risk of failure by time- or cycled-delayed fatigue but not overload failure (yellow), and eminent risk of failure by either fatigue or overload fracture/general yielding.

[9] It should be noted that crack sizes larger than ~100 μm are highly unlikely in biomedical devices with dimensions measured in terms of fractions of millimeters; however, they have been included in the diagram for completeness.

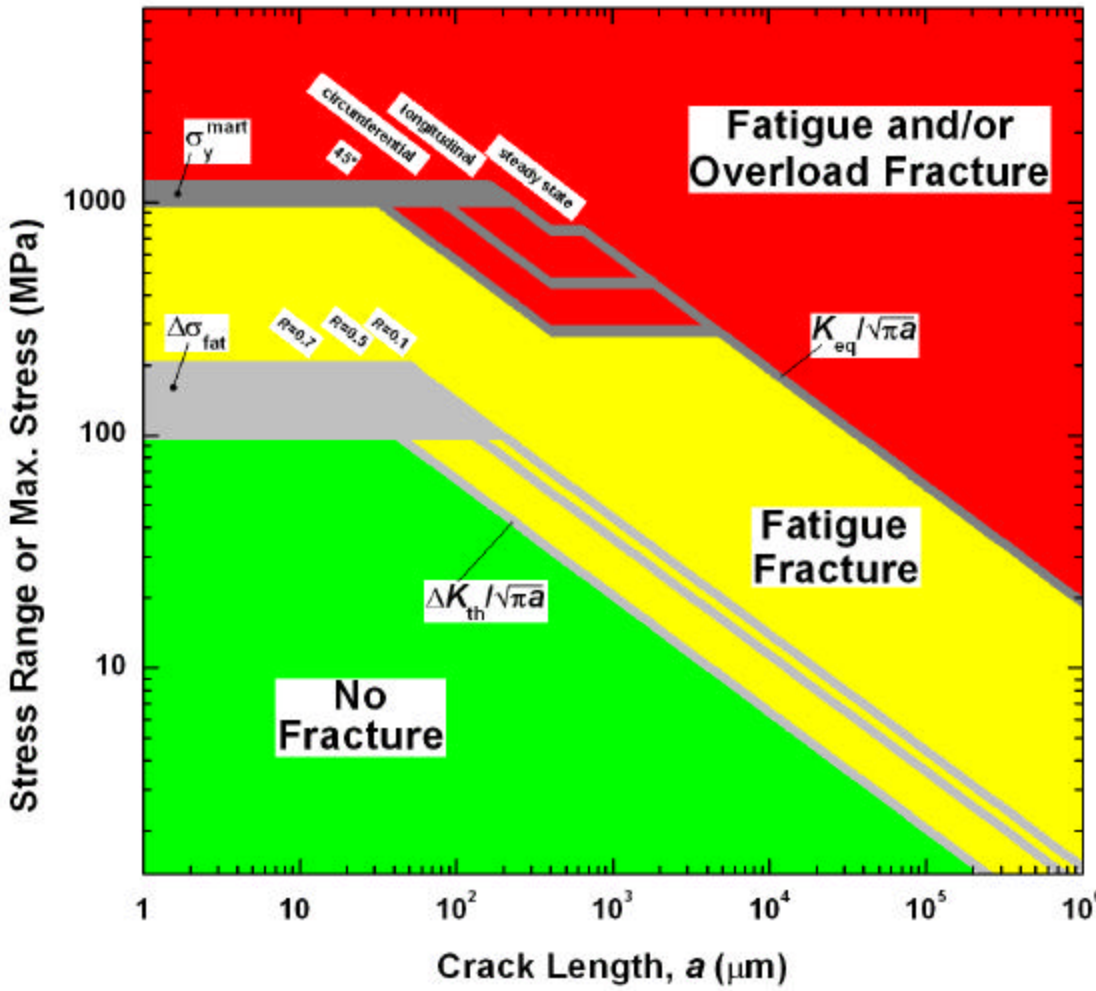

Figure 7.3. Kitagawa-Takahashi diagram [137] for thin-walled superelastic Nitinol tubing showing regions of safe operation (green), risk of failure by fatigue but not overload fracture (yellow), and eminent risk of failure by either fatigue or overload fracture. The transition crack-size between small-crack behavior, governed by the S/N endurance strength (100 – 200 MPa [52, 71]), and large-crack fracture mechanics data, is ~15-50 μm. Above that flaw size, fatigue fracture is best defined by the fracture mechanics-based threshold criterion ΔK_{th}, which is a function of the positive load-ratio, *R*. Failure by overload is bounded by the martensitic yield stress for Nitinol tube (1000 – 1200 MPa [138, 139]) up to a flaw size of ~25 μm, at which point the crack-initiation fracture toughness of the material dominates failure. For crack sizes exceeding ~400 μm, the steady-state fracture toughness value (~34 MPavm) governs the point of fracture, hence the jump from the longitudinal, circumferential and 45° safe operating curves. It should be noted that for the purposes of determining this particular diagram, the geometry factor *Y* was taken as unity and general yield stress defined in uniaxial tension. For an actual device, these would have to be calculated for the specific loading, crack and device geometry.

Note that for the purposes of constructing this generic Kitagawa-Takahashi diagram for superelastic Nitinol thin-walled tubing, the simple fracture mechanics data was plotted, *i.e.*, the fatigue threshold and fracture toughness, in terms of the basic relationship $\Delta\sigma = \Delta K_{th}/Y(\pi a)^{1/2}$ for fatigue conditions, and $\sigma_{max} = K_{eq}/Y(\pi a)^{1/2}$ for overload conditions, with the geometry factor, Y, taken equal to unity. Similarly, the corresponding general yield stress was considered only in terms of simple uniaxial tensile loading. However, computation of the actual variation in these limiting stresses for fatigue and overload failure for specific applications will clearly vary with the crack configuration, the nature of the loading and the particular device geometry.

7.5 Conclusions

A simple fracture mechanics-based approach to design of biomedical devices manufactured from thin-walled (~400 μm thick) superelastic Nitinol tubing has been presented in terms of device design diagrams which depict safe/unsafe operating regions that are dependent upon the levels of maximum and cyclic stresses experienced by the device from handling, implantation and *in vivo* operation. To define cumulative fatigue damage mechanisms attributed to cyclic stresses in a device, *e.g.*, from pulsatile motion of stent in response to the heartbeat, fatigue-crack growth behavior for both large-crack (experimentally determined) and small-crack (a more conservative interpolation of experimental data) threshold values were evaluated to determine the risk of failure by fatigue. To define failure attributed to single overload events, *e.g.*, from deployment stresses in a stent, crack-initiation fracture toughness values were used as the design variable due to the fact that the small dimensions of most biomedical devices restricts them from ever reaching a higher steady-state fracture toughness value. A Kitagawa-

Takahashi diagram combining traditional "total life" fatigue data with fracture mechanics-based failure criteria was also computed to show safe-operating stresses and stress ranges for devices with known flaw dimensions. Such device design diagrams may be considered as a *conservative* means to define the worst-case susceptibility of a biomedical device to premature failure in the presence of defects. What is apparent from such diagrams is that the fracture mechanics-based design parameters compliment, rather than compete, with total-life approaches to fatigue and simple mechanical yield criterion for single-event fracture.

CHAPTER 8: CONCLUDING REMARKS

In this work, it has been proven that the processing that goes into manufacturing the various product forms (bar, sheet, tube) has a profound impact on the crystallographic texture. In turn, that texture dramatically influences the mechanical properties of the material. It was therefore critical to conduct all mechanical testing in product forms that were appropriate for the research application – biomedical devices made from Nitinol tube.

To evaluate the susceptibility of Nitinol biomedical devices to fracture, it was first critical to determine the pertinent engineering parameters (fracture toughness and fatigue-crack growth behavior) in material that accurately mimicked the forms used for devices (tube), while maintaining standard fracture mechanics geometries (compact tension specimens). Testing of these flattened tube specimens revealed a rising R-curve behavior in the fracture toughness. Initiation toughness values ranged from 10 – 27 MPa√m and were highly dependent on the crack orientation within the tube due to textural effects.

The fatigue-crack growth properties were measured and showed an expected ΔK_{th} dependence on the R-ratio, with values ranging from 1.15 MPa√m at R = 0.7 to 2.48 MPa√m at R = 0.1. Interestingly, despite the energetic favorability to grow along a pure mode I path, fatigue cracks always grew along the 45° path (mixed mode I, mode II) relative to the tube drawing axis, presumably due to texture effects. Tests performed on this material in a simulated body fluid produced nearly identical results to those conducted in air, indicating that corrosion has little or no effect at the R-ratios that were evaluated. Lastly, Paris-law exponents, m, were significantly higher than other forms of

Nitinol, indicating a more rapid crack advance rate during steady-state fatigue-crack propagation.

X-ray microdiffraction characterization in a highly localized region around growing cracks in Nitinol expected revealed that strains were mostly tensile in nature. Furthermore, fatigue testing showed that the size of the transformed zone was stable at the maximum stress intensity starting at the first cycle, whereas the zone size upon unloading to the minimum stress intensity did not stabilize until 2-10 cycles. This zone was peanut-shaped and required the use of anisotropic yield models to accurately predict that geometry. However, the experimentally-determined size of that zone was ~5 times smaller than predicted by fracture mechanics solutions, which was attributed to the large grain size that was necessary for these experiments. It is opined that transformation in a nano-crystalline Nitinol material (like those used for biomedical devices) would produce transformation zone matching the fracture mechanics predictions because of the ample nucleation cites (in the form of grain boundaries) that were absent in the material used for this study. Lastly, certain crystallographically-aligned grains were able to suppress the transformation; and comparison of that data with theoretical texture predictions indicated that the transformation should be thought of as stress-, not strain-, driven.

A simple design criterion, in the form of a Kitagawa-Takahashi diagram, was formulated. By combining the fracture toughness with mechanical yield criterion, and fatigue-crack growth data with total-life (*S-N*) data, boundaries of acceptable design were created showing zones of safe operating stress vs. maximum detectible flaw size.

Because this work was specifically aimed at understanding the fracture mechanisms applicable to superelastic Nitinol biomedical devices, it was beyond the scope to

investigate the fracture properties of the non-transforming austenite, and/or the stable martensite phase. Future work could easily determine these properties by simply raising the test temperature above M_d for stable austenite, or below M_s for stable martensite. Fortunately, it was shown in this work that corrosion effects in this material are negligible; therefore testing at elevated or lowered temperatures could be done in air, eliminating the need for specialized low/high temperature fluid systems. Investigation of the fracture properties of each phase may shed light on the individual contributions of each phase in the transforming material. In addition, one could conduct experiments at test temperatures at which the volumetric change during the phase transformation is zero (-8°C for this alloy, as determined by analyzing the data in ref. [22]) to determine the role of the "negative dilation" which will be absent at this temperature.

Current limitations on the ALS beamline prevented the study of the microstructural influences on a growing crack in the true material form that is used for biomedical devices – nano-crystalline Nitinol. However, the micro-diffraction beamline is currently in the process of moving to a higher energy source which will allow for the necessary faster diffraction collection times in monochromatic-mode, and will implement new equipment (namely a computer-controlled goniometer) that will allow future research on the nano-crystalline material. It would be very interesting to repeat exactly the micro-diffraction experiments in such a material to observe if the anisotropic fracture mechanics predictions do accurately match the experimental transformation zone sizes.

Finally, finite element analysis (FEA) using complex material codes may help deconvolute many of the material parameters that cannot be separated via experimentation. For example, after careful matching of the stress-strain and fracture

response to the experimentally-determined data presented herein, one may be able to use FEA simulations to deduce the exact role of the negative dilation, anisotropic transformation stresses/strains, texture, and modulus mismatch between austenite and martensite on the fracture properties of Nitinol tube.

REFERENCES

1. Buehler WJ, Wiley RC, inventors. Nickel-Based Alloys. USA Patent No. 3,147,851, 1965.
2. Espinos JP, Fernandez A, Gonzalez-Elipe AR. Oxidation and diffusion processes in nickel-titanium oxide systems. Surface Science 1993;295(3):402-410.
3. Kujala S, Pajala A, Kallioinen M, Pramila A, Tuukkanen J, Ryhanen J. Biocompatibility and strength properties of nitinol shape memory alloy suture in rabbit tendon. Biomaterials 2004 2004/1;25(2):353-358.
4. Ryhanen J. Biocompatibility of Nitinol. SMST-2000: The International Conference on Shape Memory and Superelastic Technologies; Pacific Grove, CA; USA; 2003 2001:251-259.
5. Yahia LH. Shape Memory Implants. Berlin: Springer, 2000.
6. Duerig T, Pelton A, Stockel D. An overview of nitinol medical applications. Materials Science and Engineering A 1999;273-275:149-160.
7. Duerig TW, Tolomeo DE, Wholey M. An overview of superelastic stent design. Minimally Invasive Therapy & Allied Technologies 2000;9(3/4):235-246.
8. Duerig TW, Melton KN, Stockel D, Wayman CM. Engineering Aspects of Shape Memory Alloys. London: Butterworth-Heinemann Ltd., 1990.
9. Duerig TW. Applications of Shape Memory. Materials Science Forum, in Martensitic Transformations II, (ed) Muddle BC 1990;56-58:679-692.
10. Duerig TW. Present and Future Applications of Shape Memory and Superelastic Materials. Proceedings of the Materials Research Society Symposium 1995;360:497-506.
11. Duerig TW, Melton KN. Applications of Shape Memory in the USA. In: Igata N, Kimpara I, editors. New Materials and Processes for the Future, 1989. p. 195-200.
12. Pelton AR, Stoeckel D, Duerig TW. Medical Uses of Nitinol. Materials Science Forum 2000;327-328:63-70.
13. Michal GM, Sinclair R. The structure of TiNi martensite. Acta Crystallographica B 1981;B37:1803-1806.
14. Tan G, Liu Y. Comparative study of deformation-induced martensite stabilisation via martensite reorientation and stress-induced martensitic transformation in NiTi. Intermetallics 2004 2004/4;12(4):373-381.
15. Tan L, Crone WC. In situ TEM observation of two-step martensitic transformation in aged NiTi shape memory alloy. Scripta Materialia 2004;50(6):819-823.
16. Uchil J, Mahesh KK, Ganesh Kumara K. Calorimetric study of the effect of linear strain on the shape memory properties of Nitinol. Physica B: Condensed Matter 2001;305(1):1-9.
17. Duerig TW. Some unsolved aspects of Nitinol. Materials Science and Engineering: A 2006;In Press, Corrected Proof.
18. Duerig TW, Pelton AR. An Introduction to Nitinol Biomedical Devices. Workshop: Shape Memory and Superelastic Technologies Conference (SMST), Pacific Grove, CA 2003.

19. McNaney JM, Imbeni V, Jung Y, Papadopoulos P, Ritchie RO. An experimental study of the superelastic effect in a shape-memory Nitinol alloy under biaxial loading. Mechanics of Materials 2003;35(10):969-986.
20. Dauskardt RH, Duerig TW, Ritchie RO. Effects of In Situ Phase Transformation on Fatigue-Crack Propagation in Titanium--Nickel Shape-Memory Alloys. Proceedings of the MRS International Meeting on Advanced Materials Vol 9 Shape Memory Materials; Tokyo; Japan; 31 May-3 June 1988 1989:243-249.
21. Holtz RL, Sadananda K, Imam MA. Fatigue thresholds of Ni-Ti alloy near the shape memory transition temperature. International Journal of Fatigue 1999 Nov;21:S137-145.
22. Mehta A, Imbeni V, Ritchie RO, Duerig TW. On the electronic and mechanical instabilities in Ni50.9Ti49.1. Materials Science and Engineering A 2004;378(1-2):130-137.
23. Dauskardt RH, Marshall DB, Ritchie RO. Cyclic Fatigue-Crack Propagation in Mg-PSZ Ceramics. Journal of the American Ceramics Society 1990;73(4):893-903.
24. Evans AG, Cannon RM. Overview no. 48 : Toughening of brittle solids by martensitic transformations. Acta Metallurgica 1986;34(5):761-800.
25. Marshall DB, Shaw MC, Dauskardt RH, Ritchie RO. Crack Tip Transformation Zones in Toughened Zirconia. Journal of the American Ceramics Society 1990;73(9):2659-2666.
26. Simon M, inventor. Blood Clot Filter. USA Patent No. 4,425,908, 1984.
27. Ring ME. How a Dentist's Name Became a Synonym for a Life-Saving Device: The Story of Dr. Charles Stent. Journal of the History of Dentistry 2001 Jul 2001;49(2):77-80.
28. Ratner BD, Hoffman AS, Schoen F, J., Lemons JE, editors. Biomaterials Science: An Introduction to Materials in Medicine. San Diego, CA: Academic Press, 1996.
29. Bonsignore C. A Decade of Evolution in Stent Design. In: Pelton AR, Duerig T, editors. Proceedings of the International Conference on Shape Memory and Superelastic Technologies; 2003; Pacific Grove, CA; 2003. p. 519-528.
30. Stoeckel D. Nitinol Medical Devices and Implants. Minimally Invasive Therapy & Allied Technologies 2000;9(2):81-88.
31. Melton KN, Mercier O. Fatigue of NITI thermoelastic martensites. Acta Metallurgica 1979;27(1):137-144.
32. Miyazaki S, Imai T, Otsuka K, Suzuki Y. Luders-like deformation observed in the transformation pseudoelasticity of a Ti---Ni alloy. Scripta Metallurgica 1981;15(8):853-856.
33. Miyazaki S, Kimura S, Takei F, Miura T, Otsuka K, Suzuki Y. Shape memory effect and pseudoelasticity in a Ti---Ni single crystal. Scripta Metallurgica 1983;17(9):1057-1062.
34. Miyazaki S, Otsuka K, Suzuki Y. Transformation pseudoelasticity and deformation behavior in a Ti-50.6at%Ni alloy. Scripta Metallurgica 1981;15(3):287-292.
35. Miyazaki S, Otsuka K, Wayman CM. The shape memory mechanism associated with the martensitic transformation in Ti-Ni alloys. I. Self-accommodation. Acta Metallurgica 1989;37(7):1873-1884.

36. Stoeckel D, Bonsignore C, Duda S. A survey of stent designs. Minimally Invasive Therapy & Allied Technologies 2002;11(4):137-147.
37. de Azevedo Bahia MG, Fonseca Dias R, Buono VTL. The influence of high amplitude cyclic straining on the behaviour of superelastic NiTi. International Journal of Fatigue 2006 2006/9;28(9):1087-1091.
38. Tripi TR, Bonaccorso A, Condorelli GG. Cyclic fatigue of different nickel-titanium endodontic rotary instruments. Oral Surgery, Oral Medicine, Oral Pathology, Oral Radiology, and Endodontology 2006;In Press, Corrected Proof.
39. Yan XJ, Yang DZ, Liu XP. Influence of heat treatment on the fatigue life of a laser-welded NiTi alloy wire. Materials Characterization 2006;In Press, Uncorrected Proof.
40. Predki W, Klonne M, Knopik A. Cyclic torsional loading of pseudoelastic NiTi shape memory alloys: Damping and fatigue failure. Materials Science and Engineering: A 2006 2006/2/15;417(1-2):182-189.
41. Ullmann CJ, Peters OA. Effect of Cyclic Fatigue on Static Fracture Loads in ProTaper Nickel-Titanium Rotary Instruments. Journal of Endodontics 2005 2005/3;31(3):183-186.
42. Eggeler G, Hornbogen E, Yawny A, Heckmann A, Wagner M. Structural and functional fatigue of NiTi shape memory alloys. Materials Science and Engineering A 2004 2004/7/25;378(1-2):24-33.
43. Wagner M, Sawaguchi T, Kaustrater G, Hoffken D, Eggeler G. Structural fatigue of pseudoelastic NiTi shape memory wires. Materials Science and Engineering A 2004 2004/7/25;378(1-2):105-109.
44. Fife D, Gambarini G, Britto LR. Cyclic fatigue testing of ProTaper NiTi rotary instruments after clinical use. Oral Surgery, Oral Medicine, Oral Pathology, Oral Radiology & Endodontics 2004 2004/2;97(2):251-256.
45. Miyazaki S, Suizu M, Otsuka K, Takashima T. Effect of Various Factors on Fatigue Crack Propagation Rate in Ti--Ni Alloys. Proceedings of the MRS International Meeting on Advanced Materials Vol 9 Shape Memory Materials; Tokyo; Japan; 31 May-3 June 1988 1989:263-268.
46. Kuhn G, Jordan L. Fatigue and Mechanical Properties of Nickel-Titanium Endodontic Instruments. Journal of Endodontics 2002 2002/10;28(10):716-720.
47. Li U-M, Lee B-S, Shih C-T, Lan W-H, Lin C-P. Cyclic Fatigue of Endodontic Nickel Titanium Rotary Instruments: Static and Dynamic Tests. Journal of Endodontics 2002 2002/6;28(6):448-451.
48. Vaidyanathan R, Dunand DC, Ramamurty U. Fatigue crack-growth in shape-memory NiTi and NiTi-TiC composites. Materials Science and Engineering A 2000 2000/9/30;289(1-2):208-216.
49. Tabanli RM, Simha NK, Berg BT. Mean stress effects on fatigue of NiTi. Materials Science and Engineering A 1999 1999/12/15;273-275:644-648.
50. Yan XJ, Yang DZ, Qi M. Rotating-bending fatigue of a laser-welded superelastic NiTi alloy wire. Materials Characterization 2006;57(1):58-63.
51. Harrison W, Lin ZC. The study of Nitinol bending fatigue. SMST-2000: The International Conference on Shape Memory and Superelastic Technologies; Pacific Grove, CA; USA; 30 Apr-4 May 2000 2001:391-396.

52. Pelton AR, Gong XY, Duerig TW. Fatigue Testing of Diamond-Shaped Specimens. SMST-2000: The International Conference on Shape Memory and Superelastic Technologies; Pacific Grove, CA; USA; 2003 2001:293-302.
53. McKelvey AL, Ritchie RO. Fatigue-crack growth behavior in the superelastic and shape-memory alloy Nitinol. Metallurgical and Materials Transactions A (Physical Metallurgy and Materials Science) 2001;32A(3A):731-743.
54. He JY, Gao KW, Su YJ, Qiao LJ, Chu WY. The role of hydride, martensite and atomic hydrogen in hydrogen-induced delayed fracture of TiNi alloy. Materials Science & Engineering A (Structural Materials: Properties, Microstructure and Processing) 2004;A364(1-2):333-338.
55. Prymak O, Klocke A, Kahl-Nieke B, Epple M. Fatigue of orthodontic nickel-titanium (NiTi) wires in different fluids under constant mechanical stress. Materials Science and Engineering A 2004;378(1-2):110-114.
56. McKelvey AL, Ritchie RO. Fatigue-crack propagation in Nitinol, a shape-memory and superelastic endovascular stent material. Journal of Biomedical Materials Research A 1999 Dec;47(3):301-308.
57. Filip P, Paliwal M, Mazanec K. Fatigue crack propagation in pseudoelastic TiNi smart microcomponents. Zeitschrift Fur Metallkunde 2004 May;95(5):356-361.
58. Filip P, Mazanec K. Fatigue behavior of pseudoelastic TiNi thin strips in air and body fluid simulated environments. Kovove Materialy-Metallic Materials 2003;41(5):300-312.
59. Miyazaki S, Sugaya Y, Otsuka K. Effects of Various Factors on Fatigue Life of Ti--Ni Alloys. Proceedings of the MRS International Meeting on Advanced Materials Vol 9 Shape Memory Materials; Tokyo; Japan; 31 May-3 June 1988 1989:251-256.
60. Furuya Y, Shimada H, Matsumoto M, Honma T. Fatigue and Degradation of Shape Memory Effect in Ti--Ni Wire. Proceedings of the MRS International Meeting on Advanced Materials Vol 9 Shape Memory Materials; Tokyo; Japan; 31 May-3 June 1988 1989:269-274.
61. Miyazaki S, Sugaya Y, Otsuka K. Mechanism of Fatigue Crack Nucleation in Ti--Ni Alloys. Proceedings of the MRS International Meeting on Advanced Materials Vol 9 Shape Memory Materials; Tokyo; Japan; 31 May-3 June 1988 1989:257-262.
62. Heckmann A, Hornbogen E. Effects of thermomechanical pre-treatments on pseudo-elastic fatigue of a NiTi alloy. Materials Science Forum (Switzerland) 2003;394-395:325-328.
63. Furuichi Y, Tobushi H, Ikawa T, Matsui R. Influence of strain ratio on bending fatigue life of a TiNi shape memory alloy wire. Nippon Kikai Gakkai Ronbunshu A Hen (Transactions of the Japan Society of Mechanical Engineers Part A)(Japan) 2003 July;15(7):1094-1100.
64. Predki W, Kloenne M, Knopik A. Fatigue Behavior of Superelastic Niti Alloys Subjected to Torsional Loading. SMST-2003: The International Conference on Shape Memory and Superelastic Technologies; Pacific Grove, CA; USA; 5-8 May 2003 2004:285-292.
65. Morgan NB, Painter J, Moffat A. Mean Strain Effects and Microstructural Observations During in vitro Fatigue Testing of NiTi. SMST-2003: The

International Conference on Shape Memory and Superelastic Technologies; Pacific Grove, CA; USA; 5-8 May 2003 2004:303-310.
66. Hornbogen E, Heckmann A. On the Interrelation of Microstructure, Localization of Transformational Strain, and Strain Rate in Pseudo-Elastic Fatigue of Niti. SMST-2003: The International Conference on Shape Memory and Superelastic Technologies; Pacific Grove, CA; USA; 5-8 May 2003 2004:277-283.
67. Furuichi Y, Tobushi H, Ikawa T, Matsui R. Fatigue properties of a TiNi shape-memory alloy wire subjected to bending with various strain ratios. Proceedings of the Institution of Mechanical Engineers L, Journal of Materials: Design and Applications 2003;217(L2):93-99.
68. Tabanli RM, Simha NK, Berg BT. Mean strain effects on the fatigue properties of superelastic NiTi. Metallurgical and Materials Transactions A (USA) 2001 July;32A(7):1866-1869.
69. McNichols JL, Jr., Brookes PC, Cory JS. NiTi Fatigue Behavior. Journal of Applied Physics 1981 Dec.;52(12):7442-7444.
70. Wasilewski RJ. Martensitic Transformation and Fatigue Strength in Tini. Scripta Metallurgica 1971 Mar.;5(3):207-211.
71. Lopes TL, Gong XY, Trepanier C. Fatigue performance of Nitinol tubing with A_f of 25°C. In: Pelton AR, Duerig T, editors. Proceedings of the International Conference on Shape Memory and Superelastic Technologies; 2003; Pacific Grove, CA: SMST; 2003. p. 293-302.
72. Pelton AR, DiCello J, Miyazaki S. Optimization of processing and properties of medical-grade Nitinol wire. SMST-2000: The International Conference on Shape Memory and Superelastic Technologies; Pacific Grove, CA; USA; 30 Apr-4 May 2000 2001:361-374.
73. Tolomeo DE, Davidson S, Santinoranont M. Cyclic Properties of Superelastic Nitinol: Design Implications. SMST-2000: The International Conference on Shape Memory and Superelastic Technologies; Pacific Grove, CA; USA; 30 Apr-4 May 2000 2001:471-476.
74. Wurzel D, Hornbogen E. THE INFLUENCE OF THERMOMECHANICAL TREATMENTS ON FATIGUE BEHAVIOR OF NiTi ALLOYS. SMST-2000: The International Conference on Shape Memory and Superelastic Technologies; Pacific Grove, CA; USA; 30 Apr-4 May 2000 2001:383-389.
75. Goo E, Sinclair R. The B2 To R Transformation in Ti50Ni47Fe3 and Ti49.5Ni50.5 alloys. Acta Metallurgica 1985 1985/9;33(9):1717-1723.
76. Newnham RE. Phase Transformations in Smart Materials. Acta Crystallographica A 1998;A54:729-737.
77. Shaw JA, Kyriakides S. Thermomechanical aspects of NiTi. Journal of the Mechanics and Physics of Solids 1995 1995/8;43(8):1243-1281.
78. Zarins CK, Arko FR, Crabtree T, Bloch DA, Ouriel K, Allen RC, et al. Explant analysis of AneuRx stent grafts: relationship between structural findings and clinical outcome. Journal of Vascular Surgery 2004 2004/7;40(1):1-11.
79. Rocha-Singh KJ, Scheer K, Rutherford J. Nitinol stent fractures in the superficial femoral artery: Incidence and clinical significance. Journal of the American College of Cardiology 2003 2003/3/19;41(6, Supplement 1):79-80.

80. Hayerizadeh BF, Zeller T, Krankenberg H, Scheinert D, Rastan A, Braunlich S, et al. Long-term outcome of superficial femoral artery stenting using self-expandable nitinol stents compared to stainless steel stents: A retrospective multicenter study. Journal of the American College of Cardiology 2003 2003/3/19;41(6, Supplement 1):80.
81. Riepe G, Heintz C, Kaiser E, Chakfe N, Morlock M, Delling M, et al. What can we Learn from Explanted Endovascular Devices? European Journal of Vascular and Endovascular Surgery 2002 2002/8;24(2):117-122.
82. Chuter TAM. Stent-graft design: the good, the bad and the ugly. Cardiovascular Surgery 2002 2002/2;10(1):7-13.
83. Barras CDJ, Myers KA. Nitinol - Its Use in Vascular Surgery and Other Applications. European Journal of Vascular and Endovascular Surgery 2000 2000/6;19(6):564-569.
84. Ginsberg GG, Faigel DO, Kochman ML, Smith D, Long WB, Habecker P. A new, self-expanding, nitinol, biliary stent: An in vivo evaluation. Gastrointestinal Endoscopy 1996 1996/4;43(4):382.
85. Jacobs TS, Won J, Gravereaux EC, Faries PL, Morrissey N, Teodorescu VJ, et al. Mechanical failure of prosthetic human implants: A 10-year experience with aortic stent graft devices. Journal of Vascular Surgery 2003;37(1):16-26.
86. Allie DE, Hebert CJ, Walker CM. Nitinol Stent Fractures in the SFA. Endovascular Today Jul/Aug 2004:1-8.
87. Serruys P, Kutryk MJB. Handbook of Coronary Stents, 2nd Ed. London: Martin Dunitz Ltd, 1998.
88. Liermann DD. STENTS: State of the Art and Future Developments. Morin Heights, Canada: Polyscience Publications, Inc., 1995.
89. Leon MB, Mintz G, S. Interventional Vascular Product Guide. Washington DC, USA: Martin Dunitz, Ltd., 1999.
90. Robertson SW, Imbeni V, Wenk H-R, Ritchie RO. Crystallographic texture for tube and plate of the superelastic/shape-memory alloy Nitinol used for endovascular stents. Journal of Biomedical Materials Research A 2005;72(2):190-199.
91. Matthies S, Vinel GW. An example demonstrating a new reproduction method of the ODF of texturized samples from reduced pole figures. Physica Status Solidi B 1982;112(2):K115-120.
92. Wenk HR, Matthies S, Donovan J, Chateigner D. BEARTEX: a Windows-based program system for quantitative texture analysis. Journal of Applied Crystallography 1998;31:262-269.
93. American Society of Testing Materials I, Subcommittee E08.06. E399: Standard test method for measurement of the plane strain fracture toughness in metallic materials. ASTM Book of Standards, 2005.
94. American Society of Testing Materials I, Subcommittee E08.06. E647: Standard test method for measurement of fatigue crack growth rates. ASTM Book of Standards, 2005.
95. Gall K, Sehitoglu H. The role of texture in tension-compression asymmetry in polycrystalline NiTi. International Journal of Plasticity 1999 1999;15(1):69-92.

96. Gao S, Yi S. Experimental study on the anisotropic behavior of textured NiTi pseudoelastic shape memory alloys. Materials Science and Engineering A 2003 2003/12/5;362(1-2):107-111.
97. Hornbogen E, Bruckner G, Gottstein G. Microstructure and texture of ausformed NiTi. Zeitschrift Fur Metallkunde 2002;93(1):3-6.
98. Inoue H, Miwa N, Inakazu N. Texture and shape memory strain in TiNi alloy sheets. Acta Materialia 1996;44(12):4825-4834.
99. Kitamura K, Miyazaki S, Iwai H, Kohl M. Effect of Heat-Treatment on the Texture in Rolled Ti-Ni Thin Plates. In: Pelton AR, Hodgson DE, Russell SM, Duerig TW, editors. Proceedings of the Second International Shape Memory and Superelastic Technologies Conference; 1997; Asilomar, CA, USA: SMST; 1997. p. 47-52.
100. Li DY, Wu XF, Ko T. The texture of Ti-51.5 at.% Ni rolling plate and its effect on the all-around shape memory effect. Acta Metallurgica et Materialia 1990;38(1):19-24.
101. Monasevich LA, Paskal YI, Prib VE, Timonin GD, Chernov DB. Effect of texture on the shape memory effect in titanium nickelide. Metal Science and Heat Treatment 1979;21:735-737.
102. Mulder IJH, Thoma PE, Beyer J. Anisotropy of thermal fatigue properties of cold-rolled TiNi sheet. Materials Characterization 1994;32(3):161-168.
103. Shu YC, Bhattacharya K. The influence of texture on the shape-memory effect in polycrystals. Acta Materialia 1998;46(15):5457-5473.
104. Sitepu H, Schmahl WW, Von Dreele RB. Use of generalized spherical harmonic model for describing crystallographic texture in polycrystalline NiTi shape-memory alloy with time-of-flight neutron powder diffraction data. Applied Physics A 2002;74:S1676-1678.
105. Vaidyanathan R, Bourke MAM, Dunand DC. Texture, Strain, and Phase-Fraction Measurements during Mechanical Cycling in Superelastic Niti. Metallurgical and Materials Transactions A (Physical Metallurgy and Materials Science) 2001;32A:777-786.
106. Yuan WQ, Yi S. Pseudo-elastic strain estimation of textured TiNi shape memory alloys. Materials Science & Engineering A 1999;A271(1-2):439-448.
107. Kocks UF, Tome CN, Wenk H-R. Texture and Anisotropy: preferred orientations in polucrystals and their effect on materials properties. Cambridge: Cambridge University Press, 1998.
108. Ono N, Sato A. Plastic Deformation Governed by the Stress Induced Martensitic Transformation in Polycrystals. Transactions of the Japan Institute of Metals 1988;29(4):267-273.
109. Ono N, Satoh A, Ohta H. A Discussion on the Mechanical Properties of Shape Memory Alloys Based on a Polycrystalline Model. Transactions of the Japan Institute of Metals 1989;30(10):756-764.
110. Vaidyanathan R, Bourke MAM, Dunand DC. Stress-induced martensitic transformations in NiTi and NiTi-TiC composites investigated by neutron diffraction. Materials Science and Engineering A 1999 1999/12/15;273-275:404-409.

111. Tada H, Paris PC, Irwin GR. The Stress Analysis of Cracks Handbook, 3rd edition. New York: ASME Press, 2000.
112. Ritchie RO, Horn RN. Further considerations on the inconsistency of toughness evaluation of AISI 4340 steel austenitized at increasing temperatures. Metallurgical and Materials Transactions A 1978;9A:331-341.
113. Imbeni V, Nalla RK, Bosi C, Kinney JH, Ritchie RO. *In vitro* fracture toughness of human dentin. Journal of Biomedical Materials Research A 2003;66A:1-9.
114. Anderson TL. Fracture Mechanics: Fundamentals and Applications. 3rd ed. Boco Raton, FL: CRC Press, 2004.
115. Knott J. Fundamentals of Fracture Mechanics. Buttersworths, UK, 1973.
116. Marrey RV, Burgermeister R, Grishaber RB, Ritchie RO. Fatigue and life prediction for cobalt-chromium stents: A fracture mechanics analysis. Biomaterials 2006;27(9):1988-2000.
117. Stankiewicz J. Master's Thesis. Berkeley: Univ. of California; Dec. 2006.
118. Ritchie RO. Mechanisms of fatigue crack propagation in metals, ceramics, and composites: Role of crack-tip shielding. Materials Science & Engineering A 1988;103:15-28.
119. Ritchie RO. Mechanisms of fatigue-crack propagation in ductile and brittle solids. International Journal of Fracture 1999;100:55-83.
120. Ritchie RO, Knott JF. Mechanisms of fatigue crack growth in low alloy steel. Acta Metallurgica 1973;21:639-648.
121. Paris PC, Erdogan F. A critical analysis of crack propagation laws. Journal of Basic Engineering, Trans ASME, Ser D 1963;85:528-534.
122. Bartlett ML, Hudak SJ. The influence of frequency-dependent crack closure on corrosion fatigue-crack growth. In: Kitagawa H, Tanaka K, editors. Fatigue 90. Birmingham, UK: Materials & Components Engineering Publications, 1990. p. 1783-1788.
123. Suresh S, Zamiski GF, Ritchie RO. Oxide-induced crack closure: An explanation for near-threshold corrosion fatigue crack growth behavior. Metallurgical and Materials Transactions A 1981;12A:1435-1443.
124. Armitage P, Berry G. Statistical Methods in Medical Research 3rd Ed.: Blackwell Publishing, 1994.
125. Valek BC. X-Ray Microdiffraction Studies of Mechanical Behavior and Electromigration in Thin Film Structures [Ph.D.]. Palo Alto: Stanford University; 2003.
126. Imbeni V, Mehta A, Robertson SW, Duerig TW, Pelton AR, Ritchie RO. On the Mechanical Behavior of Nitinol under Multiaxial Loading Conditions and *In Situ* Synchrotron X-Ray. In: Pelton AR, Duerig T, editors. Proceedings of the International Conference on Shape Memory and Superelastic Technologies; 2003; 2003. p. 267-276.
127. Kulkov SN, Mironov YP. Martensitic transformation in NiTi investigated by synchrotron X-ray diffraction. Nuclear Instruments and Methods in Physics Research Section A: Accelerators, Spectrometers, Detectors and Associated Equipment Proceedings of the 10th National Synchrotron Radiation Conference 1995 1995/5/1;359(1-2):165-169.

128. Paula AS, Canejo JHPG, Mahesh KK, Silva RJC, Fernandes FMB, Martins RMS, et al. Study of the textural evolution in Ti-rich NiTi using synchrotron radiation. Nuclear Instruments and Methods in Physics Research Section B: Beam Interactions with Materials and Atoms Synchrotron Radiation and Materials Science - Proceedings of the E-MRS 2005 Symposium O on Synchrotron Radiation and Materials Science 2006 2006/5;246(1):206-210.
129. Schmahl WW, Khalil-Allafi J, Hasse B, Wagner M, Heckmann A, Somsen C. Investigation of the phase evolution in a super-elastic NiTi shape memory alloy (50.7 at.%Ni) under extensional load with synchrotron radiation. Materials Science and Engineering A European Symposium on Martensitic Transformation and Shape-Memory 2004 2004/7/25;378(1-2):81-85.
130. Labossiere PE, Perry KE. The Effects of Notches and Grain Size on Transformations in Nitinol. In: Pelton AR, Duerig T, editors. Proceedings of the International Conference on Shape Memory and Superelastic Technologies (SMST); 2003; Pacific Grove, CA, USA: SMST; 2003. p. 259-266.
131. Loughran GM, Shield TW, Leo PH. Fracture of shape memory CuAlNi single crystals. International Journal of Solids and Structures 2003;40(2):271-294.
132. Lexcellent C, Blanc P. Phase transformation yield surface determination for some shape memory alloys. Acta Materialia 2004;52(8):2317-2324.
133. Barney M, Pelton AR. Unpublished work: angular dependence of stress/strain response in Nitinol flattened tube. Nitinol Devices and Components (NDC), a Johnson & Johnson Company, 2006.
134. Saburi T, Wayman CM. Crystallographic Similarities in Shape Memory Martensites. Acta Metallurgica 1979;27:979-995.
135. Ritchie RO, Lankford J. Small fatigue cracks: A statement of the problem and potential solutions. Materials Science & Engineering 1986;84:11-16.
136. Suresh S, Ritchie RO. A geometric model for fatigue crack closure induced by fracture surface roughness. Metallurgical and Materials Transactions A 1982;13A:1627-1631.
137. Kitagawa H, Takahashi S. Applicability of fracture mechanics to very small cracks or the cracks in the early stages. Proceesings of the Second International Conference on Mechanical Behavior of Materials; 1976; Metals Park, OH: American Society for Metals (ASM); 1976. p. 627-631.
138. Gong XY, Pelton AR, Duerig TW, Rebelo N, Perry K. Finite element analysis and experimental evaluation of superelastic Nitinol stent. In: Pelton AR, Duerig T, editors. Proceedings of the International Conference on Shape Memory and Superelastic Technologies; 2003; Pacific Grove, CA: SMST; 2003. p. 311-320.
139. Rebelo N, Gong XY, Connally M. Finite element analysis of plastic behavior in Nitinol. In: Pelton AR, Duerig T, editors. Proceedings of the International Conference on Shape Memory and Superelastic Technologies; 2003; Pacific Grove, CA: SMST; 2003. p. 501-507.

APPENDIX A: COMPUTER SIMULATION OF NITINOL TRANSFORMATION ZONE

The following Matlab code was written to: a) simulated the anisotropic yield surface of Nitinol derived by Lexcellent and Blanc Surface [132], and b) use fracture mechanics solutions of stress intensity around a crack tip to predict a transformation zone size.

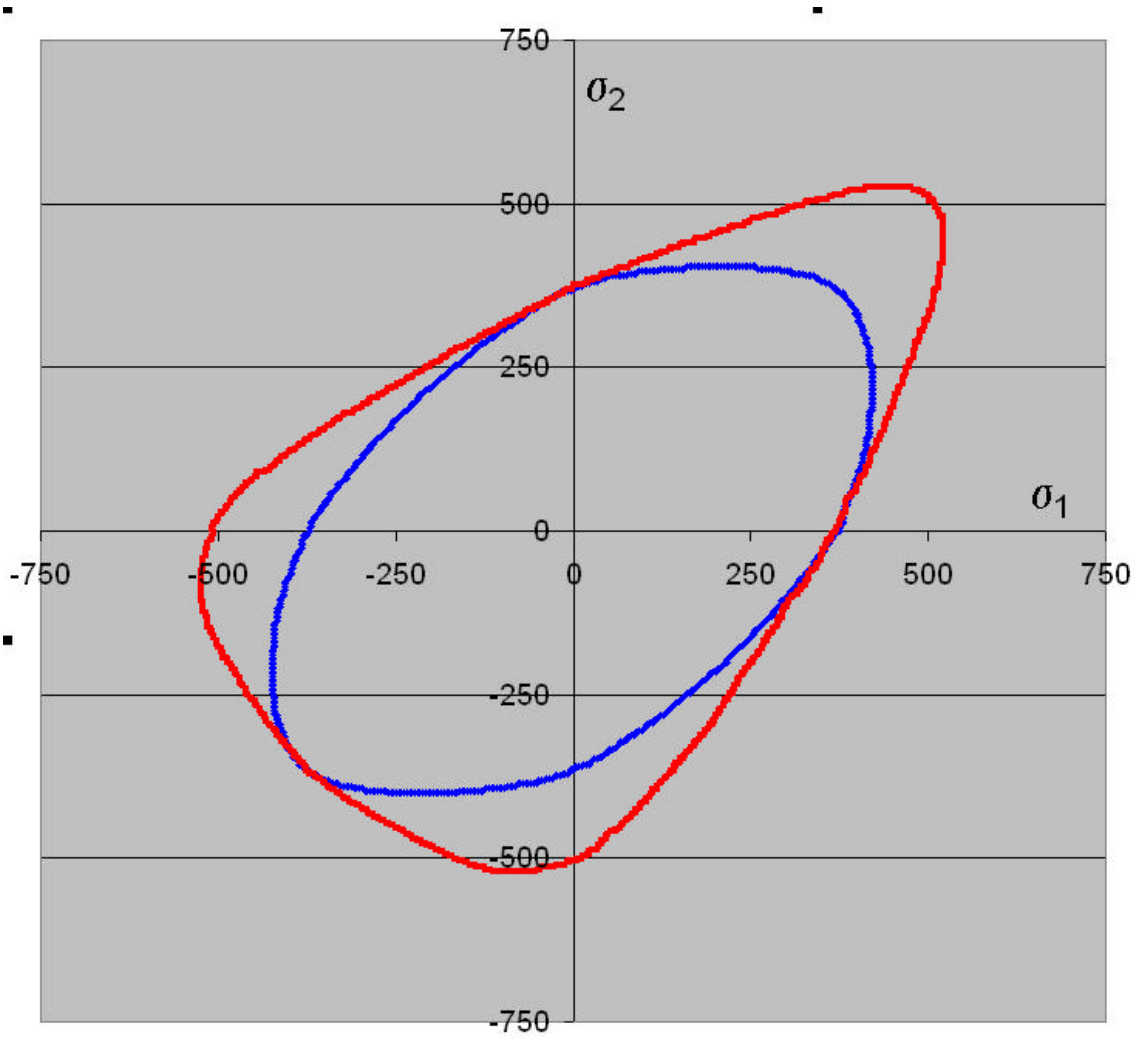

Figure A.1: Yield surface, plotted in terms of principal stresses in MPa, derived from anisotropic yield conditions for Nitinol from Lexcellent and Blanc (red plot), vs. isotropic yield condition (von Mises) shown in blue.

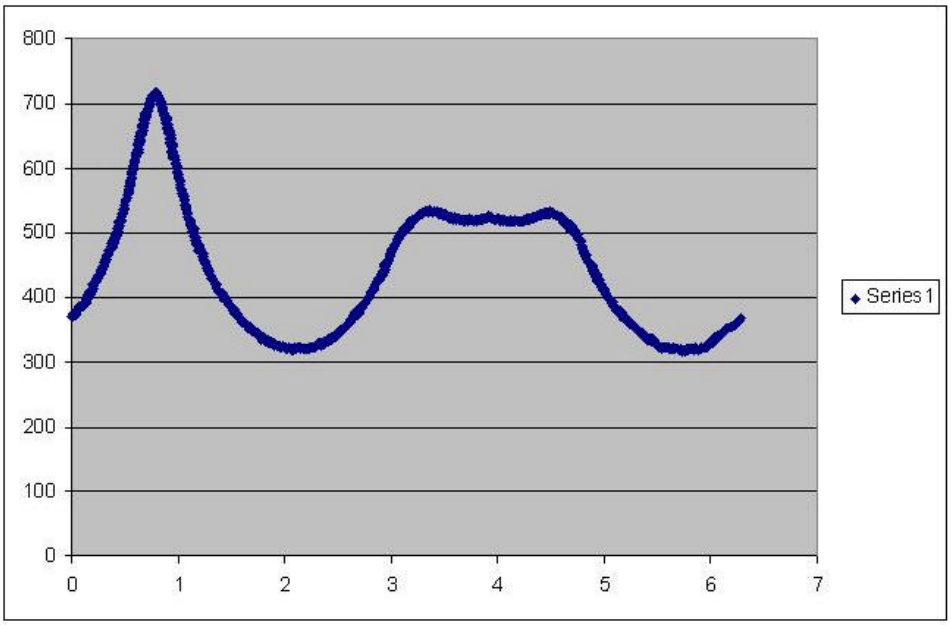

Figure A.2: Lexcellent and Blanc's yield surface plotted as radial coordinates (radians vs. yield stress) rather than principal stresses in Fig. A.1. This is the output from the computer simulation of the yield surface.

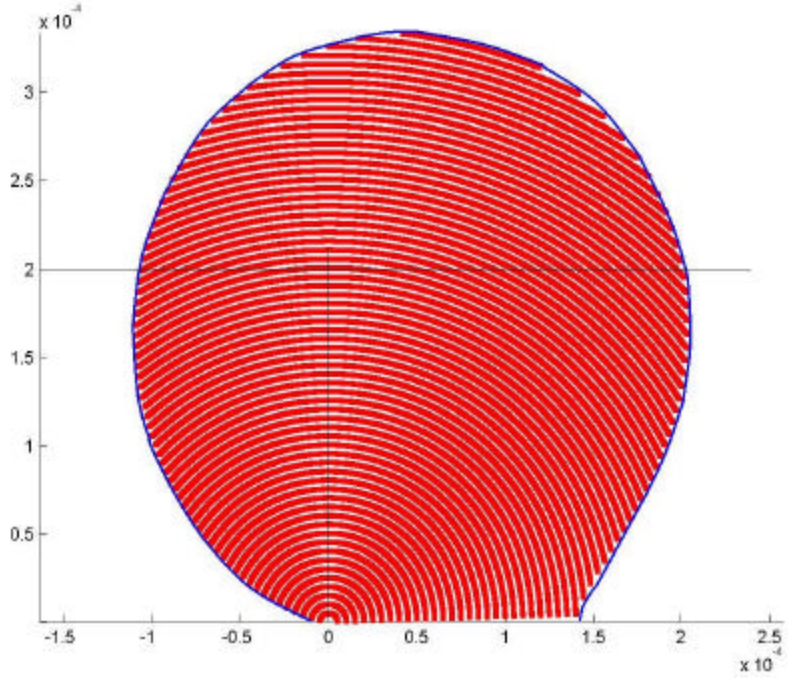

Figure A.3: Half transformation zone size as calculated from the computer simulation by the combination of the Lexcellent and Blanc yield criterion with standard fracture mechanics solutions. Plot was predicted for a stress intensity of 15 MPa√m, with the scale in meters.

```
%%%%% The following approximates the empirical yield surface from Lexcellent, Acta
Met 2004 %%%%%%

clear all;

index = 1;
theta = 0;

% From 0 - 45 degrees
for theta = 0:pi/250:pi/4;
   C6 = -2891.4;
   C5 = -1687.8;
   C4 = 8413.5;
   C3 = -5886;
   C2 = 1895.2;
   C1 = 6.4885;
   C0 = 372.69;

   r = C6*theta^6 + C5*theta^5 + C4*theta^4 + C3*theta^3 + C2*theta^2 + C1*theta +
C0;

   y(index,1) = theta;
   y(index,2) = r;
   index = index + 1;
end;

% From 45 - 90 degrees
for theta = pi/4:pi/250:pi/2;
   C6 = -10963;
   C5 = 85070;
   C4 = -272917;
   C3 = 462867;
   C2 = -436765;
   C1 = 216291;
   C0 = -42991;

   r = C6*theta^6 + C5*theta^5 + C4*theta^4 + C3*theta^3 + C2*theta^2 + C1*theta +
C0;

   y(index,1) = theta;
   y(index,2) = r;
   index = index + 1;
end;

% From 90 - 180 degrees
```

```
for theta = pi/2:pi/500:pi;
    C2 = 187.72;
    C1 = -794.66;
    C0 = 1158.8;

    r = C2*theta^2 + C1*theta + C0;

    y(index,1) = theta;
    y(index,2) = r;
    index = index + 1;
end;

% From 180 - 190 degrees
for theta = pi:pi/1125:pi*(190/180);
    C2 = -526.15;
    C1 = 3559.3;
    C0 = -5484.5;

    r = C2*theta^2 + C1*theta + C0;

    y(index,1) = theta;
    y(index,2) = r;
    index = index + 1;
end;

% From 190 - 225 degrees
for theta = (190/180)*pi:pi/320:(225/180)*pi;
    C3 = 201.82;
    C2 = -2098.9;
    C1 = 7222;
    C0 = -7690.7;

    r = C3*theta^3 + C2*theta^2 + C1*theta + C0;

    y(index,1) = theta;
    y(index,2) = r;
    index = index + 1;
end;

% From 225 - 260 degrees
for theta = (225/180)*pi:pi/320:(260/180)*pi;
    C3 = -118.16;
    C2 = 1617.5;
    C1 = -7312;
    C0 = 11450;
```

```
    r = C3*theta^3 + C2*theta^2 + C1*theta + C0;

    y(index,1) = theta;
    y(index,2) = r;
    index = index + 1;
end;

% From 260 - 270 degrees
for theta = (260/180)*pi:pi/1125:1.5*pi;
    C2 = -320.93;
    C1 = 2824.2;
    C0 = -5678;

    r = C2*theta^2 + C1*theta + C0;

    y(index,1) = theta;
    y(index,2) = r;
    index = index + 1;
end;


% From 270 - 360 degrees
for theta = 1.5*pi:pi/200:2*pi;
    C2 = 179.74;
    C1 = -2061.5;
    C0 = 6228.7;

    r = C2*theta^2 + C1*theta + C0;

    y(index,1) = theta;
    y(index,2) = r;
    index = index + 1;
end;


scatter(y(:,1),y(:,2));


%%%%%This ends the yield surface approximation %%%%

clear all;


%%%%%% The following plots the PLANE STRESS transformation surface for Nitinol
(370MPa A-M) %%%%%%
```

```
K = input('Input applied Mode I stress intensity (MPa*m^0.5):  ');

step = 1;
% R and t are radial coordinates about a crack tip in a C(T) specimen;

R = 0; % R is in meters
t = 0; % t is in radians

% Eval(1,1) = 'R';
% Eval(1,2) = 't';
% Eval(1,3) = 'sigma1';
% Eval(1,4) = 'sigma2';
% Eval(1,5) = 'evalR';
% Eval(1,6) = 'evaltheta';
% Eval(1,7) = 'r';
% Eval(1,8) = 'C6';
% Eval(1,9) = 'C5';
% Eval(1,10) = 'C4';
% Eval(1,11) = 'C3';
% Eval(1,12) = 'C2';
% Eval(1,13) = 'C1';
% Eval(1,14) = 'C0';
% Eval(1,15) = 'marker';

% Constraints for R may need to be increased/decreased for K level
for R = 0.00008:0.000002:0.00025;
   for t = pi/200:pi/200:pi;
      sigma1 = K*cos(t/2)*(1+sin(t/2))/(sqrt(2*R*pi));
      sigma2 = K*cos(t/2)*(1-sin(t/2))/(sqrt(2*R*pi));
      evalR = sqrt(sigma1^2+sigma2^2);
      evaltheta = atan(sigma2/sigma1); %quadrant 1
      if sigma1 > 0;
         if sigma2 < 0; %quadrant 4
            evaltheta = 2*pi + evaltheta;
         end;
      end;

      if sigma1 < 0; %quadrant 2 and 3
         evaltheta = pi + evaltheta;
      end;

      theta = evaltheta;
      C6 = 0;
      C5 = 0;
      C4 = 0;
      C3 = 0;
```

```
        C2 = 0;
        C1 = 0;
        C0 = 0;

% Criteria 1 (0-45 degrees)
if theta > 0;
    if theta < pi/4;

    C6 = -2891.4;
    C5 = -1687.8;
    C4 = 8413.5;
    C3 = -5886;
    C2 = 1895.2;
    C1 = 6.4885;
    C0 = 372.69;
end;
end;

% Criteria 2 (45-90 degrees)
if theta > pi/4;
    if theta < pi/2;

    C6 = -10963;
    C5 = 85070;
    C4 = -272917;
    C3 = 462867;
    C2 = -436765;
    C1 = 216291;
    C0 = -42991;
end;
end;

% Criteria 3 (90-180 degrees)
if theta > pi/2;
    if theta < pi;

    C2 = 187.72;
    C1 = -794.66;
    C0 = 1158.8;
end;
end;

% Criteria 4 (180-190 degrees)
if theta > pi;
    if theta < (190/180)*pi;
```

```
    C2 = -526.15;
    C1 = 3559.3;
    C0 = -5484.5;
end;
end;

% Criteria 5 (190-225 degrees)
if theta > (190/180)*pi;
    if theta < (225/180)*pi;

    C3 = 201.82;
    C2 = -2098.9;
    C1 = 7222;
    C0 = -7690.7;
end;
end;

% Criteria 6 (225-260 degrees)
if theta > (225/180)*pi;
    if theta < (260/180)*pi;

    C3 = -118.16;
    C2 = 1617.5;
    C1 = -7312;
    C0 = 11450;
end;
end;

% Criteria 7 (260-270 degrees)
if theta > (260/180)*pi;
    if theta < 1.5*pi;

    C2 = -320.93;
    C1 = 2824.2;
    C0 = -5678;
end;
end;

% Criteria 8 (270-360 degrees)
if theta > 1.5*pi;
    if theta < 2*pi;

    C2 = 179.74;
    C1 = -2061.5;
    C0 = 6228.7;
end;
```

```
end;

r = C6*theta^6 + C5*theta^5 + C4*theta^4 + C3*theta^3 + C2*theta^2 + C1*theta + C0;

   if r > evalR;
      marker = 0;
   else;
      marker = 1;
   end;

xpos(step,1) = R*cos(t);
ypos(step,1) = R*sin(t);
Eval(step+1,1) = R;
Eval(step+1,2) = t;
Eval(step+1,3) = sigma1;
Eval(step+1,4) = sigma2;
Eval(step+1,5) = evalR;
Eval(step+1,6) = evaltheta;
Eval(step+1,7) = r;
Eval(step+1,8) = C6;
Eval(step+1,9) = C5;
Eval(step+1,10) = C4;
Eval(step+1,11) = C3;
Eval(step+1,12) = C2;
Eval(step+1,13) = C1;
Eval(step+1,14) = C0;
Eval(step+1,15) = marker;
C(step,1) = marker;

step = step+1;


end; %ends t for loop
end; %ends R for loop

C(:,2)=0;
C(:,3)=0;

dlmwrite('mydata.out',Eval,',');
scatter(xpos,ypos,2,C,'s','filled');
```

Appendix B: Derivation of Stresses from Deviatoric Strains Measured by Diffraction

Goal:
Determine the equivalent stress and strain state around a crack tip in Nitinol

Experimental Data:

Deviatoric strains, e'_{ij}, calculated from white-beam Laue diffraction patterns. Dilational strain cannot be measured without monochromatic diffraction data. The dilational strains, and the total stresses, must therefore be inferred from the deviatoric strains alone.

Assumptions:

1) Isotropic material: valid only for the linear elastic portion of Austenite (note: transformation stress/strain values are anisotropic, but elastic stiffness is isotropic). Since the Laue patterns disappear upon transformation, the only deviatoric strains that were measured must be for Austenite, not Martensite.
2) Austenite remains perfectly linear-elastic (i.e. no plastic deformation of Austenite). That is, the material is either elastically deformed Austenite, or the material has transformed to Martensite. Therefore, Hookean behavior prevails
3) Plane stress (σ_{33} = 0). Since the depth of penetration of x-rays is only 5-10 microns below the surface, we can assume that the sampled region is essentially a free surface under plane stress conditions.

Calculations:

Basic formulation of strain: Total = Deviatoric + Dilational

$$e_{ij} = e'_{ij} + d_{ij}\frac{e}{3} \tag{1}$$

$$\text{where, } d_{ij} = \begin{matrix} 1; i = j \\ 0; i \neq j \end{matrix}$$

Therefore:

$$e_{11} = e'_{11} + \frac{e}{3} \tag{2a}$$

$$e_{22} = e'_{22} + \frac{e}{3} \tag{2b}$$

$$e_{33} = e'_{33} + \frac{e}{3} \tag{2c}$$

$$e_{12} = e'_{12} \tag{2d}$$

$$e_{13} = e'_{13} \tag{2e}$$

$$e_{23} = e'_{23} \tag{2f}$$

Hooke's Law:

$$s_{ij} = C_{ijkl} e_{ij} \tag{3}$$

For isotropic material:

$$C_{11} = C_{22} = C_{33}; C_{44} = C_{55} = C_{66}; C_{12} = C_{21} = C_{13} = C_{31} = C_{23} = C_{32}$$

$$2G = \frac{E}{1+u} \tag{4}$$

$$l = \frac{2Gu}{1-2u} \tag{5}$$

$$C_{11} = l + 2G = \frac{(1-u)E}{(1+u)(1-2u)} \tag{6}$$

$$C_{12} = l = \frac{uE}{(1+u)(1-2u)} \tag{7}$$

$$C_{44} = G = \frac{E}{2(1+u)} \tag{8}$$

Therefore, *Eqn. 3* becomes:

$$\begin{bmatrix} s_{11} \\ s_{22} \\ s_{33} \\ s_{12} \\ s_{13} \\ s_{23} \end{bmatrix} = \begin{bmatrix} C_{11} & C_{12} & C_{12} & 0 & 0 & 0 \\ C_{12} & C_{11} & C_{12} & 0 & 0 & 0 \\ C_{12} & C_{12} & C_{11} & 0 & 0 & 0 \\ 0 & 0 & 0 & C_{44} & 0 & 0 \\ 0 & 0 & 0 & 0 & C_{44} & 0 \\ 0 & 0 & 0 & 0 & 0 & C_{44} \end{bmatrix} \begin{bmatrix} e_{11} \\ e_{22} \\ e_{33} \\ e_{12} \\ e_{13} \\ e_{23} \end{bmatrix} \tag{9}$$

From matrix multiplication of *Eqn 9* to obtain stress relationship to strain (with plane stress zero values shown):

$$s_{11} = C_{11} e_{11} + C_{12}(e_{22} + e_{33}) \tag{10a}$$

$$s_{22} = C_{11} e_{22} + C_{12}(e_{11} + e_{33}) \tag{10b}$$

$$s_{33} = C_{11} e_{33} + C_{12}(e_{11} + e_{22}) = 0 \tag{10c}$$

$$s_{12} = C_{12} e_{12} \tag{10d}$$

$$s_{13} = C_{12} e_{13} = 0 \tag{10e}$$

$$s_{23} = C_{12} e_{23} = 0 \tag{10f}$$

For plane stress conditions, σ_{33}=0: Substituting *Eqn 1* into *Eqn 10c*:

$$s_{33} = 0 = C_{11}\left(e'_{33} + \frac{e}{3}\right) + C_{12}\left(e'_{11} + e'_{22} + \frac{2e}{3}\right) \tag{11a}$$

$$s_{33} = 0 = \left[C_{11} e'_{33} + C_{11} \frac{e}{3} \right] + \left[C_{12} \left(e'_{11} + e'_{22} \right) + C_{12} \frac{2e}{3} \right] \tag{11b}$$

$$s_{33} = 0 = C_{11} e'_{33} + C_{12} \left(e'_{11} + e'_{22} \right) + e \left(\frac{2C_{12}}{3} + \frac{C_{11}}{3} \right) \tag{11c}$$

Solving for the dilational strain component from *Eqn 11c*, and using stiffness relation *Eqn 6* & *7*:

$$\boxed{e = -\frac{C_{12} \left(e'_{11} + e'_{22} \right) + C_{11} e'_{33}}{\left(\frac{2C_{12}}{3} + \frac{C_{11}}{3} \right)} = -\frac{3}{(1+u)} \left[u \left(e'_{11} + e'_{22} \right) + (1-u) e'_{33} \right]} \tag{12}$$

Plugging the dilational strain from *Eqn 12* into *Eqn 2* will produce the ***total strain tensor***. Multiplying that total strain tensor by the stiffness matrix (i.e. operating *Eqn 9*) produces the ***total stress tensor***.

Using the total stress and strain tensors, we can now calculate equivalent stresses and strains:

$$\bar{s} = \sqrt{J_1^2 - 3J_2} \tag{13}$$

$$J_1 = s_{11} + s_{22} + s_{33} = 3s \tag{14}$$

$$J_2 = s_{11} s_{22} + s_{22} s_{33} + s_{11} s_{33} - \left(s_{12}^2 + s_{13}^2 + s_{23}^2 \right) \tag{15}$$

$$\boxed{\bar{s} = \sqrt{\tfrac{1}{2}[(s_{11} - s_{22})^2 + (s_{11} - s_{33})^2 + (s_{22} - s_{33})^2] + 3(s_{12}^2 + s_{13}^2 + s_{23}^2)}} \tag{16}$$

$$\bar{e} = \frac{2}{3} \sqrt{I_1^2 - 3I_2} \tag{17}$$

$$I_1 = e_{11} + e_{22} + e_{33} = e \tag{18}$$

$$I_2 = e_{11} e_{22} + e_{22} e_{33} + e_{11} e_{33} - \left(e_{12}^2 + e_{13}^2 + e_{23}^2 \right) \tag{19}$$

$$\boxed{\bar{e} = \frac{2}{3} \sqrt{\tfrac{1}{2}[(e_{11} - e_{22})^2 + (e_{11} - e_{33})^2] + (e_{22} - e_{33})^2 + 3(e_{12}^2 + e_{13}^2 + e_{23}^2)}} \tag{20}$$